ABSTRACT

O'BRIEN, SEAN EDWARD. *A Posteriori* Error Estimators for the Discrete Ordinates Approximation of the One-Speed Neutron Transport Equation. (Under the direction of Yousry Azmy.)

When calculating numerical approximations of the neutron transport equation it is important to have a measure of the accuracy of the solution. As the true solution is not known in most applications, a suitable estimation of the error, that does not require knowledge of the true solution, must be used. The steady state transport equation can possess errors due to the discretization of all its variables, angle, energy and space. In this work only spatial discretization errors are considered in the one-speed discrete ordinates formulation of the steady state transport equation. To assess the accuracy of the error estimator a corresponding exact transport solution is manufactured in order to determine the numerical solution's true discretization error. The method of generating the true solution has the unique property of specifying the degree of regularity of the flux across the singular characteristic. This solution is then projected onto a Legendre polynomial space in order to form an exact solution on the same basis as the numerical solution to enable computation of the true error. In addition, the manufacturing method provides a distributed source and boundary conditions that are used in the numerical solution algorithm to yield the corresponding numerical solution. In our work, the numerical solution is obtained by the Discontinuous Galerkin Finite Element Method, utilizing a Legendre Polynomial basis space. Over a series of test problems in which the spatial mesh and geometry, regularity across the singular characteristic and cross sections are varied, the true error is comparred to the error estimated by: a two-mesh cell centered estimator, Ragusa and Wang's two-mesh estimator, Residual Source, Madsen's and cell discontinuity estimators, angular flux and scalar flux forms. The validity and accuracy of the considered estimators are assessed by considering the effectivity index, global $L2$ norm of the error and other metrics. In general we observe that the two-mesh estimators, cell centered and Ragusa and Wang, excell at approximating the true error distribution but usually under-estimate its magnitude; the residual estimators,

Madsen's and Residual Source, emulate the true error distribution but frequently over-estimate the magnitude of the true error; the discontinuity estimators, both angular and scalar flux forms, sufficently captures the true error distribution and generally under-estimate the error about the singular characteristics but over-estimate the error elsewhere. Further distinctions of an estimator's relms of effectiveness are made among various problem specifications that include: degree of regularity across singular characteristics, optical thickness, scattering ratios, domain geometry and basis order.

A Posteriori Error Estimators for the Discrete Ordinates Approximation of the One-Speed Neutron Transport Equation

by
Sean Edward O'Brien

A thesis submitted to the Graduate Faculty of
North Carolina State University
in partial fulfillment of the
requirements for the degree of
Master of Science

Nuclear Engineering

Raleigh, North Carolina

2012

APPROVED BY:

Dmitriy Anistratov	John Harlim
Randy Baker	Yousry Azmy Chair of Advisory Committee

DEDICATION

To my parents.

BIOGRAPHY

The author was born in Richmond, Virginia on March 31, 1987 to Wayne and Martha O'Brien, the oldest of three children. Raised in Farmville, where he worked construction and on a dairy and hog farm to support his college aspirations. He graduated Cum Laude from James Madison University in 2009 with his bachelors of science in Physics. While at JMU he worked under Dr. Steve Whisnant as member of the photo-nuclear group. There he researched the development of polarized, scintillating plastic targets for a program of high energy polarized gamma ray on polarized nucleon scattering at Duke University's $HI\gamma s$ facility at TUNL. In conjunction with this project he performed optimization and characterization measurements of large NaI spectrometers. In his final year at JMU he began work with Dr. Kevin Giovanetti as a member of the pre-shower calorimeter group, a collaboration with Jefferson Lab. There he designed a photomultiplier tube characterization database and worked in the experimental Hall B counting house. In addition to research, the author was a teaching assistant for five courses and was a physics department sanctioned private tutor. While in the program he was inducted into ΠΣΠ, the physics honors society, and received the Dr. Raymond A. and Elizabeth Serway Physics Scholarship and the Madison Department Achievement Scholarship in Physics.

Upon graduating from JMU he entered North Carolina State University's Nuclear Engineering graduate program under the direction of Dr. Yousry Azmy, where he began studying the error estimation of the neutron transport equation. In the summer of 2010, he worked as a graduate research assistant at Los Alamos National Laboratory, under the guidance of Dr. Randy Baker, where he worked on the development of an *a posteriori* error estimator for adaptive mesh refinement in the PARTISN code.

ACKNOWLEDGEMENTS

I would like to thank my advisor, Yousry Y. Azmy, for his guidance and patience. I am indebted to my fellow students, in particular Sebastian for his help in utilizing the MMS and DGFEM codes, for their support and friendship. Finaly I'd like to credit the Global Village coffee shop for brewing a strong cup of coffee, this work could not have been written without it.

TABLE OF CONTENTS

LIST OF TABLES

LIST OF FIGURES

CHAPTER 1

Introduction

1.1 Motivation and Goals

When performing numerical calculations it is important that the error in the solution be known. The error can be used for many purposes which include determining the confidence in the solution and driving adaptive mesh refinement (AMR) algorithms . In practice it is impossible to know the exact error in the solution because this would mean one possesess the exact solution making any numerical calculations unnecessary. In practice the best that one can achieve is an approximate estimation of the solution's discretization error. Before one uses an estimator there must be information validating its accuracy and its applicability. Performing this verification for a selection of estimators is the objective of this work.

There are many types of error estimators but they fall into two general categories: *a priori* and *a posteriori*. The concept of the *a posteriori* error estimator is described succinctly by Oden and Ainsworth: "*a posteriori* error estimation, whereby the computed solution itself is used to assess the accuracy" [2]. *A priori* estimates are founded on information available before the numerical solution is determined.

This work is concerned with *a posteriori* spatial error estimators. The estimators considered only measure the solution's spatial discretization error and is why the One-Speed Discrete Ordinates approximation of the Neutron Transport Equation is considered. It is one-speed (one-energy group) such that no errors arise from scatterings between energy groups. The Discrete Ordinates approximation of the angle variable is taken to effectively represent reality allowing one to essentially ignore any angle related error.

It was stated that the true solution is typically not known and without it one does not have a means to compare the estimated error to the true error. In this work the Method of Manufactured Solutions (MMS) is used. As the name suggest the true solution is known, in this case analytically, and can be used to produce a known true error.

To generate the numerical solution to base the estimators on the Discontinuous Galerking Finite Element Method (DGFEM) is considered. This numerical method takes as input the nuclear properties (basically cross sections data), distributed source and boundary data of the MMS solution to arrive at its own approximate solution. The error estimators can only rely on the inputs and outputs of the DGFEM problem but not on the MMS generated solution. The true and estimated errors are then formed from these solutions.

With both errors in hand one can begin verifying the effectiveness of the error estimator. This is primarily done by considering the effectivity index and global norms of the error. These tools form the principal standard such that each estimator can be independently verified and provides measures of comparison between estimators. In addition a simple cost benefit analysis is performed which accounts for the cost of computing the error estimator measured in computational time as compared to what is reaped in terms of the estimator's ability to accurately represent the error magnitude and spatial distribution.

In this work there are six estimators that are considered and they fall into three main categories. First, there are estimators that rely on the computation of an additional solution on a mesh that has been refined by a factor of two. These are the Cell Centered and Ragusa and Wang estimators. Second, there are estimators that are constructed using the residual of the solution. These are the Madsen and Residual Source error estimators. Finally, there are estimators that relate the error to the degree of discontinuity of the solution along element boundaries. These Jump Discontinuity estimators are considered in angular and scalar fluxes.

1.2 Summary of Results and Conclusions

Though distinctions between estimators are made. There are many potential uses for any estimator and many excel when considering a specific application, such as AMR. On the whole each estimator is effective enough for particular applications. Though each has its own drawbacks as well.

The two-mesh based estimators generally underestimate the true error in the solution but typically model the true error distribution accurately. The requirement for a second transport solution is usually a drawback but is natural for AMR applications. On the whole the Ragusa and Wang estimator is superior to the Cell Centered estimator because as the mesh is refined its average effectivity index remains close to one.

The residual based error estimators typically over-estimate the error, especially when considering the global error. The Madsen estimator acts as an upper bound of the true error and always excessively over estimates it but does a decent job of approximating the true error distribution. The Residual Source estimator requires an additional transport solve on the same mesh but does a superior job in approximating the true error in magnitude and distribution. If the additional computational cost is worth it the Residual Source estimator is generally superior to Madsen, but the latter is the only considered estimator that uniformily bounds the error everywhere.

The Jump Discontinuity estimators in both angular and scalar flux forms behaved principally the same. In particular, they excelled for the case of constant basis functions of the DGFEM formulation and approximated the error distribution and magnitude well. However, for all basis cases, icluding and beyond the constant basis case, the global error was slightly underestimated but trended with the true global error curve. Overall, as these two manifestations perform so similarly the scalar flux version is preferable in that it requires a greatly reduced computational effort.

On the whole each estimator is reasonably adept in certain situations and there are clearly superior estimators in each category. However, with all metrics considered equal the Ragusa and Wang estimator is the most well behaved. In particular it escapes the trend of increasing average effectivity indexes far above unity with mesh refinement.

CHAPTER 2

Review of the Literature

2.1 Error Estimators

This review of the literature is composed with the purpose of providing a basic background of, and cataloging of several advancements in the development of *a posteriori* error estimators in general and then with specific application to radiation transport methods. In this work, a selection of these error estimators is applied to the steady-state, one-speed, discrete ordinates, Discontinuous Galerkin Finite Element Method (DGFEM) discretization of the neutron transport equation. In the present work only spatial discretization errors are considered. Error estimators provide an approximation of the true error that can be utilized to drive adaptive mesh refinement (AMR) algorithms, provide confidence in results and quantify uncertainty.

Discussion of the various types of *a posteriori* error estimators is often dependent on the target numerical solution method. Due to the large number of distinct numerical solution methods, the classes of error estimates will be relegated to the finite element method, in particular Discontinuous Galerkin Finite Element Method solutions. In addition, local error estimators will be considered. This is the error that is present in a given cell and is often a single value or a distribution. A global estimator is a quantity that provides one with knowledge of the error incurred in every computational cell of the solution domain. However, one can often construct the global error as some norm of local ones.

No attempt at a chronological structure of the ensuing review will be made and the principal papers for each estimator will be presented as representative of the estimator at hand. Additionally, the distinction between error estimators and error indicators will not be explicitly made as such a distinction is often subtle and the usage of these two terms is not uniform throughout the field of study [14]. The two terms take on two primary meanings. First, the indicator is often the error associated with a particular element and the estimator is a global error that is usually a totality, in some norm, of the indicators. The second usage is that the estimator is a more rigorous estimate of the error where as the indicator merely gives signs indicative of the size of the error but does not actually approximate the value of the error. So, throughout this work the term error estimator is generally used to mean an element error and an approximation of the true error.

2.2 *A Posteriori* Error Estimators

In 1978, Babuska and Rheinboldt developed error estimators for finite element solutions by considering one-dimensional boundary value problems, in particular "source, eigenvalue, and parabolic problems are considered involving a linear, self-adjoint operator of the second order" [4]. The resulting error estimators were shown to have good agreement with the true error, based on several theorems in finite element analysis. This was accomplished by simultaneously generating upper and lower bounds for the error. These bounds were constructed in the energy norm over every finite element and were also extended to p-norms, leading to an estimation of both the local and global errors. The resulting error estimates were shown to be computationally cheap enough to provide a foundation for AMR routines. These authors' work concerning AMR implementation can be seen in [3] and earlier analysis of the the presented error estimators was reported in [5].

While some *a posteriori* error estimators rely only upon manipulations involving the computed solution, the work of Ladeveze and Leguillon [17] utilizes that solution in conjunction with the solution of a complementary problem. This complementary problem is derived by considering a constitutive law, basically a mathematical relationship (often simple) between two quantities, such as Hooke's law which establishes the relationship between stress-strain or Fick's law which defines the diffusion coefficient based on materials' properties, of the primary solution. One can consider the solution of this constitutive law within each element as an approximate solution that provides a permissible boundary condition for valid solutions. When the solutions are compared it yields the desired error estimate on an element by element basis. As in many other works in this area the estimator is shown to be successfully applied to an AMR methodology by using the error estimate to flag elements eligible for refinement.

Advancing the idea of solving a complimentary problem then comparing its solution to the given numerical solution to estimate the local error, Bank and Weiser proposed three estimators that rely on "solving local Neumann problems in each element" [6]. Their work is focused on elliptic partial differential equations utilizing a finite element solution. The three estimators vary in how they demand consistency between the local and global problems, chiefly in algorithm construction. The element by element approach immediately leads to error estimates that are explicitly relevant to a particular element and is computationally favorable because element calculations rely on information of the element and nearest neighbors instead of necessitating a global matrix solution. This local computational approach is efficient as one considers "computations which involve only one or a few neighboring elements at a time" [6]. The effectiveness of these *a posteriori* error estimators is naturally dependent on how well-posed the local problem is. All three estimators, are shown to satisfy the same inequality that provides upper and lower bounds, for the estimates, in terms of the true error. This technique can also be extended to local Dirichlet boundary condition problems.

The work of Demkowicz et al., investigates the use of interpolation finite element error estimates [8]. The method relies on the use of ”extraction formulas” that provide an estimation of the exact solution’s second-order derivatives by using the numerical solution whose error is to be estimated over the individual finite elements. The error estimator is derived by considering the difference between the approximated second-order derivatives of the interpolated derivative of the solution and those calculated from the pure numerical solution. This restriction is beneficial in detecting regions in the domain which contain discontinuities/singularities and in this regard, behaves as a sufficiently reliable indicator of the error to drive an AMR routine.

Similar to the work of Demkowicz,[8] is that of Dias, Kikuchi and Taylor [9]. In their work an interpolation method is utilized to arrive at an estimate of the error but without requiring the solution of auxiliary problems (extraction formulas) as in Demkowicz’s work. This method is powerful in that it correlates the error to the size of an element [9]. The validity of these relationships can be shown by proofs of bounds on the error from interpolation theory, and they naturally leads to implementation as a successful mesh refinement tool.

In Zienkiewicz and Zhu’s paper [27], a recovery-based error estimator is developed. This method attempts to use the solution to arrive at an improved gradient in each element and use the difference in this ”recovered” gradient and the FE solution gradient as a measure of the error. This is accomplished by approximating the gradient at element nodes by considering locally higher order basis than the original solution [27]. The paper presents the theory’s development for the linear-elements case but states that ”the procedure is valid for higher order approximating shape functions” [27]. The strength of this *a posteriori* error estimator is stated clearly by the authors: ”it is not only reasonably accurate but whose evaluation is computationally so simple” [27]. The estimator was tested using stress analysis problems and numerical results show that the effectivity index is in general tight about the ideal value of unity.

Zienkiewicz and Zhu expanded on the ideas of their gradient recovery method in two later papers [28] and [29] that describe the method of superconvergent patch recovery and is also referred to as the Z2 estimator. The error estimator, as in [27], is based on the difference between the gradient of the solution with a ”post-processed, recovered, more accurate gradients,” and the original solution gradient[29] but develops the estimator beyond linear solution approximations. In the development it was shown that the ”error estimator will always be asymptotically exact in the energy norm,” [28]. By proving this the authors have developed the theoretical rigorous basis of a method that was previously ad hoc in its derivation. This claim is observed by explicit results from several test problems in which the effectivity index is near one[29]. As in their previous work, this estimator is computationally economical and an effective/reliable estimation of the error and is appealing due to the physically intuitive nature of the estimate.

The aforementioned papers have chiefly concerned themselves with the basic properties of general *a posteriori* error estimators. These estimators are valid for many problem types but may not possess/inhabit tight bounds about the true error. In the following reviewed articles *a posteriori* error estimators are derived for specific classes of problems. By considering a restricted set of equations one may be able to derive tighter upper and lower bounds for the estimator in terms of the true error.

Verfurth introduced two *a posteriori* error estimators of the finite element discretization for the Stokes equations, [24]. The estimators rely on two popular estimate methods: computation of ”suitable norms of the residual,” and ”the solution of local Stokes problems,” [24]. The first approach relies upon the calculation of upper and lower bounds of the residual by use of inequality theorems and the second approach compares the element solution to a local solution on that element. The paper concludes with the error estimators used to drive AMR algorithms. It is determined that both estimators provide reasonable approximations of the error. However, the residual method is preferred for AMR application as it is computationally cheaper but the local problem method, though more expensive to compute, ”yields slightly better quantitative information on the error” [24].

2.3 Error Estimators: The Neutron Transport Equation

The above selection of literature has dealt with both general and problem specific *a posteriori* error estimators. In this section we focus on reported estimators that have been constructed and applied to the discretized neutron transport equation.

Zamonsky, Buscaglia and Azmy developed an "*a posteriori* error analysis of the spatial approximation ... for the one-dimensional Arbitrarily High Order Transport-Nodal method," (AHOT-N) [26]. The estimator is local thereby allowing its application in an AMR routine as each element has access to its own error. The strength of this method lies in the fact that the AHOT-N method allows for "two operations that refine the approximation: reducing the cell size ... or increasing the polynomial order" [26]. The derived estimator is shown to bound the true error and is "a residual-based one ... it reduces to a suitable norm of the residual of the differential equation," [26]. The work provides a theoretical justification of the estimator and several numerical experiments that support its validity. This is shown by considering one-dimensional isotropic scattering problems with fixed meshes and polynomial expansions. It is shown that the local error estimator captures the spatial distribution of the true error. This approach is further explored in [25] and [7].

Expanding on the above work, Duo, Azmy and Zikatanov, considered a new local error estimator for the AHOT-N Method [10], in particular one that handles multiple spatial dimensions. The estimation is achieved by considering a secondary solution that "is obtained on a cell by cell basis" by "solving local problems" [10]. Comparing this second solution to the numerical solution, whose error is to be determined, gives the approximation of the error. This estimator is numerically verified using the Method of Manufactured Solutions (MMS) and is further utilized as the basis for an AMR algorithm.

Madsen developed "a rigorous *a posteriori* error bound for the numerical solutions to time-independent neutron transport problems," [19]. The derived estimator serves to bound "norms of the error function," [19]. Madsen first derives inequalities for the true solution's norms utilizing the source of neutrons and cross section data. The inequalities are mathematically proven and are justifiable from physical interpretation. The error estimators are arrived at by applying the inequalities to the error function corresponding to the numerical solution. One restriction of this estimator is that a " 'smoothing' process must be specified in order to give an approximate solution of the form required," [19] this is due to the nature of the derived inequalities and for computational ease as discontinuities complicate the calculation of the integrals, in the construction of the L_2 norm of the residual. The estimator is verified numerically by considering several test problems.

Similar to the above work, Krivodonova and Flaherty "construct efficient and asymptotically exact *a posteriori* discretization error estimates," [16]. The derived estimators are valid for "hyperbolic problems solved by discontinuous Galerkin methods," [16]. The estimator provides both local and global error estimates. This is verified numerically by noting that the effectivity index tends to unity for several test problems.

In two papers by Ragusa and Wang, [20] and [21], the authors explore several estimators with the intent of driving AMR schemes that are based on Discrete Ordinate DGFEM solutions of the transport equation. In [20] non directional quantities such as the current and scalar flux are compared on two different spatial meshes, a coarse one and its refinement by a factor of two. This is achieved by essentially computing the spatial L_2 norm of the difference between two quantities of interest. Using these local error estimates, the AMR scheme was shown to increase the solution convergence rate versus number of degrees of freedom when compared to uniform refinements. Calculation of the solution on two meshes is computationally inefficient. A successful acceleration was explored in [20] where the converged scattering source on the coarse mesh was used as an initial guess on the refined mesh. In [21] calculation of the coarse mesh is never determined and instead the solution is projected onto the coarser mesh and was shown to be sufficiently accurate for the goals of AMR. The authors in [21] developed two additional estimators to drive the AMR. Utilizing the discontinuities allowed by DGFEM between cell boundaries, an estimator was constructed that measures these "jumps". In a continuous solution these "jumps" should disappear, as the mesh size tends to zero as should the error. Even though the transport solution may contain discontinuities, especially across singular characteristics, it functioned sufficiently well in the scope of their AMR implementation. The final estimator presented in [21] is based on using angle integrated quantities in the adjoint solution to provide weights for the estimate of the error in the direct solution.

Fournier, Le Tellier and Suteau in [13] have applied an estimator derived for hyperbolic problems in [1], to the Discrete Ordinate DGFEM transport equation. The estimator is constructed by considering a modified projection, by exploiting properties of DGFEM solutions, on a basis of nonorthogonal Radau polynomials. A major restriction in the derivation is that the flux and source must belong to C^∞ [13]. This is rare in transport solutions especially across singular characteristics in the solution. However, the proposed estimator has been shown to provide accurate estimates by possessing an effectivity index near unity, within cells that contain no discontinuities. The utility of the estimator is further illustrated by using it and the true error to drive an AMR scheme, in which both error distributions yielded similar results [13].

2.4 Conclusion

This completes the review of the literature. The basic idea of *a posteriori* error estimators was explored. Next error estimates for finite element discretizations were considered. The focus was then brought to error estimators of the neutron transport equation, which is the primary concern of this work.

CHAPTER 3

Transport Discretizations

3.1 Introduction

In this work the proposed error estimators are verified against a true error for selected configurations. In order to accomplish this objective two computer codes are utilized. First, a Method of Manufactured Solutions (MMS) code, in which the angular flux is exactly (analytically) known. From this known flux a distributed source and boundary conditions are generated and used as input to the second code that yeilds the numerical solution via a Discontinuous Galerkin Finite Element Method (DGFEM). The exact formulation and implementation of these codes is elaborated here.

3.2 Discrete Ordinates

Both subject codes start from the same angular discretization called the discrete ordinates approximation (S_N). Potential discretizations in time and energy are irrelevant here as only steady state one-speed problems are considered, respectively. First consider, the one-speed steady state continuous transport equation with isotropic sources and scattering.

$$\vec{\Omega} \cdot \nabla\psi(\vec{r},\vec{\Omega}) + \sigma_t\psi(\vec{r},\vec{\Omega}) = \sigma_s\phi(\vec{r}) + S(\vec{r}) \tag{3.1}$$

Where ψ is the angular flux, ϕ is the scalar flux, S is the distributed source. The total and scattering cross sections are given by σ_t and σ_s, respectively. The unit direction vector is denoted by $\vec{\Omega}$ and ∇ is the del, a differential operator.

The discretization of angle, is straightforward, as the name implies the solution is determined on a finite number of directions. Proceeding with this derivation assuming a Cartesian spatial geometry (as is utilized in this work) and defining a set of angular variables μ, η, ξ, which are the direction cosines of Ω relative to the Cartesian coordinates [18]. With these terms the direction vector Ω may be written as:

$$\vec{\Omega} = \mu\vec{e_x} + \eta\vec{e_y} + \xi\vec{e_z} \tag{3.2}$$

Furthermore, as Ω is a unit vector these direction cosines satisfy $\mu^2 + \eta^2 + \xi^2 = 1$. The discretization occurs by utilizing a finite number of these direction cosines, denoted by:

$$\vec{\Omega_n} = \mu_n\vec{e_x} + \eta_n\vec{e_y} + \xi_n\vec{e_z} \tag{3.3}$$

The actual values of the direction cosines may be chosen in many ways but certain choices have advantages. In this work these values are chosen such that reflective boundary conditions may be satisfied exactly on all external faces. This is accomplished by specifying a set of μ_n, η_n, ξ_n in a single octant and then simply altering their signs when considering the remaining octants. The S_N neutron transport equation can then be written as:

$$\vec{\Omega_n}\nabla\psi_n(\vec{r}) + \sigma_t\psi_n(\vec{r}) = \sigma_s\phi(\vec{r}) + S(\vec{r}) \tag{3.4}$$

Table 3.1: S_4 quadrature angles and weights.

n	μ	η	w
1	0.35002	0.35002	0.08333
2	0.35002	0.86889	0.08333
3	0.86889	0.35002	0.08333

As the scalar flux ϕ is an angle integration of ψ, it must be defined with regard to the angular discretization

$$\phi = \Sigma_{n=1}^{N} w_n \psi_n \tag{3.5}$$

where w_n are quadrature weights.

Throughout this work a S_4 set is used and Table 3.1 shows the particulars, notice that the values for ξ_n are not shown because they may be determined from μ_n and η_n and as only two dimensional problems are studied here.

3.3 Method of Manufactured Solutions

As the exact , MMS, solution is required before determining the strictly numerical solution, it is derived first. The steady-state one-speed discrete ordinates neutron transport equation in 2D Cartesian geometry with isotropic scattering and source is:

$$\mu_n \frac{\partial \psi_n}{\partial x} + \eta_n \frac{\partial \psi_n}{\partial y} + \sigma_t \psi_n(x,y) = \sigma_s \phi(x,y) + q(x,y) \tag{3.6}$$

for $n = 1, \ldots, N$ with boundary conditions, defined on the inflow boundary ∂D^- [22]:

$$\psi_n(x,y) = \psi_{BC,n}(x,y) \text{ if } x, y \epsilon \partial D^- = [x, y \epsilon \partial D, (\mu_n, \eta_n)^T \cdot \vec{n} < 0] \tag{3.7}$$

In the typical MMS formalism the solution is chosen $\psi_n(x,y)$ and then the source $q(x,y)$

and boundary conditions are computed. Naturally the source is given by:

$$q(x,y) = \mu_n \frac{\partial \psi_n}{\partial x} + \eta_n \frac{\partial \psi_n}{\partial y} + \sigma_t \psi_n(x,y) - \sigma_s \phi(x,y) \tag{3.8}$$

Now consider a space independent source Q, that is defined as (primarily for ease of writing the angular flux):

$$Q = q(x,y) + \sigma_s \phi(x,y) \tag{3.9}$$

and choose ψ_n to be the solution to the following auxiliary problem:

$$\mu_n \frac{\partial \psi_n}{\partial x} + \eta_n \frac{\partial \psi_n}{\partial y} + \sigma_t \psi_n(x,y) = Q \tag{3.10}$$

The solution of the transport equation may be discontinuous, in flux value and in value of partial derivatives in space, across the singular characteristic (SC). This is the line of demarcation between regions illuminated by different boundaries and is stated by the points that obey:

$$\bar{y} = |\frac{\eta_n}{\mu_n}|\bar{x} \tag{3.11}$$

where $\bar{x}$ and $\bar{y}$ are defined, assuming the spatial domain is given by $D = [0,X] \times [0,Y]$, as:

$$\bar{x} = \frac{1 - sign(\mu_n)}{2} X + sign(\mu_n) x \text{ and } \bar{y} = \frac{1 - sign(\eta_n)}{2} Y + sign(\eta_n) y \tag{3.12}$$

Now, consider the solution to the auxiliary problem:

$$\psi_n(x,y) = \begin{cases} \psi_{<B,T>,n}(x - sign(\mu_n)|\frac{\mu_n}{\eta_n}|\bar{y}) e^{\frac{-\sigma_t}{|\eta_n|}\bar{y}} + \frac{Q}{\sigma_t}(1 - e^{\frac{-\sigma_t}{|\eta_n|}\bar{y}}) & \text{if } \bar{y} < |\frac{\eta_n}{\mu_n}|\bar{x} \\ \psi_{<R,L>,n}(y - sign(\eta_n)|\frac{\eta_n}{\mu_n}|\bar{x}) e^{\frac{-\sigma_t}{|\mu_n|}\bar{x}} + \frac{Q}{\sigma_t}(1 - e^{\frac{-\sigma_t}{|\mu_n|}\bar{x}}) & \text{if } \bar{y} > |\frac{\eta_n}{\mu_n}|\bar{x} \end{cases} \tag{3.13}$$

where $< B,T >$ and $< R,L >$ refer to the boundary conditions on the bottom, top, right and left edges, respectively [22]. As the solution, and the location of the SCs are known, it is possible to control the order of smoothness of the solution, Cp, across the SC by selecting the appropriate boundary conditions and distributed source (they must also be chosen such that they are always positive, as to retain a physical meaning). This smoothness, Cp, is defined such that p is "the lowest order partial derivative that is not continuous across the SC" [22]. For example, $C0$ and $C1$, the cases studied in this work, refer to solutions where the solution is, i.e the angular flux, discontinuous and where the gradient of the solution is discontinuous across the SC. The SC lines for the S_4 equations are shown in Figure 3.1 for a unit square.

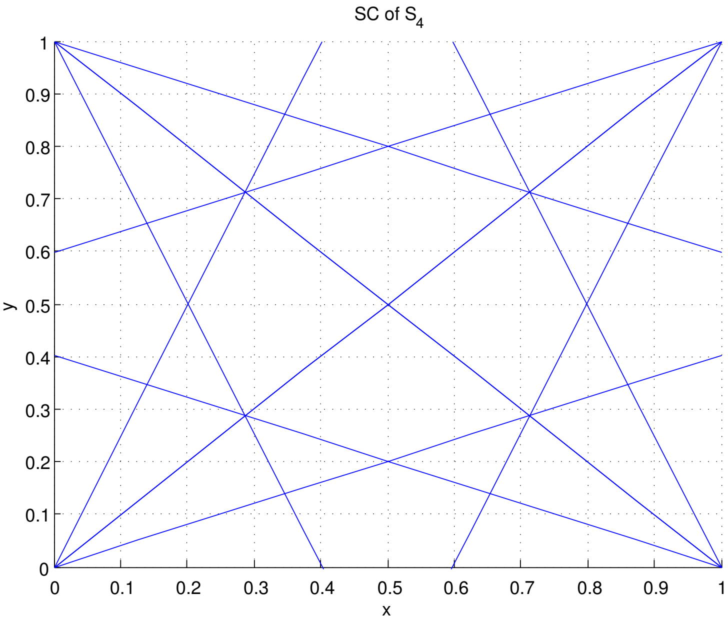

Figure 3.1: Singular Characteristic lines of S_4 on the unit square.

As the aim of this MMS code is for use in error estimator testing, it is beneficial for this code to output results that correspond to the spatial discretization of the numerical solver. To this end, the angular flux in a cell is projected onto a Legendre polynomial space. These moments $\psi_n^{i,j}$ are given in [22] as:

$$\psi_n^{i,j} = \frac{1}{\Delta x \Delta y} \int_{\Delta x} \int_{\Delta y} dx dy P_i(2\frac{x - x_c}{\Delta x}) P_j(2\frac{y - y_c}{\Delta y}) \psi_n(x, y) \tag{3.14}$$

With this definition in hand it is trivial to report the scalar flux and source in the same fashion. Next, consider the formulation of the numerical solution.

3.4 Discontinuous Galerkin Finite Element Method

As with the MMS solution, the Discontinuous Galerkin Finite Element Method (DGFEM) begins with the discrete ordinates transport equation (3.4) and with the same spatial region D, with ∂D^- and ∂D^+ as the inflow and outflow boundaries, respectively. First consider the partitioning of the spatial domain D "into non-overlapping Cartesian cells $(x_{i-1}, x_i) \times (y_{j-1}, y_j)$ with $i = 1, \ldots, I$ and $j = 1, \ldots, J$, covering the whole domain" [23]. As DGFEM allows for the solution to be discontinuous across cell boundaries it is necessary to specify the value of the flux on the cell boundary as either belonging to flux inside the cell, interior trace indicated by superscript $-$, or from fluxes from neighboring cells, exterior trace indicated by superscript $+$. These traces can be interpreted as the limit of the flux on the edge of a cell, either approaching from outside the cell, exterior trace, or from within the cell, interior trace [23].

Before delving into the derivation of the DGFEM it is necessary to define some operator notations. These notations concern the definition of inner products, the first,(3.15) concerns the integration across a cell along one of the dimensions and the second, (3.16), deals with the integration over an entire cell [23].

$$\langle g(x), f(x) \rangle_x = \int_{x_{i-1}}^{x_i} dx g(x) f(x) \tag{3.15}$$

$$(g(x,y), f(x,y)) = \int_{x_{i-1}}^{x_i} \int_{y_{j-1}}^{y_j} dxdy g(x,y) f(x,y) \tag{3.16}$$

With these definitions in hand, consider the weak formulation of the discrete ordinates transport equation, (3.17), for a single cell, (i, j), for a discrete ordinate in the first angular quadrant, $\mu_n, \eta_n > 0$, noting that analogous statements exist for the remaining quadrants, where $v(x, y)$ is the trial space.

$$\begin{aligned}\mu_n[\langle v^{(i,j)}(x_i^+,y),\psi_n^{(i,j)}(x_i^-,y)\rangle_y-\langle v^{(i,j)}(x_{i-1}^+,y),\psi_n^{(i,j)}(x_{i-1}^-,y)\rangle_y]\\+\eta_n[\langle v^{(i,j)}(x,y_j^+),\psi_n^{(i,j)}(x,y_j^-)\rangle_x-\langle v^{(i,j)}(x,y_{j-1}^+),\psi_n^{(i,j)}(x,y_{j-1}^-)\rangle_x]\\-\mu_n(\frac{\partial v^{(i,j)}}{\partial x},\psi_n^{(i,j)}(x,y))-\eta_n(\frac{\partial v^{(i,j)}}{\partial y},\psi_n^{(i,j)}(x,y))\\+(v^{(i,j)},\sigma_t\psi_n^{(i,j)}(x,y)-(\sigma_s\phi(x,y)+q(x,y)))=0\end{aligned}\tag{3.17}$$

One may notice that the upstreaming terms, the exterior trace of the flux on the cell outflow boundaries, are absent. In fact they are not absent, as on outgoing boundaries the exterior and interior traces are set to be equal, in the weak sense, [23] and can be written as:

$$\langle v^{(i,j)}(x_i^+,y),\psi(x_i^-,y)-\psi(x_i^+,y)\rangle_y=0\tag{3.18}$$

With the general expression for the weak form the DGFEM solution can be constructed by specifying the test and trial spaces. These function spaces are equivalent, as it is a Galerkin method, and are a truncated series of Legendre polynomials, up to order Λ. As these functions are defined on the interval $[-1,1]$ it is necessary to scale the spatial variables of D in these functions, which are $\tilde{x}=2(x-x_c)/\Delta x$ and $\tilde{y}=2(y-y_c)/\Delta y$, where x_c, y_c are the cell midpoint coordinates and Δx and Δy are the length of a cell in the x and y direction, respectively [23]. Defining the test and trial spaces as:

$$v_{g,h}(x,y)=P_g(\tilde{x})P_h(\tilde{y})\text{ for }g,h=0,\ldots,\Lambda\tag{3.19}$$

$$\psi(x,y)=\Sigma_{k=0}^{\Lambda}\Sigma_{l=0}^{\Lambda}(2k+1)(2l+1)P_k(\tilde{x})P_l(\tilde{y})\bar{\psi}_{k,l}\tag{3.20}$$

where the Legendre moments of $\psi(x,y)$, $\bar{\psi}_{k,l}$, are:

$$\bar{\psi}_{k,l}=\frac{1}{\Delta x\Delta y}(P_k(\tilde{x})P_l(\tilde{y}),\psi(x,y))\tag{3.21}$$

The final system of discretized S_N equations is arrived at by inserting the test and trial spaces into (3.17). This gives the total number of degrees of freedom of the DGFEM for the entire domain D to be $DoF^{DGFEM} = I \times J \times N \times (\Lambda + 1)^2$ [23].

3.5 MMS and DGFEM Interface

The general procedure for generating a true discretization error between the MMS and DGFEM results is straightforward. First, the MMS code is run with the cross sections, number of angles, domain geometry, size of basis space and the degree of regularity across the SC are defined as inputs. From these inputs the boundary conditions and distributed sources are defined. With all the necessary parameters defined the MMS solution is determined. The output of the MMS code consists of the angular flux, scalar flux and distributed source defined on the selected degree of Legendre polynomials. The DGFEM code then uses the distributed source, boundary conditions and cross sections to arrive at its own solution of the angular and scalar fluxes.

Now that that the MMS and DGFEM fluxes are known the true error can be constructucted in the various forms required by the selection of estimators considered in this work. By solely using the DGFEM solution and its inputs the error estimators are constructed. With the true and estimated errors known they can then be validated.

3.6 Conclusion

Now that the MMS and DGFEM methodologies have been defined and by design share the Legendre polynomials as a basis space (a very beneficial design as will be seen later in this work), one can now turn to generating a set of numerical test cases. These test cases will serve as numerical trials of the estimators studied.

CHAPTER 4

Estimator Rubrics and Test Problems

4.1 Introduction

The estimators considered in this work have as their foundation an explicit mathematical formulation and are often intuitively plausible as valid estimations of the true error. As convincing as their derivation may seem it is essential to test their validity across many problem types. With this large set of estimators and true errors, it is insufficient to judge the effectiveness as either good, bad or mixed. Though some qualitative judgments may be made, a system of quantitative ”yard sticks” must be devised to judge these estimators.Additionally, these rubrics will be utilized to compare the plethora of estimators to each other.

4.2 Estimator Rubrics

In order to quantify the effectiveness of the error estimators two measurements are generally defined, one on the local level and the other on the global level. The local measure is called the effectivity index, θ, and is defined in every spatial cell, (i, j), in [2] as:

$$\theta_{i,j} = \frac{E_{i,j}}{e_{i,j}} \tag{4.1}$$

where $E_{i,j}$ is the estimated error and $e_{i,j}$ is the true error both evaluated in cell i, j for the case, as in this work, that both are always non-negative. The ideal value of θ is unity, this occurs when the estimator exactly agrees with the true error. With this quantity, regions can be identified where the estimator agrees, over estimates or underestimates the true error. In general, regions and estimators that underestimate the error, an effectivity less than one, are considered risky because one is may have more confidence in the solution than actually justified. While the ideal is one, overestimating does not pose the same risks to solution confidence as it conservatively overestimates the error leading to more than necessary caution. However, an estimator that significantly overestimates is undesirable as it renders the estimated error less than useful.

The effectivity index is also considered in a global sense by constructing the average effectivity over the entire domain, denoted by $\bar{\theta}$ and is simply defined as:

$$\bar{\theta} = \frac{1}{nx \times ny} \Sigma_{i=1}^{nx} \Sigma_{j=1}^{ny} \theta_{i,j} \tag{4.2}$$

It is useful to modify the inputs, e and E, of the effectivity index in order to observe the effects. First, by normalizing the true and estimated errors, such that the maximum value in each is one, one can garner how accurately the shape of the error distribution is approximated regardless of its magnitude. This is achieved by simply dividing each error distribution by its maximum value over the entire domain, writing this as:

$$\theta_{i,j}^{N} = \frac{E_{i,j} \times max_{i,j}(e_{i,j})}{e_{i,j} \times max_{i,j}(E_{i,j})} \tag{4.3}$$

The final alteration of $\theta_{i,j}$ is accomplished by excluding the cells that contain a singular characteristic. The equation for this line is known and is given by (3.11). A simple algorithm was constructed to tag these cells for removal from consideration and to clarify, if a SC line passes through a cell corner all cells (four if in the domain interior) sharing this corner were tagged for removal. The exclusion of SC cells is done because one expects the error to be greatest in these cells as it is where the angular flux suffers irregularity that are not possible to represent accurately bu both the MMS and DGFEM solutions that use a set of continuous basis functions. By omitting these cells one may hope to see improvements in the estimators' accuracy and to better understand how the estimators handle these discontinuities.

The main global error measure is taken in the L_2 norm. While this report is primarily concerned with the spatial discretization error in each cell. If the local error estimates are accurate it should follow that, in there totality, the global error should be accurate as well. The global error estimate in general should approximate the true error and at least possess the same trend with mesh (h-) refinement and expansion order (p-) refinement, or expansion order increases, $\Lambda \uparrow$. In discretized solutions there is an expectation that the error should go to zero, $e_{i,j} \to 0$, as the mesh size decreases, $h \to 0$.

The general expression for the L_2 norm of an estimated or true error is:

$$||E||_{L_2} = \sqrt{\Sigma_{i=1}^{nx} \Sigma_{j=1}^{ny} E_{i,j}^2} \tag{4.4}$$

However, some estimators, as in Ragusa and Wang's (Eq. 5.5 and Eq. 5.6), lack the squareing of $E_{i,j}$ in (4.4) as the square is already applied to the integrand employed in their definition and is done to maintain consistency when comparing estimators.

4.3 Test Problems

The MMS-DGFEM code combo provides one with an interesting set of potential test problems. Starting with the restrictions on test problems considered. First only steady-state one-speed two-dimensional problems are considered that have isotropic scattering and sources. Additionally, the problem domain is homogeneous and is discretized into Cartesian domains, limiting one to rectangular regions. As simplifying as this sounds the primary benefit is the ability to construct solutions with known regularity of the solution across the singular characteristics. In this work the $C0$, discontinuous flux, and $C1$, discontinuous gradient of the flux, cases are considered. These are chosen as they are the most prevalent in realistic transport calculations, with $C0$ occurring frequently in shielding problems and $C1$ being prevalent in reactor calculations. The degree of continuity is strongly influenced by the boundary conditions and to a lesser degree by the distributed source. For all $C0$ cases the left and right boundaries deploy constant incident radiation while the top and bottom boundaries are vacuum. For the $C1$ case all boundaries are vacuum. The exact values assigned for the boundary conditions in the test problems are given in Table 4.1.

Table 4.1: Boundary Conditions by scattering ratio and SC continuity

$c = 0.1$	L-R	T-B	$c = 0.9$	L-R	T-B
C0	9.0	0.0	C0	$0.11\bar{1}$	0.0
C1	0.0	0.0	C1	0.0	0.0

The second main class of parameters sampled for the test problems lies in the size of the Legendre Polynomial basis space, Λ, chosen. The values utilized are $\Lambda = 0, 1, 2$. In this work the highest order terms, in x and y, are retained. For example the highest polynomial term kept for $\Lambda = 2$ is x^2y^2. This allows for an intricate surface structure to be used in each computational cell. An interesting result of this work is to see how well these continuous surfaces, i.e. linear combinations of Legendre Polynomials, are able to approximate the irregularities of the true solution across singular characteristics.

Now, turning our attention to the problem geometry, including spatial mesh choices, and cross sections. Two types of problem geometries are considered: square domains (square mesh cells) and high aspect ratio domains (high aspect ratio mesh cells), in this work the aspect ratio is 10:1. These choices are made to represent extremes, with the square being ideal and the high aspect, chosen so large, is likely a poor choice for most calculations. The mesh cells possess the same aspect ratio of the problem domain and by adjusting the length of the domain in x and y effectively varyies $\Delta x, \Delta y$. If one begins with the coarsest mesh, h, the set of meshes considered are uniform refinements by factors of 2, $h_n = \frac{h}{2^n}$, because several estimators require it. The starting mesh size for both the square and high aspect ratio domains is 4×4. To create a square or high aspect ratio domain the length in the x, X, and y, Y, directions are changed. The square case is defined with $X, Y = 1$ and the high aspect ration case is defined using $X = 1$ and $Y = 0.1$.

Continuing with the choice of extremes the cross sections are divided into optically thin ($\sigma_t = 1$) and optically thick ($\sigma_t = 10$) test problems. By increasing the optical thickness one is increasing the expected number of neutron interactions in a cell. The final extreme choice concerns the scattering cross section, σ_s. The cross section types are high scattering or low scattering, and instead of citing these cross sections for each choice of σ_t one can define the scattering ratio, $c = \frac{\sigma_s}{\sigma_t}$. The values of c considered in our numerical tests are 0.1 and 0.9.

These problem variations lead to a large set of test problems, as the choices multiply. A sampling of the various results, scalar flux and sources, follows but first a note on the iterative convergence criteria used for every test problem: the problem is converged when every scalar flux moment satisfies $|\frac{\phi^k_{i,j} - \phi^{k-1}_{i,j}}{\phi^k_{i,j}}| \leq 10^{-10}$, where the superscript denotes the inner iteration step or until $6,000$ iterations is reached. While this convergence criteria is unrealistically tight for practical applications, it is intended here to avoid contaminating the DGFEM solution, hence the true and estimated errors, from iterative issues.

4.3.1 Plots of DGFEM and MMS Scalar Fluxes

A selection of plots from the problems considered is presented here. All plots presented, if applicable, are color-coded plots using the cell centered value of the plotted field in each cell, the scalar flux in this section. Using the cell centered scalar flux, ϕ^{cc}, as an example (recall that the MMS and DGFEM fluxes, and distributed sources use the same Legendre polynomial basis) the cell centered value is constructed from the DGFEM and MMS solutions via:

$$\phi^{cc} = \Sigma_{i=0}^{\Lambda}\Sigma_{j=0}^{\Lambda}(2i+1)(2j+1)\phi_{i,j}P_i(0)P_j(0) \tag{4.5}$$

First, consider the similarity between the MMS and DGFEM solutions in Figure 4.1:

Figure 4.1: MMS(left) and DGFEM(left) plots of ϕ^{cc} for the test problem where $\Lambda = 1$, $\sigma_t = 1$, $c = 0.1$ and continuity $C0$.

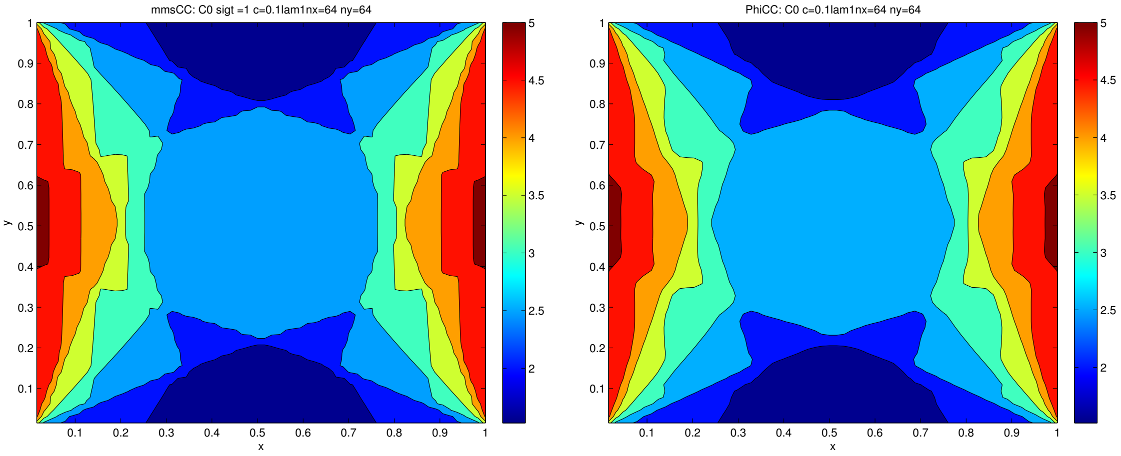

Upon inspection, it is clear that the MMS and DGFEM scalar fluxes generally agree in Figure 4.1. The largest values exist along the left and right boundaries, as expected due to the large boundary source quoted in Table 4.1. In addition the SC lines, recall Figure 3.1, are prominently exhibited by both solutions in Figure 4.1. This is an expected feature of $C0$ cases because the angular flux, from which the scalar flux is computed, is in a sense doubly valued at the SC. The low scattering ratio and small total cross section of this problem also serves to keep the SC lines vibrant by allowing particles to stream more freely without much chance to collide and redistribute over angles to effectively smoothen out the SC edges.

Contrast the flux profile depicted in Figure 4.1 with the same problem specifications except that the left figure has an increased scattering ratio, $c = 0.9$ and that the right figure maintains the $c = 0.1$ value but with $\sigma_t = 10$, in Figure 4.2.

Figure 4.2: DGFEM plots of ϕ^{cc} for the test problems where $\Lambda = 1$ and continuity $C0$. The left figure has $\sigma_t = 1$ and $c = 0.9$ and the right figure has $\sigma_t = 10$ and $c = 0.1$.

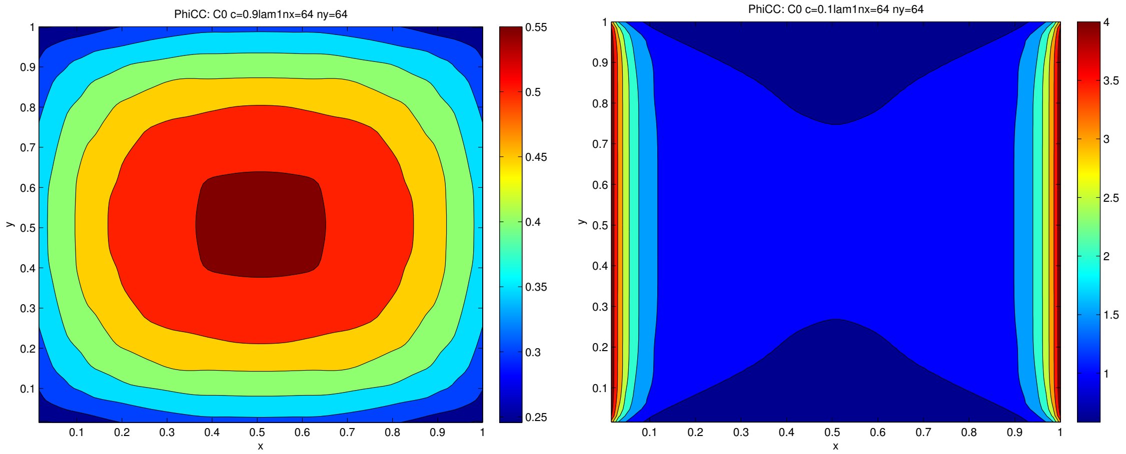

The effect of increasing the scattering ratio serves to smoothen the scalar flux. The discontinuity is still present and one can observe crinkles in the left plot in Figure 4.2, where the SC lines are present. Also the magnitude of the flux is diminished as expected due to the smaller incoming boundary fluxes. In the right plot of Figure 4.2 the effects of increasing the optical thickness are seen by the flux rapidly decreasing with increasing distance from the vertical boundaries.

Now consider the case of $C1$ continuity across the singular characteristics in Figure 4.3 and these are noticeably smoother than those in Figure 4.1. They are very similar in shape and magnitude as expected because the boundary conditions and internal source are the same.

The preceding figures have all been $\Lambda = 1$ cases. Now consider the effects on the solution by varying the expansion order to $\Lambda = 0$ and $\Lambda = 2$ as shown in Figure 4.4. It is apparent that by increasing the expansion order more detail is visible in the flux. Note the improved agreement with increasing expansion order, $\Lambda \uparrow$, between the DGFEM and MMS solutions. This implies improved accuracy with p-refinement, i.e. increasing Λ, for this problem configuration.

Figure 4.3: DGFEM plots of ϕ^{cc} for the test problems where $\Lambda = 1$ and continuity $C1$. The left figure has $\sigma_t = 1$ and $c = 0.1$ and the right figure has $\sigma_t = 1$ and $c = 0.9$.

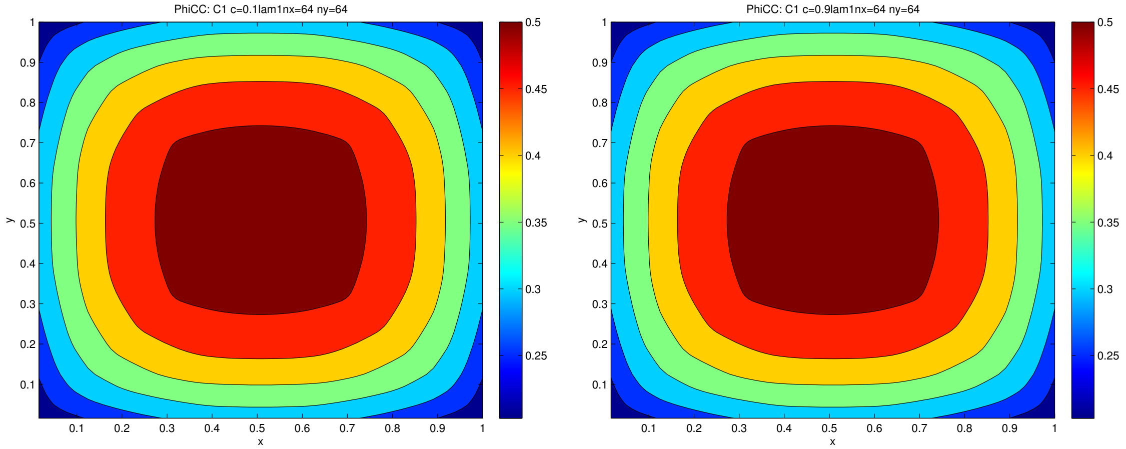

The final variation on the problems considered in this work is the aspect ratio of the computational cells. The 10 : 1 aspect of the computational cell is maintained in the size of the problem where $X = 1$ and $Y = 0.1$. A sample of these cell centered scalar flux profiles for problems is given in Figure 4.5 where we stretched the scale of the y-axis to retrieve a unit square shape of the problem domainl this was done for the ske of improved visibility of the solution's shape.

4.4 Conclusion

This concludes the exhibition of a small selection of all the problem configurations considered in this work. While the spatial form of the scalar fluxes is important when evaluating the error estimators under study, the main quantities of concern are the distinctions between the various continuity conditions, basis size, and cross sections values.

Figure 4.4: DGFEM plots of ϕ^{cc} for the test problems where continuity $C0$, $\sigma_t = 1$ and $c = 0.1$. Left: $\Lambda = 0$. Right: $\Lambda = 2$.

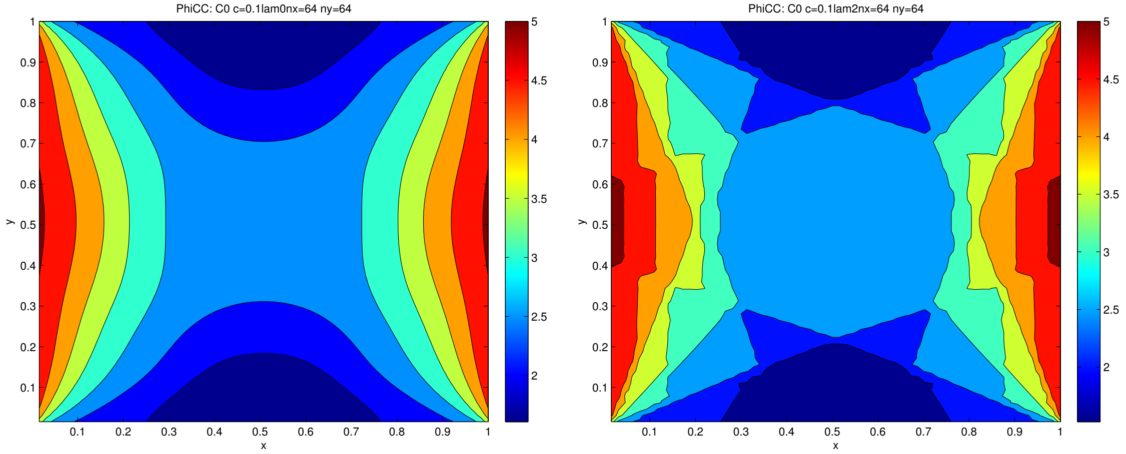

Figure 4.5: DGFEM plots of ϕ^{cc} for the test problems where $\sigma_t = 1$, $c = 0.1$ and $\Lambda = 1$. Left: $C0$. Right: $C1$.

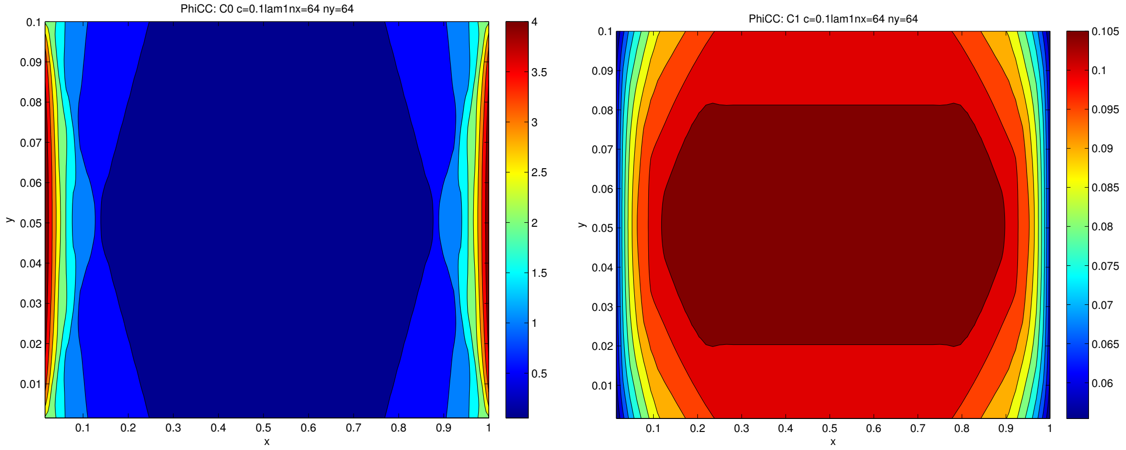

CHAPTER 5

Two Mesh Estimators

Many error estimators are developed in order to drive adaptive mesh refinement algorithms. There are two primary ways to improve the accuracy of a numerical solution: perform the calculation using an increased basis space , e.g. using a higher order polynomial expansion, p-refinement, constructing the solution using more elements, h-refinement, or using a combination of both, hp-refinement. In this work, only estimators that employ h-refinement to generate the second of the two-mesh solutions are considered and in particular those estimators which base there error estimates using a mesh of size h compared to a mesh of size h/2.

The notion that refinement of the spatial mesh can be relied upon to generate a more accurate solution is shown in finite element theory, provided that one is considering cell sizes in the asymptotic regime. In the asymptotic regime the error can be related to a power of the mesh size times a constant as seen in Eq. 5.1, [2], where C is some constant with respect to h and $\bar{\phi}$ is the true solution.

$$e(h) = Ch^p = \phi(h) - \bar{\phi} \tag{5.1}$$

This expression provides formal justification that the error in the solution decreases as the mesh is refined. However, the terms in this expression are not generally known and an approximation must be made. Typically $\phi(h/2)$ is used instead of the unknown $\bar{\phi}$ and Eq. 5.1 shows that $\phi(h/2)$ is a more accurate flux than $\phi(h)$ when h is in the asymptotic regime. This yields an approximation of the error that is the basis of the error estimators considered here.

There is a drawback to this form of estimator as it generally underestimates the true error, $e(h)$. It can be seen that $\phi(h) - \phi(h/2) = e(h) - e(h/2)$ and clearly $e(h) - e(h/2) \leq e(h)$. This can also be explained graphically as in Figure 5.1

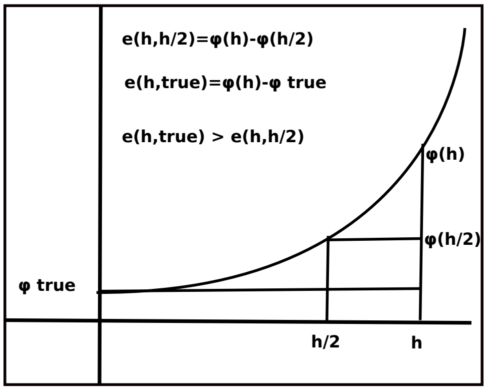

Figure 5.1: A graphical representation showing how two mesh based estimators generally underestimate the true error. Provided h is in the asymptotic convergence regime.

where the error between two meshes, h_1 and h_2, is given by $e(h_1, h_2) = \phi(h_1) - \phi(h_2)$ and "true" corresponds to $h = 0$.

Even with this propensity to underestimate, these estimators are still useful, considering the AMR function they were designed to support. When performing AMR one typically has other meshes on hand to utilize for the comparison and one is more interested in discriminating between regions of greater and lesser error. Therefore the mark of a superior estimator of this nature is that it capture the error distribution accurately.

Given the theoretical limitations, propensity to underestimate the error, of this class of estimators, the normalized effectivity index will be the primary metric because the distributions of the true and estimated error may be similar; perhaps differing by the constant C. There are points in the domain where the error is overestimated. This can be attributed to cells that are traversed by singular characteristics. These cells are not in the asymptotic regime because they contain irregularities and a set of continuous basis functions can never capture these. Now, consider two variations of the two mesh type of error estimator.

5.1 Cell Centered Estimator

When determining a numerical solution on a given spatial mesh, there is an expectation that the accuracy of the solution will increase as the size of spatial cell decreases. The estimator considered here, as well as others in this work, utilizes the effects on the accuracy of the solution if the spatial mesh is refined, uniformly by a factor of two. As this work is concerned with spatial discretization errors, an angle integrated quantity, namely the scalar flux ϕ, is chosen as the basis of this estimator E. Given the value of the h mesh (coarse) scalar flux at a cell center (cc), one may suppose that the average of the $\frac{h}{2}$ mesh (refined) cell centered scalar flux may better approximate this value. This is accomplished by taking the absolute difference between the value of the flux on the h mesh and the averaged value of the scalar fluxes on the $h/2$ mesh. Writing this estimator for the two dimensional case, for an arbitrary cell on the h mesh, gives:

$$E = |\phi_h^{cc} - avg(\phi_{h/2}^{cc})| \tag{5.2}$$

This is the basic formulation of the Two-Mesh Cell-Centered estimator. Now, writing Eq. 5.2 explicitly by utilizing the form of the Legendre polynomial expansion of the solution and for a h-mesh cell (i, j), yields:

$$E_{i,j}^{2M} = |\Sigma_{l=0}^{\Lambda}\Sigma_{k=0}^{\Lambda}(\phi_{h,i,j}^{l,k} - \frac{1}{4}(\phi_{\frac{h}{2},2i,2j}^{l,k} + \phi_{\frac{h}{2},2i-1,2j}^{l,k} + \phi_{\frac{h}{2},2i,2j-1}^{l,k} + \phi_{\frac{h}{2},2i-1,2j-1}^{l,k})P_k(0)P_l(0))| \tag{5.3}$$

The true error, e, used for comparison is simply the cell centered error in the solution between the DGFEM and MMS solutions and is given explicitly by:

$$e_{i,j}^{2M} = |\Sigma_{l=0}^{\Lambda}\Sigma_{k=0}^{\Lambda}(\phi_{h,i,j}^{l,k} - \phi_{h,i,j}^{MMS,l,k})P_l(0)P_k(0)| \tag{5.4}$$

The basic assumption made in this estimator is that the DGFEM solution on the $\frac{h}{2}$-mesh acts as a superior approximation of the true solution than does the DGFEM solution on the h-mesh and therefore the difference of the fluxes on these two meshes serves as an approximation of the error. Before proceeding to the examination of numerical cases, some weaknesses of this estimator are readily apparent. The blatantly obvious one, is the requirement that in order to obtain E on the h mesh one must determine, a presumably more accurate, solution on the $\frac{h}{2}$ mesh. This is of course computationally expensive. There are two approaches, though not considered in this work, that may make this estimator more computationally appealing. First, one may use the scalar flux solution on the h mesh as the initial guess of the scalar flux on the $\frac{h}{2}$ mesh, hopefully reducing the number of iterations and computational cost needed to solve for the $h/2$ flux. Second, one may only solve on the $h/2$-mesh and then project the solution onto the h-mesh in order to obtain an approximation of the h-mesh solution. Clearly this requires that the original $h/2$ mesh solution be sufficiently accurate if the h solution is to be trusted for generating estimates of the error. There is some promise for use in an adaptive mesh refinement scheme, where one may have these different mesh solutions on hand.

5.1.1 Estimator Validation

Now consider an example of this estimator and the corresponding true error in Figure 5.2. First note that the estimator and the true error have similar magnitudes spanning the range 10^{-4} to 10^{-1}. Also traces of the SC lines are evident in the plots and comprise the regions of greatest error. Finally, the two plots share symmetries that are present in the scalar flux, upon which they are based.

The effectivity index over the spatial domain, using the true and estimated errors that are

Figure 5.2: Two Mesh errors: Log_{10} scale of $C0$, $\sigma_t = 1$, $c = 0.1$ and $\Lambda = 1$ case. Left: estimator Right: true error.

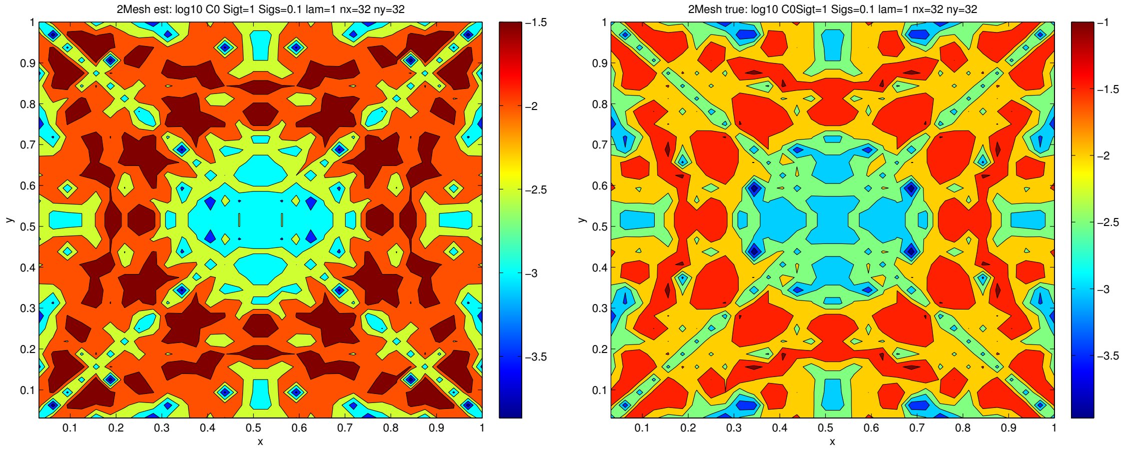

depicted in Figure 5.2, is given in Figure 5.3. The SC lines are visible and the effectivity index is fairly uniform along them. Unlike the Madsen estimator presented in Sec. 6.2, the two mesh estimator does not provide an absolute upper bound of the error as evident from the effectivity index falling below one over most of the problem domain, implying that this estimator is not conservative, i.e. exaggerates confidence in the numerical solution's accuracy.

Figure 5.3: Two Mesh effectivity index: Log_{10} scale of $C0$, $\sigma_t = 1$, $c = 0.1$ and $\Lambda = 1$ case.

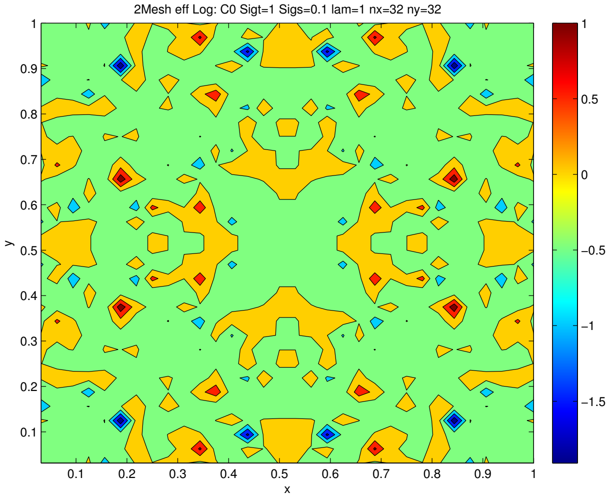

Now, consider how the effectivity index changes for the same case but with increasing Λ in Figure 5.4. There are general improvements as $\Lambda = 0 \to 2$, in that the effectivity index is initially peaked below the ideal value of $\theta = 1$ and then moves towards it. In the $\Lambda = 2$, a greater fraction of the effectivities has moved to $\theta = 1$ and greater, which constitutes change in the better direction as it is conservative to overestimate the error.

Figure 5.4: Two Mesh effectivity index: log scale for nx,ny=32 $\sigma_t = 1.0$, $C0$ and $c = 0.1$. Left: $\Lambda = 0$, Right: $\Lambda = 1$, Bottom: $\Lambda = 2$.

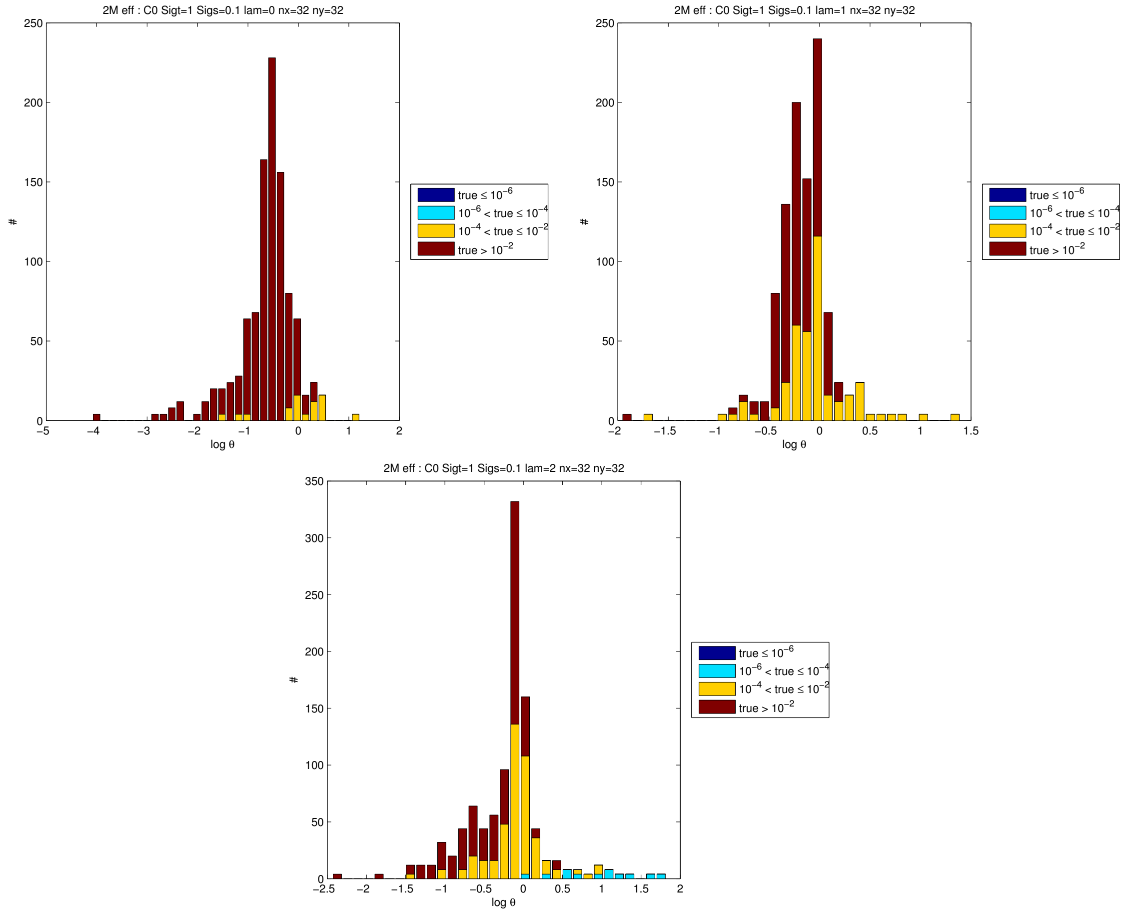

The results are already promising for this estimator but now we test the similarity of the true and estimated error distributions with the normalized effectivity index in Figure 5.5 (note: there are slight differences due to shifting of binning and arises in Matlab between using hist and bar plotting options). The overall result is that true and estimated error have similar distributions by noting that the normalized effectivity index is close to unity. The effect of moving the peak of the distribution is most notable for the $\Lambda = 0$ case and becomes less significant for the higher orders, which already showed strong agreement without normalizing the effectivity index.

Figure 5.5: Two Mesh normalized effectivity index: log scale for nx,ny=32 $\sigma_t = 1.0$, $C0$ and $c = 0.1$. Left: $\Lambda = 0$, Right: $\Lambda = 1$, Bottom: $\Lambda = 2$.

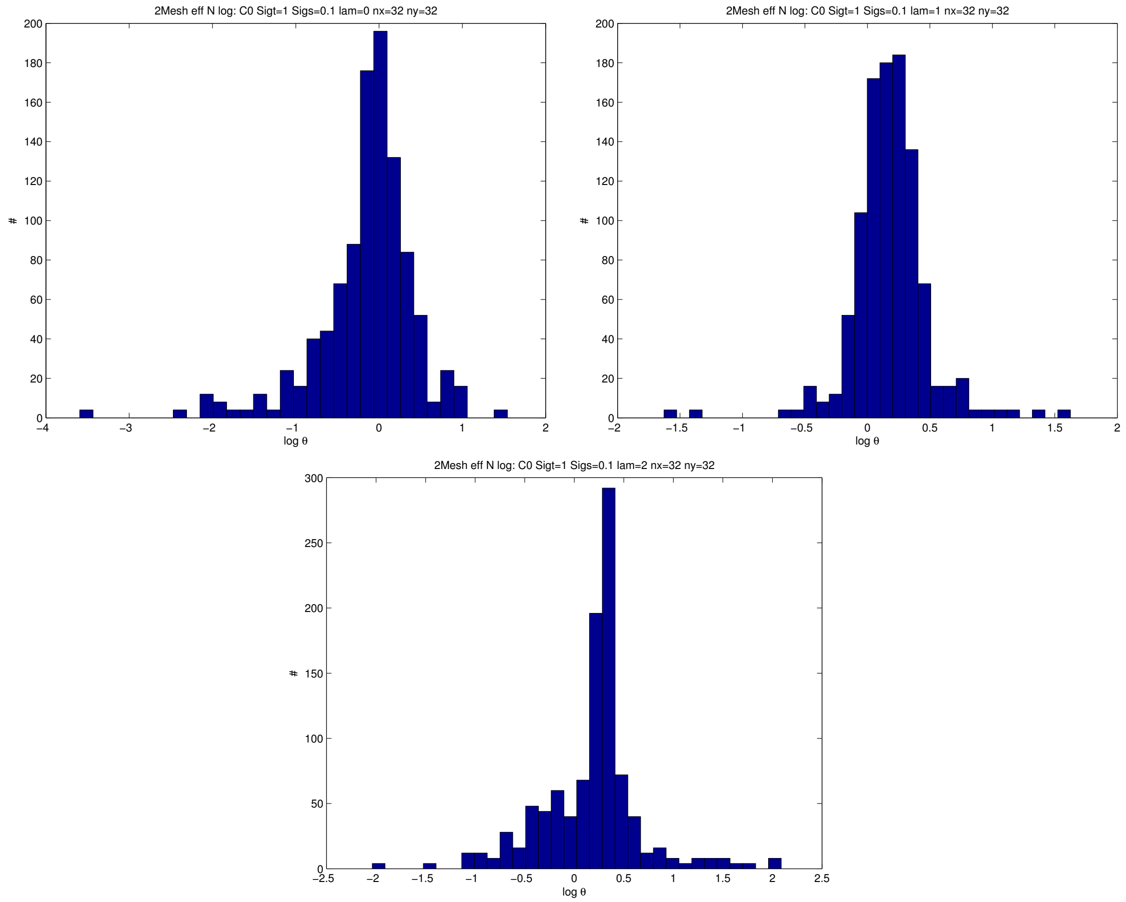

Additionally, the effects of removing the error in cells that contain SC lines from the binning function on the effectivity index is observed in Figure 5.6 by comparison with Figure 5.4. Overall, in cells containing SC lines, this estimator underestimates the true error. This is observed by noting that the majority of the distribution removed, lies below $\theta = 1$ ($log_{10}(\theta) = 0$).

Figure 5.6: Two Mesh effectivity index with the error in SC cells removed: log scale for nx,ny=32 $\sigma_t = 1.0$, $C0$ and $c = 0.1$. Left: $\Lambda = 0$, Right: $\Lambda = 1$, Bottom: $\Lambda = 2$.

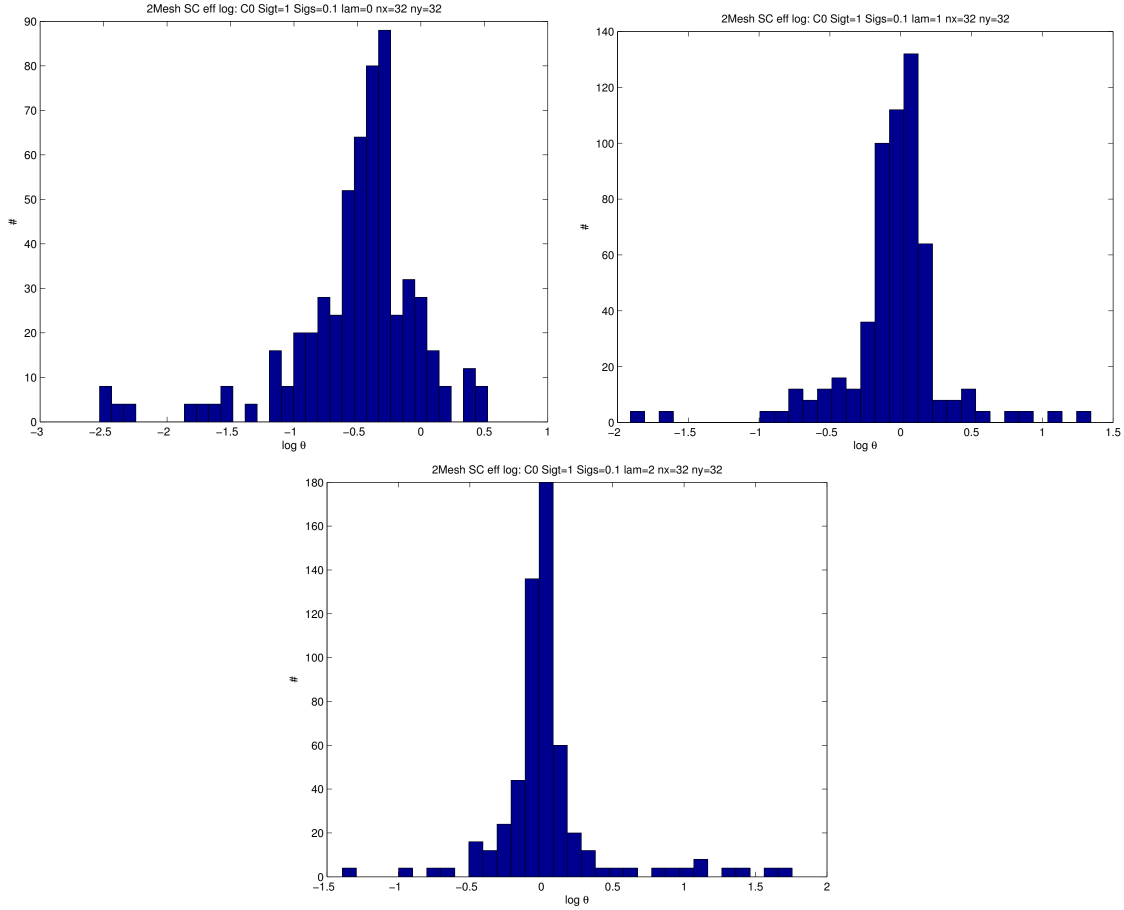

Additional effects on the effectiveness of the error estimator occurs when considering the effects of continuity across singular characteristics. In general the true and estimated error of the solution is greater for C0 than for C1 cases. In addition the error is generally underestimated more for $C1$ cases as the arguements from Eq. 5.1 hold for this degree of regularity because the continutous basis functions can capture the continuous value of the flux across the SC and therefore can lie in the aymptotic regime; eventhough the discontinuity in the first derivative cannot be modeled exactly.

5.1.2 Conclusion

Overall, this is a very effective and cheap estimator, provided one has two mesh solutions, to compute. For higher order Λ the effectivity index is near its ideal value and the upper outliers are explainable by the true error being exceptionally small.

5.2 Ragusa and Wang Estimator

Following the current theme of two mesh based estimators, consider one of the estimators proposed by Ragusa and Wang in their work [20] and [21]. The basic structure of the estimator, E, considers the difference between two angle integrated quantities, such as the current or scalar flux, computed in the L_2 norm in the spatial variables [20]. Angle integrated quantities are chosen because the angular flux is often not stored and one is interested in spatial estimates of the error. The difference considered in the L_2 norm is between quantities that have been calculated on a h level mesh and on a $\frac{h}{2}$ level mesh. Writing the basic form of this estimator using the DGFEM scalar flux, for an arbitrary spacial cell is:

$$E = \frac{\int_K (\phi_h - \phi_{\frac{h}{2}})^2 dA}{\int_D (\phi_h)^2 dA} \tag{5.5}$$

where K is spatial extent of the cell in question and D is the entire spatial domain. The denominator is present because of the intent of the authors to utilize this estimator to drive an AMR routine and this terms acts to the scale resulting error estimate for consistent comparisons to their refinement criterion. We retain this term in the present work to be consistent with [20] and [21]. The same scaling factor is also incorporated in the calculation of the true error in Eq. 5.6.

$$e = \frac{\int_K (\phi_h - \phi_h^{MMS})^2 dA}{\int_D (\phi_h)^2 dA} \tag{5.6}$$

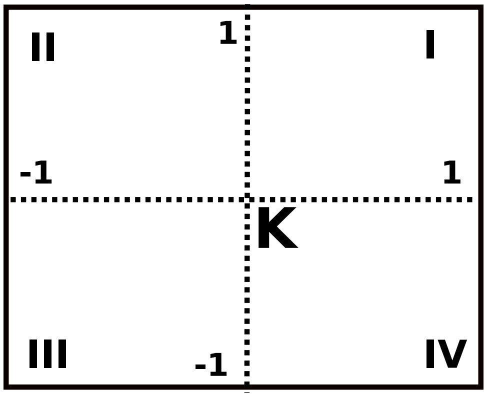

Figure 5.7: Quadrant map for the h-level element K.

With these definitions in hand, let us consider how they are implemented in this work. The use of Legendre polynomials as the expansion basis of the solution loses its utility, namely orthogonality, in the calculation of the numerator. The orthogonality is lost because integrations are done between Legendre moments that do not share the same spatial domain entirely, namely the $h/2$ cell is a subdomain of the h cell. Recall, that in each cell the Legendre polynomials are defined from $\bar{x}, \bar{y} \epsilon [-1, 1]$ and there is a cell by cell transformation from the true spatial coordinates to these local bared or basis ones. Given that there are four $\frac{h}{2}$ mesh cells in any h-level K cell, the integration is broken up into 4 quadrants as shown in Figure 5.7. Within each of these quadrants, the $\frac{h}{2}$ scalar fluxes are integrated over the range $[-1, 1]$ with respect to both x and y and the h mesh scalar fluxes must be integrated over a subspace of this range, depending on the quadrant in question.

To facilitate quick numerical calculations of the estimator the values of all potential integrals comprising products of various order Legendre Polynomials were determined using Mathematica. To perform this calculation the arguments of the $\frac{h}{2}$-mesh were defined such that they spanned the full Legendre Polynomial range ,$[-1, 1]$, while the h-mesh arguments were constrained to the limits as defined by the quadrant map, Figure 5.7. These arguments are given in 5.1 and for the given ranges of x, y it is clear that $\bar{x}, \bar{y}$ cover the desired range of $[-1, 1]$.

Table 5.1: Quadrant integration limits and arguments

Q	x-range	$\bar{x}$-arguments	y-range	$\bar{y}$-arguments
I	[0,1]	$2x-1$	[0,1]	$2y-1$
II	[-1,0]	$2x+1$	[0,1]	$2y-1$
III	[-1,0]	$2x+1$	[-1,0]	$2y+1$
IV	[0,1]	$2x-1$	[-1,0]	$2y+1$

The integration values, denoted by c, are given by:

$$c^{Q,h,\frac{h}{2}}_{i,j,k,l} = \int_{Q_x} dx \int_{Q_y} dy P_i(\bar{x_Q}) P_j(\bar{y_Q}) P_k(x) P_l(y) dA_Q \tag{5.7}$$

These coefficients are only necessary for the integration of terms involving Legendre Polynomials on the two meshes. The integrations of like meshes simply use the Legendre polynomial orthogonality, denoted by c with the proper superscript, with the proper dA for each mesh level. With this definition in hand, the numerator of estimator can be written, for a single cell, as:

$$\begin{aligned} E_{numerator} = \Sigma^{\Lambda}_{i=0}\Sigma^{\Lambda}_{j=0}\Sigma^{\Lambda}_{k=0}\Sigma^{\Lambda}_{l=0}(\phi^{h}_{i,j}\phi^{h}_{k,l}c^{h,h}_{k,l,g,h} \\ +\Sigma^{IV}_{Q=I}(-2\phi^{Q,\frac{h}{2}}_{i,j}\phi^{h}_{k,l}c^{Q,h,\frac{h}{2}}_{i,j,k,l} \\ +\phi^{\frac{h}{2}}_{i,j}\phi^{\frac{h}{2}}_{k,l}c^{\frac{h}{2},\frac{h}{2}}_{k,l,g,h})) \end{aligned} \tag{5.8}$$

The denominator suffers from no such complications since it involves only the h-mesh, simply using the Legendre polynomial integration values.

This completes the error estimator evaluation as per the original paper by Ragusa and Wang [20]. In order to bring this estimator into compliance with the remaining estimators considered in this work, it must be modified such that the error is considered, not the error squared. This is accomplished simply by taking the square root of E and e. These new quantities are denoted by E^{RW} and e^{RW} to distinguish them from the other estimators.

$$E^{RW} = \sqrt{\frac{\int_K (\phi_h - \phi_{\frac{h}{2}})^2 dA}{\int_D (\phi_h)^2 dA}} \tag{5.9}$$

$$e^{RW} = \sqrt{\frac{\int_K (\phi_h - \phi_h^{MMS})^2 dA}{\int_D (\phi_h)^2 dA}} \tag{5.10}$$

An example of these errors, (5.9) and (5.10), is reported in Figure 5.8 (note: the asymmetries in the figure are due to small differences of the order 10^{-15} in absolute differences, prior to taking the square root). Upon first glance there are several features that are promising. First, the estimator and the true errors are on similar scales in terms of magnitude spanning the range from 10^{-5} to 10^{-3} . Additionally the SC lines are prominent and include the area of largest error, which is expected. Note that the difference in the true error plot in Figure 5.2 and Figure 5.8 is a consequence of the different formula used to compute the cell-value for the error from the same MMS and DGFEM data for that cell, namely Eq. 5.4 and Eq. 5.10, respectively.

Figure 5.8: Ragusa and Wang errors: Log_{10} scale of $C0$, $\sigma_t = 1$, $c = 0.1$ and $\Lambda = 1$ case. Left: estimator Right: true error.

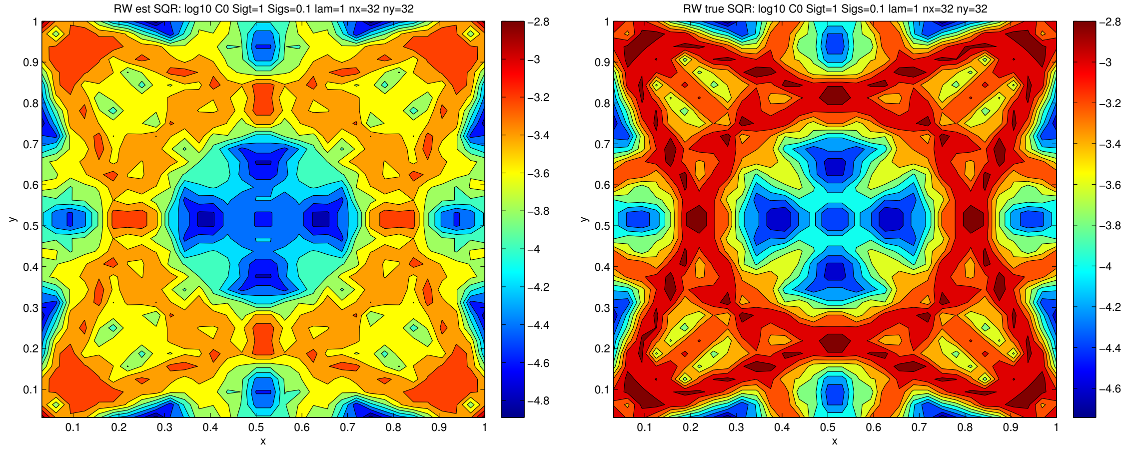

The Ragusa and Wang effectivity index, using the data ploted in Figure 5.8, is given in Figure 5.9. It shows considerable agreement between the estimated and true errors. In particular notice the use of a linear scale for the effectivity index. It is clear from Figure 5.9 that the error estimator generally underestimates the true error and only overestimates in a small fraction of the domain.

Figure 5.9: Ragusa and Wang effectivity index: Linear scale of $C0$, $\sigma_t = 1$, $c = 0.1$ and $\Lambda = 1$.

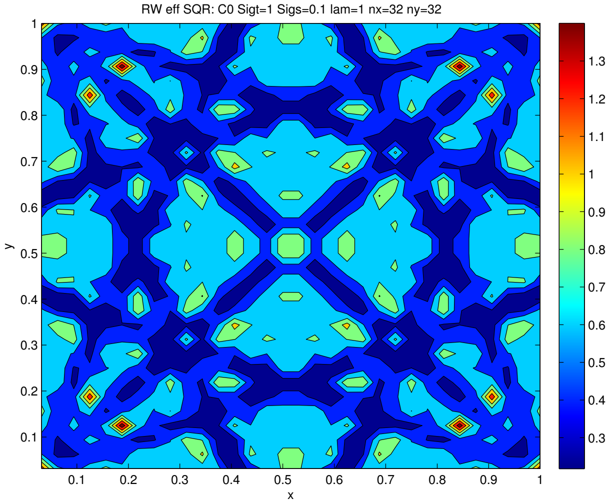

5.2.1 Estimator Validation

For the bulk of this discussion the expansion basis $\Lambda = 1$ is used. Most of the conclusions hold equally well for the cases of $\Lambda = 0, 2$. In general, increasing Λ serves to tighten the effectivity index distribution horizontally and by doing so heightens the peak of the distribution. This effect is observed for the Ragusa and Wang estimator in Figure 5.10. First noting that from $\Lambda = 0 \rightarrow 2$, the peak of the distribution increases, approximately, from 300 to 800. Second and perhaps more importantly, the spread of θ decreases with increasing Λ. This occurs mostly on the lower end for all Λ but the upper end is significant as $\Lambda = 0 \rightarrow 1$. This effect holds for all cases of continuity and cross sections. Also, the peak shifts closer to its ideal value of $\theta = 1$ with increasing Λ, wherein $log_{10}(\theta)$ increases from -0.5 for $\Lambda = 0$ to -0.2 for $\Lambda = 1$ to -0.15 for $\Lambda = 2$.

The effectivity index measures how close the true and estimated errors are in value. It

Figure 5.10: Ragusa and Wang effectivity index: log scale for nx,ny=32 $\sigma_t = 1.0$, $C0$ and $c = 0.1$. Left: $\Lambda = 0$, Right: $\Lambda = 1$, Bottom: $\Lambda = 2$.

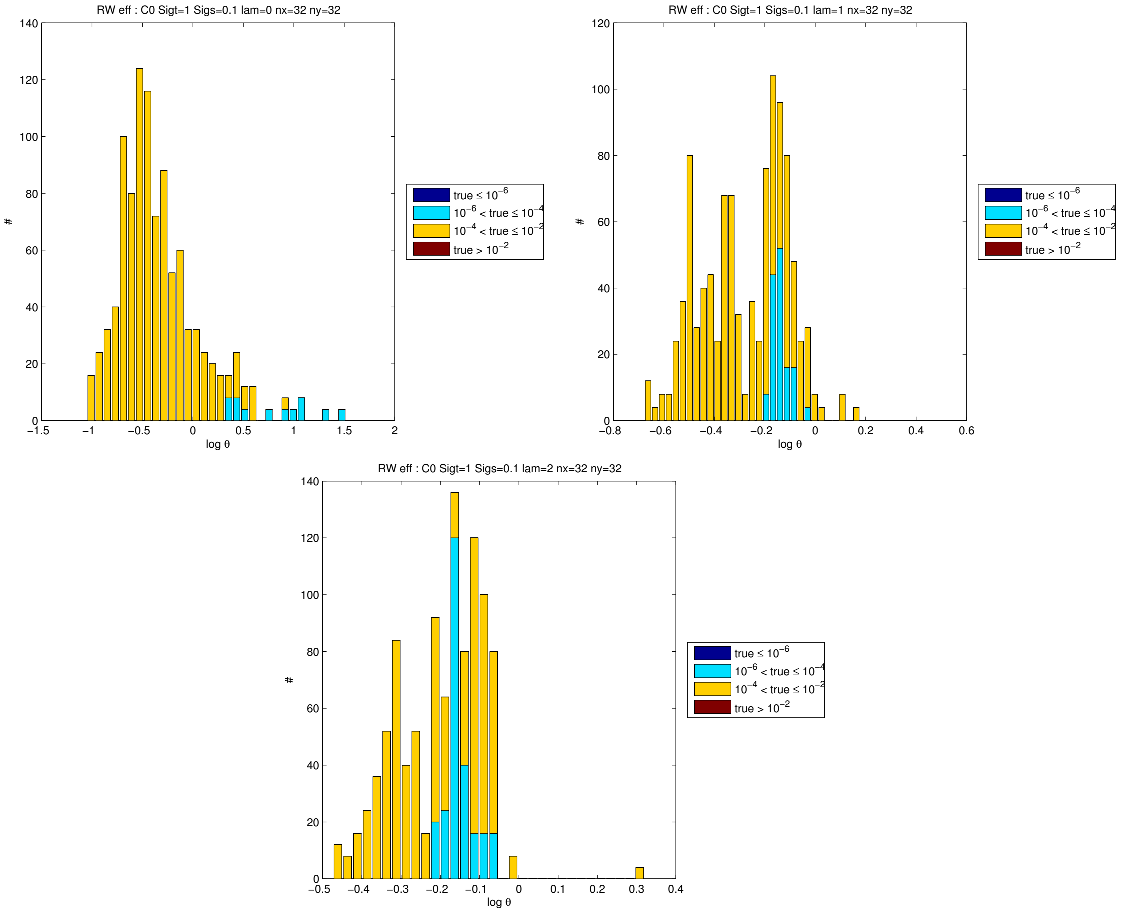

is useful to also determine if the errors share a similar distribution, regardless of magnitude. To measure this consider the "normalized" effectivity index, as defined in Eq. 4.3 but using E^{RW} and e^{RW}. As seen in Figure 5.11 , in comparison to Figure 5.10, the distribution and its peak, are shifted to the right and in general is more centered about $log(\theta) = 0$, this shows that overall the normalized Ragusa and Wang estimator captures the shape of the distribution but underestimates the value of the true error.

Continuing with the specified problem case, one can observe the effect of removing cells that contain SCs in Figure 5.12. In general, for all cases of Λ, by removing the SC lines the distribution of the effectivity index is tightened by the removal of some of the extreme minimum

Figure 5.11: Ragusa and Wang Normalized effectivity index: log scale for nx,ny=32 $\sigma_t = 1.0$, $C0$ and $c = 0.1$. Left: $\Lambda = 0$, Right: $\Lambda = 1$, Bottom: $\Lambda = 2$.

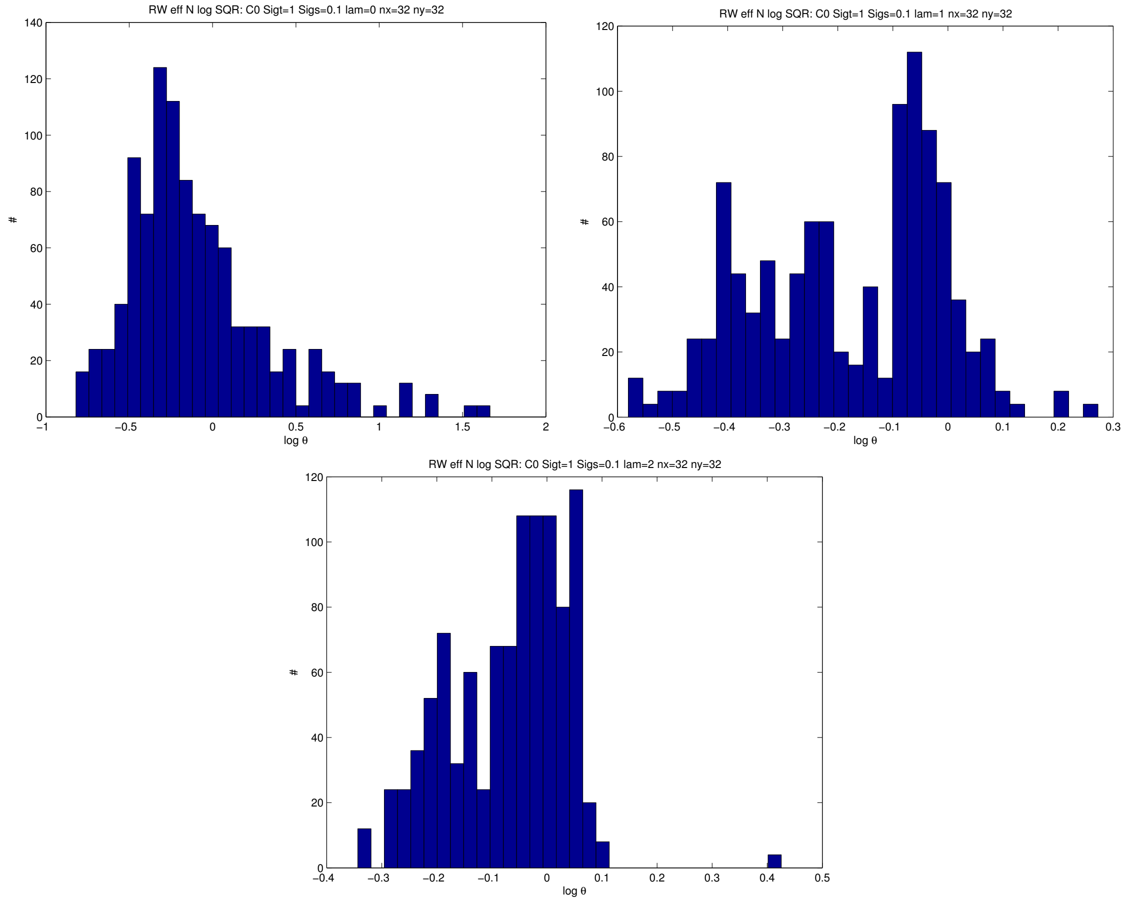

and maximum values. Coupling this with the normalized effectivity, one ought to observe an improvement of the distribution.

5.2.2 Conclusion

In general this estimator behaves similarly to the Cell Centered estimator which is expected but outperforms it as it uses the full flux as defined in each element. When comparing the range of effectivities between the two estimators it is observed that Ragusa and Wang is tighter about $\theta = 1$ as observed in the $\Lambda = 1$ case where the Cell Centered estimator's effectivities range from 10^{-2} to $10^{1.5}$ and Ragusa and Wang's range from $10^{-.6}$ to $10^{.2}$. Though the Cell Centered is

Figure 5.12: Ragusa and Wang effectivity index with SC removed: log scale for nx,ny=32 $\sigma_t = 1.0$, $C0$ and $c = 0.1$. Left: $\Lambda = 0$, Right: $\Lambda = 1$, Bottom: $\Lambda = 2$.

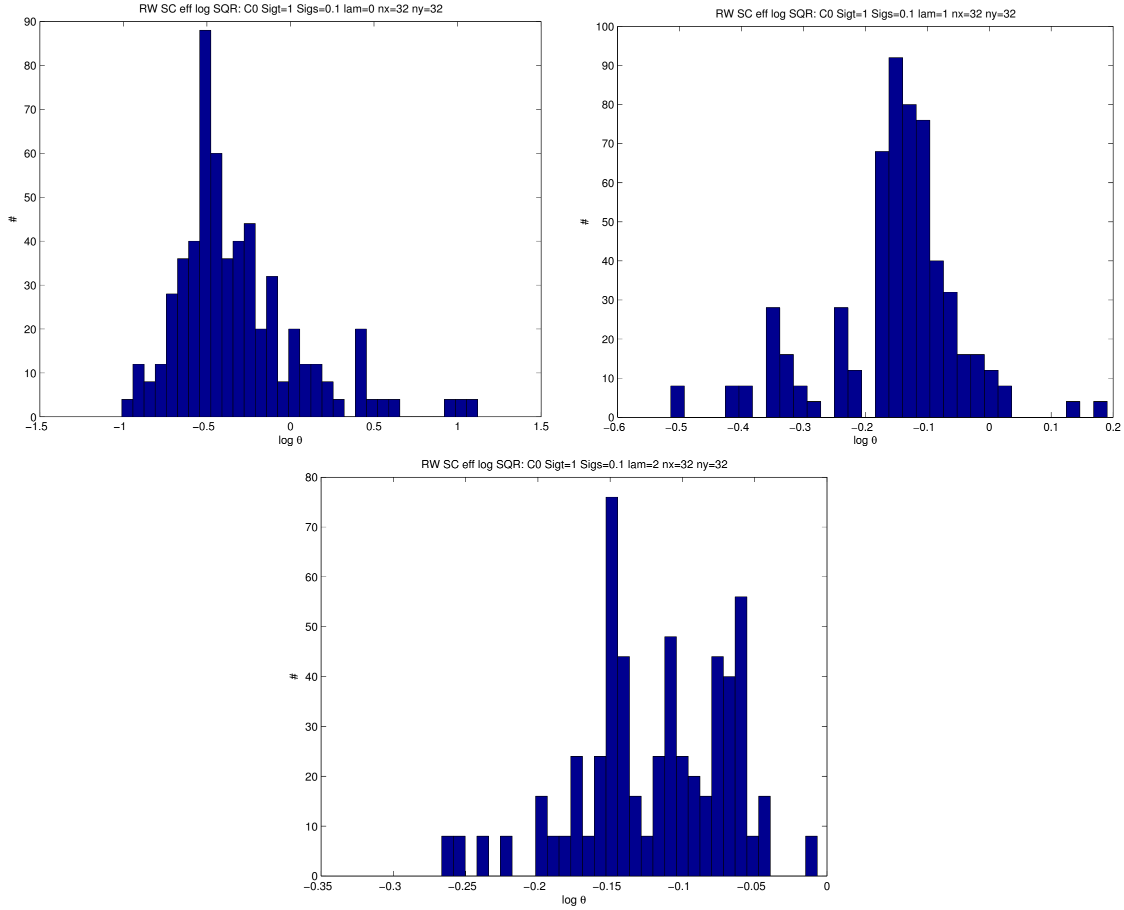

RW SC eff log SQR: C0 Sigt=1 Sigs=0.1 lam=0 nx=32 ny=32

RW SC eff log SQR: C0 Sigt=1 Sigs=0.1 lam=1 nx=32 ny=32

RW SC eff log SQR: C0 Sigt=1 Sigs=0.1 lam=2 nx=32 ny=32

computationally faster to compute the Ragusa and Wang estimator is not prohibitively slower.

CHAPTER 6

Residual Based Estimators

Another widely used method of constructing error estimators is achieved by considering the residual. The residual is the imbalance in the exact (undiscretized) problem when the numerical solution is substituted in place of the exact. For the transport equation the residual, R, is expressed as $R = S - L\psi$, where S is the distributed source, L is the undiscretized transport operator and ψ is the numerical angular flux. It is not the error in the solution, $e = \bar{\psi} - \psi$, but the two can often be related. The benefit of residual methods is that all quantities are known and in general, if a problem is well-posed, a larger residual typically corresponds to a larger error. The ways these two quantities can be related, to obtain an estimation of the error, is the focus of this chapter.

There are several properties of the residual that arise from considering Galerkin finite element methods. Chief among these is Galerkin orthogonality, which states that the error and the basis space are orthogonal. If v_Λ is the basis space then the DGFEM transport formulation can be written in the bilinear form as stated in Eq. 6.1,

$$L(\phi, v_\Lambda) = S(v_\Lambda) \tag{6.1}$$

where $L(\phi, v_\Lambda) = S(v_\Lambda)$ is DGFEM weak formulation, Eq. 3.17, rewritten in the bilinear form where the scattering and distributed sources have moved to the right hand side and rewritten as $S(v_\Lambda)$.

Now, expressing the property of Galerkin orthogonality in this form yields $L(e, v_\Lambda) = 0$ [2]. Using this property one can show that the residual, $R(\psi, v_\Lambda) = S(v_\Lambda) - L(\psi, v_\Lambda)$, in this form is zero as expressed in Eq. 6.2 and noting that this operator is linear,

$$\begin{aligned} L(e, v_\Lambda) &= L(\bar{\psi}, v_\Lambda) - L(\psi, v_\Lambda) \\ &= S(v_\Lambda) - L(\psi, v_\Lambda) \\ &= R(\psi, v_\Lambda) \\ &= 0 \end{aligned} \tag{6.2}$$

where $\bar{\psi}$ is the exact representation of the angular flux.

Many finite element error estimators are constructed utilizing this result. However, for the estimators considered in this work the discrete ordinates operator is utilized because it does not yeild a zero valued residual. Now, consider two estimators that are founded on the use of residuals.

6.1 Residual Source (LE=R) Estimator

Consider a new error estimator inspired by the work by Madsen in [19]. This new estimator is based on constructing the residual of the DGFEM solution and using it as a distributed source to solve for the error. This procedure, without making additional simplifications, does require one to run an additional transport solve of a problem equivalent in scale to the original problem. While time consuming, it could be computationally cheaper to the transport solves required for the $\frac{h}{2}$ mesh error estimators by a factor of four, in two-dimensional geometry. Additionally, one could solve for the error using a lower order of basis functions since the error estimator need not be computed to the same high accuracy as the solution itself.

Now, proceeding with the derivation of this estimator. Let ψ be the true angular flux solution and $\tilde{\psi}$ be the numerical angular flux. The error, e, can be written as $e = \psi - \tilde{\psi}$. Now applying the transport operator L to the error gives Eq. 6.3.

$$Le = L(\psi - \bar{\psi}) \tag{6.3}$$

Using the linearity of the operator and that the true solution satisfies $L\psi = S$, where S is the distributed source, gives the equation to solve for the error in Eq. 6.4. Notice that the operator is now $\tilde{L}$, denoting that it is the DGFEM approximation, such that the DGFEM code can be reutilized to solve for the error, as opposed to the spatially continuous Discrete Ordinates operator L that is used to compute the residual. By using the operator $\tilde{L}$, the approximate error, E, is now solved for.

$$\tilde{L}E = S - L\bar{\psi} \tag{6.4}$$

To complete the operation the boundary conditions must be defined. As the boundary condition to the original problem is exactly known, there can be no "inflow of error". This yields vacuum boundary conditions for all explicit boundary conditions. With the transport problem now defined one can solve for the error in this manner.

With the conceptual derivation complete, one must consider its implementation into the DGFEM framework utilized in this work. First, the choice of construction of the residual, R, is considered. In the construction of the residual the approximate angular flux, $\tilde{\psi}$, is operated on by the operator L. This could either be the DGFEM spatially discretized operator or the spatially continuous, Discrete Ordinates transport operator. In order to avoid the zero residual result due to Galerkin orthogonality, [15], the Discrete Ordinates operator, Eq. 3.4, is used.

With the operator in hand, the residual is constructed within each spatial cell and for each discrete ordinate in the angular quadrature. In order to comply with the DGFEM solver the distributed source must be isotropic and defined on a basis of Legendre polynomials. The projection of the residual onto the basis space is simple as both the angular flux and source are defined on it. In addition, the projection of the partial derivatives of the flux is simplified because derivatives of Legendre polynomials can be expressed as the sum of lower order Legendre polynomials, as given by: $\frac{dP_{n+1}(x)}{dx} = (2n+1)P_n(x) + (2(n-2)+1)P_{n-2}(x) + \ldots$. One must account for the fact that the basis functions are not in terms of the true spatial variables when determining their partial derivatives. The residual for a particular direction, R_n, is given by Eq. 6.5.

$$\begin{aligned} R_n(\bar{x},\bar{y}) = \Sigma_{i=0}^{\Lambda}\Sigma_{j=0}^{\Lambda}((S_{i,j} + \sigma_s\phi_{i,j} - \sigma_t\psi_{i,j}^{n})P_i(\bar{x})P_j(\bar{y}) \\ -\psi_{i,j}^{n}(\mu_n P_j(\bar{y})\frac{d\bar{x}}{dx}\frac{dP_i(\bar{x})}{d\bar{x}} + \eta_n P_i(\bar{x})\frac{d\bar{y}}{dy}\frac{dP_j(\bar{y})}{d\bar{y}})) \end{aligned} \tag{6.5}$$

Once the residual has been defined for each direction, it is integrated over angle, as given by (3.5), to obtain an approximate isotropic residual suitable for use by the DGFEM transport solver. The final modification necessary for implementation, was to enable the DGFEM solver to accept negative sources, which are not physically realistic for the original transport problem but not unexpected for the error problem. Even with the negative residual sources, the DGFEM solver was able to converge to a solution for the error distribution, E.

6.1.1 L_2 Residual Source Error

With the expression of E in terms of a truncated Legendre series in hand one may consider the formulation of the true error, e, to be evaluated against. The L_2 error is considered as it is the form common to several of the estimators considered in this work. Though computationally intensive, the L_2 error utilizes more of the available information as it is an integrated quantity. The true, e^{L_2}, and estimated,E^{L_2}, errors are given in Eq. 6.6 and Eq. 6.7 for a given cell,

$$e^{L_2} = ||\psi^{DGFEM} - \psi^{MMS}||_{L_2} \tag{6.6}$$

$$E^{L_2} = ||E||_{L_2} \tag{6.7}$$

where E is computed from Eq. 6.4. The L_2 norm in this case, defined using the angular flux and its full Legendre polynomial representation is given by Eq. 6.8. The factor $\bar{A}$ is the determinant of the Jacobian transformation between the problem space (x, y) and the local space of the basis $(\bar{x}, \bar{y})$.

$$||\psi||_{L_2} = \sqrt{\Sigma_{n=1}^{N} w(n) \int_{-1}^{1} d\bar{x} \int_{-1}^{1} d\bar{y} \bar{A} (\Sigma_{i=0}^{\Lambda} \Sigma_{j=0}^{\Lambda} \psi_{i,j}^{n} P_i(\bar{x}) P_j(\bar{y}))^2} \tag{6.8}$$

With the expressions for the true error and error estimator consider a representative case of these errors in Figure 6.1. From this figure one can tell that this estimator possesses qualities similar to the true error. First, the error distributions are very similar and the singular characteristic lines are where larger errors are present. Additionally, the two generally occupy the same scale of magnitude and share their maximum value. There are regions where the true error is smaller than the estimator but this conservative estimation is generally preferable to underestimation.

Figure 6.1: Le=R errors: Log_{10} scale of $C0$, $\sigma_t = 1$, $c = 0.1$ and $\Lambda = 2$. Left: estimator Right: true error.

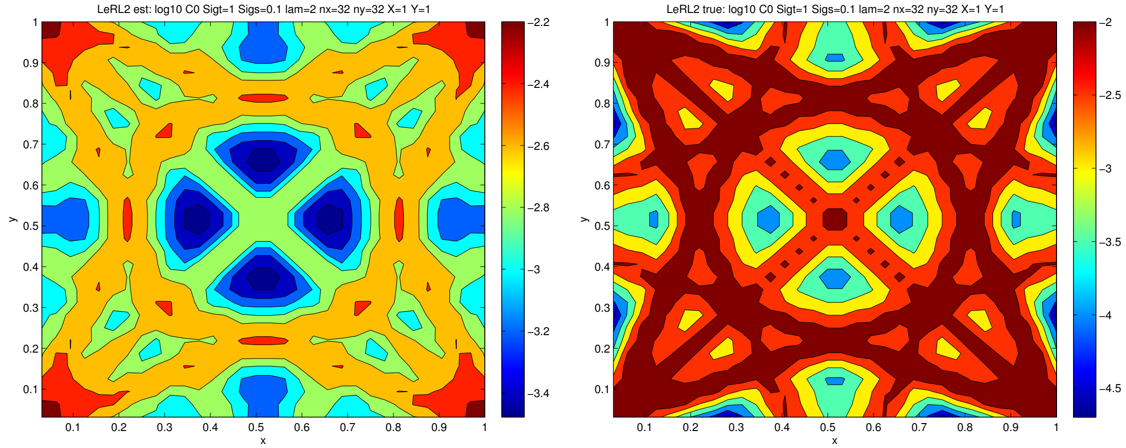

6.1.2 Estimator Validation

Now proceeding with a sampling of typical results from this estimator. First, consider the effectivity index in Figure 6.2. Overall, this is a good result with the effectivity being reasonably bounded. It is interesting that the region that is most underestimated is about the singular characteristics and may be due to forcing an isotropic residual source. It is also apparent that interior regions are closer to zero, the ideal effectivity on the log scale, than the boundary.

Figure 6.2: Le=R effectivity index: Log_{10} scale of $C0$, $\sigma_t = 1$, $c = 0.1$ and $\Lambda = 2$.

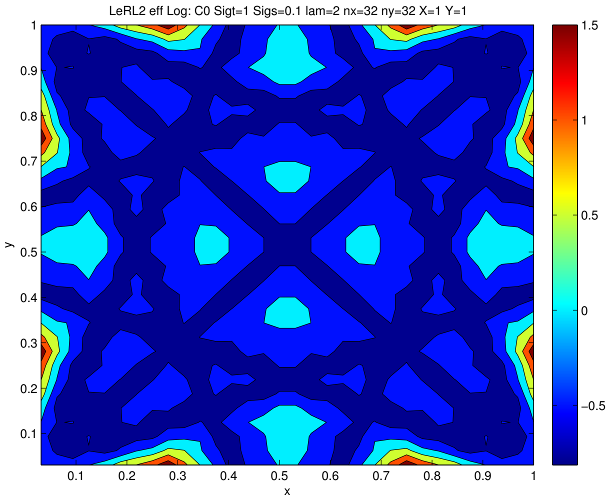

The spatial distribution of effectivity indexes is important but so is its overall performance. The set of effectivity index histograms in Figure 6.3 displays behavior typical of this estimator as one varies Λ. The resulting distribution for the $\Lambda = 0$ case uniformaily overestimates the error and its inability to estimate the magnitude of the error can be attributed to the poor residual approximation for this case. As the residual is taken locally over each element this case has no contribution from the streaming term as the partial derivatives of a constant flux are zero. Proceeding to the $\Lambda = 1$ case improvements are visible as there are several elements which have effectivity of one and the degree of overestimation is lessened. As can be seen in the teal bars this may be due to true error decreasing faster than the estimator. Finally, for $\Lambda = 2$

the distribution drops below $\theta = 1$. This can be attributed to the residual source drastically decreasing in magnitude, by as much as a factor of 10^{-5} from the $\Lambda = 0$ case. These small ”sources” may be insufficient to drive the solution of the error and the frequent change in sign may lead to cancellations as the error streams.

Figure 6.3: Le=R effectivity index: log scale for nx,ny=32 $\sigma_t = 1.0$, $C0$ and $c = 0.9$. Left: $\Lambda = 0$, Right: $\Lambda = 1$, Bottom: $\Lambda = 2$.

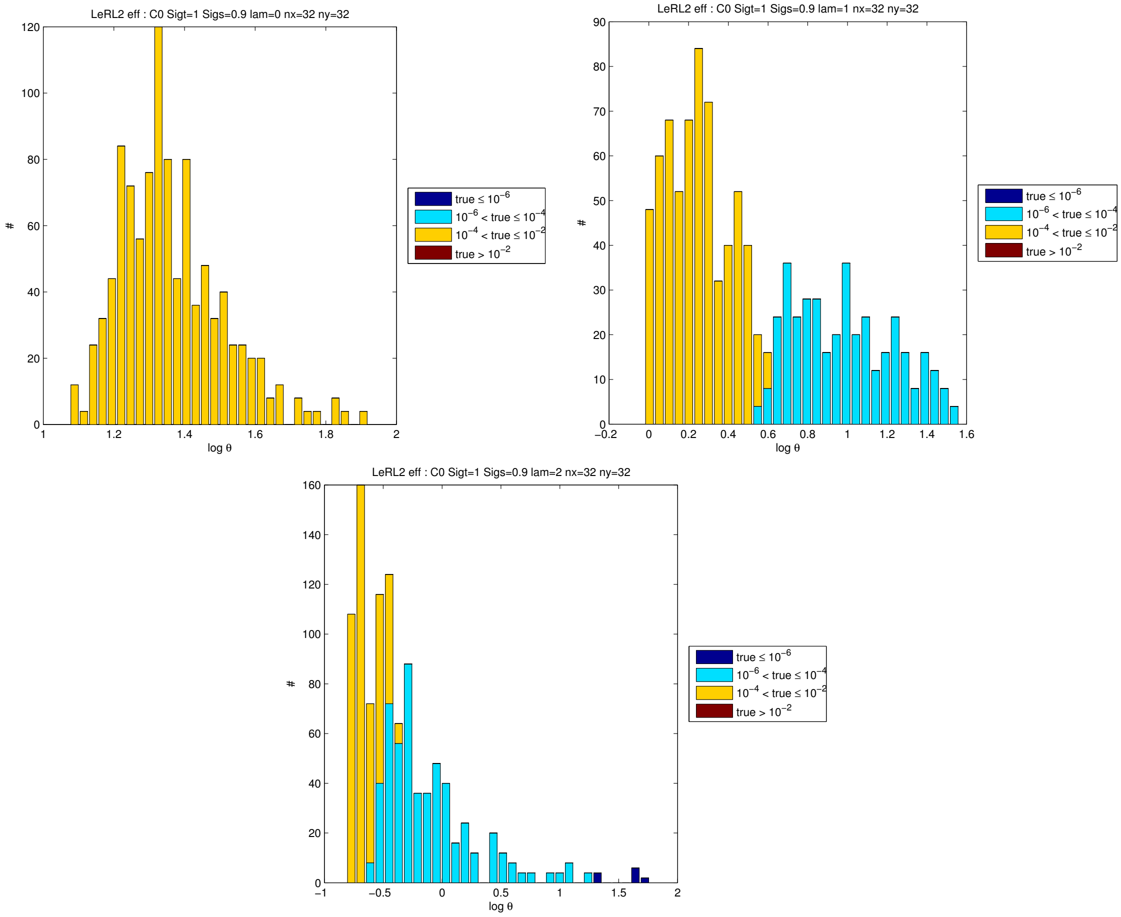

Even though the $\Lambda = 2$ case has a wide range and does not capture the magnitude of the error well it does a decent job in modeling the error distribution. Consider the normalized effectivity index in Figure 6.4. Note that the majority of the distribution is now about the ideal value of $\theta = 1$.

Figure 6.4: Le=R Normalized effectivity index: Log_{10} scale of $C0$, $\sigma_t = 1$, $c = 0.1$ and $\Lambda = 2$.

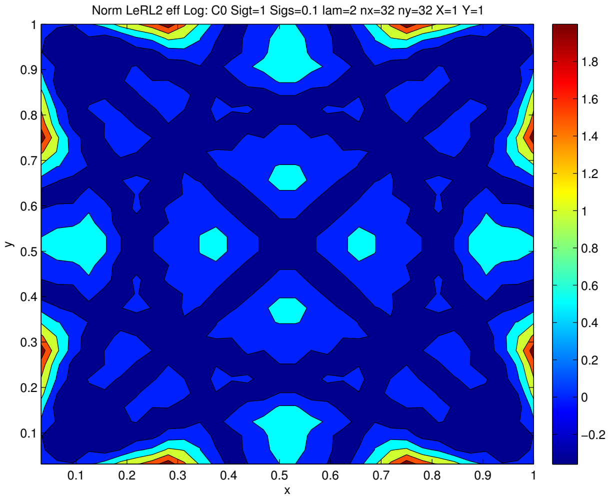

Unlike other estimators in this work the distributions with singular characteristic cells removed is unnecessary as these are the regions where this estimator behaves the best. This may be due to large contributions of local residual sources. These are also the regions where the true solution is largest and where error will always be present as even the true solution must attempt to fit discontinuities with continuous basis functions.

6.1.3 Conclusion

In conclusion, overall this is an effective estimator but may be prohibitively costly to run as it requires the formulation of the residual and requires the solving of an addition "transport" problem of the scale of the same size of the original problem whose solution error is to be estimated. However, this is an improvement when compared to the two mesh estimators. There are several interesting routes for further exploration with this estimator: utilizing an anisotropic residual source which may yield superior results and enforcing a non-zero residual source instead of sources of alternating signs that might cause source local cancellations that may suppress the magnitude of the error.

6.2 Madsen Estimator

In Madsen's article, [19], two error bounds are derived in the L_1 and L_2 norm of the error. In this work the L_2 error bound is considered. A set of constraints on the solution to $L\psi = S$ are applied. First the angular flux is absolutely continuous along characteristics, $\psi(\vec{r} + s\vec{\Omega}, \vec{\Omega})$. Additionally the absorption cross section is nonzero and greater than or equal to some parameter $\sigma_0 > 0$ everywhere in the domain and the scattering cross section is symmetric, $\sigma_s(\vec{\Omega}, \vec{\Omega}') = \sigma_s(\vec{\Omega}', \vec{\Omega})$. Now consider the inequality, based on neutron conservation, that is used to derive the error bound [19]:

$$||\psi||_{L_2} \leq \frac{1}{\sigma_0}||S||_{L_2} \tag{6.9}$$

Now define the error, e, to be $e = \psi - \tilde{\psi}$, where ψ is the true solution and $\tilde{\psi}$ is the approximate solution. Applying the transport operator to the error, $Le = L(\psi - \tilde{\psi}) = S - L\tilde{\psi}$. Now e is a solution of the transport equation and its source is the residual. Substituting the error and residual into equation (6.9), gives the desired error bound:

$$||e||_{L_2} \leq \frac{1}{\sigma_0}||S - L\tilde{\psi}||_{L_2} \tag{6.10}$$

Let this error bound be denoted by E^{Mad} for this work as (6.11). Additionally consider that this norm is determined in each spatial cell, that it is angle integrated and $\sigma_0 = \sigma_a$.

$$E^{Mad} = \frac{1}{\sigma_a}||S - L\tilde{\psi}||_{L_2} \tag{6.11}$$

An interesting way to perceive Madsen's estimator is to view it as Residual Source estimator in which the transport operator L has been approximated by σ_a, $L \approx \sigma_a$. This would occur only if the streaming operator were zero, $\vec{\Omega} \cdot \nabla\psi = 0$, and only in-scattering along each discrete ordinate. Obviously this would be a very uninteresting problem but would yield faster results than the Residual Source method if valid.

The computation of this estimator is straight forward. First, noting that S and $\tilde{\psi}$ are known quantities, the main concern is applying the transport operator L, in this case the discrete ordinates operator as opposed to the S_N DGFEM discretization of L. This choice has the benefit of treating space continuously and conforming to the angular discretization of the flux. The calculation consists of integrating sets of Legendre polynomials over the range $x, y \epsilon [-1, 1]$. Once again the orthogonality properties of the basis functions is exploited, including the partial derivative terms as they can be written in terms of lower order Legendre polynomials as given by the recursive relationship (6.12).

$$\frac{dP_{n+1}(x)}{dx} = (2n+1)P_n(x) + (2(n-2)+1)P_{n-2}(x) + (2(n-4)+1)P_{n-4}(x) + \dots \tag{6.12}$$

The true error that this estimator is compared to is the L_2 error, given by $e = ||\psi - \tilde{\psi}||_{L_2}$. Consider the initial comparison presented in Figure 6.5. The first observation is the shape of the distributions, they are quite similar. Both errors possess distinct SC lines but beyond the domain corners these regions cease to be the regions of largest error for the estimator. The two also disagree in their magnitudes. Madsen's estimator was derived as an upper bound and it does just that but by more than two orders of magnitude.

6.2.1 Estimator Validation

Even though this is not the primary analysis section of this work, it is useful to see the effectivity index of the quantities reported in Figure 6.5. The effectivity index for Madsen's estimator is plotted over the spatial domain in Figure 6.6. This figure is typical, Madsen's estimator overestimates the error. The effectivity values that are closest to zero, as this is log scale, are about the SC lines.

Figure 6.5: Madsen errors: Log_{10} scale of $C0$, $\sigma_t = 1$, $c = 0.9$ and $\Lambda = 1$. Left: estimator Right: true error.

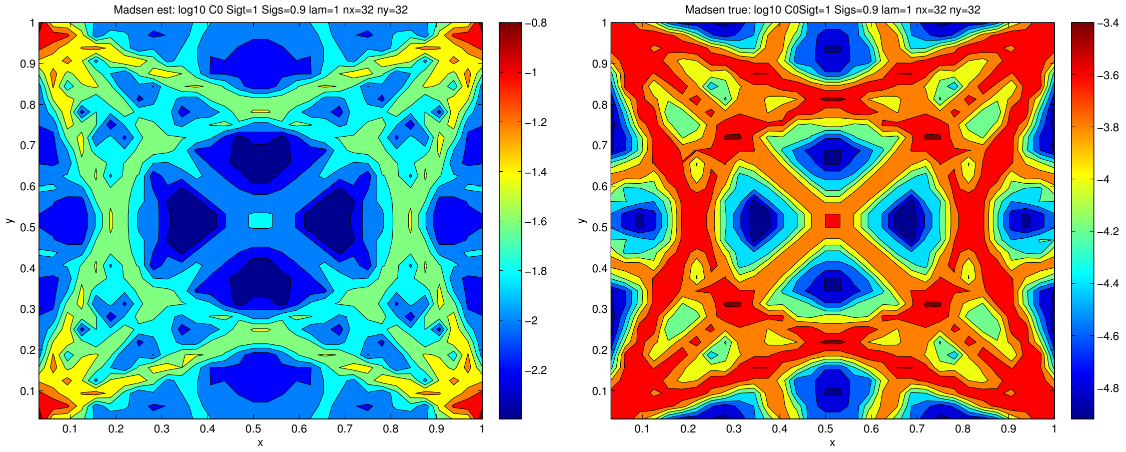

In all cases Madsen's estimator gratuitously over estimates the error. In addition this overestimation increases, in terms of the maximum value of θ and not its distribution, with increasing Λ, as seen in Figure 6.7. This is readily explained by examining the maximum and minimum values of the estimator and the true error in Figure 6.8, which is typical for all cross section cases. The effectivity index increases with increasing Λ because the true error decreases far more rapidly and to a greater extent than the estimator does. So in effect one is dividing a large number by a small one, which causes the effectivity index to grow in magnitude.

In an attempt to give Madsen's estimator its due. One can consider the effect of normalizing the true and estimated error to determine the normalized effectivity index. As seen in Figure 6.9, the effectivity index is at least on the order of the true error error. However, this benefit degrades as one increases Λ. Unlike the other error estimators, the removal of singular characteristic containing cells is not shown, as it leads to no substantial improvement in the results, such as narrowing the distribution. Conceivabley σ_0 could be chosen to more align the magnitudes of the true and estimated error but this does not aid in correcting for the difference in the distributions and there is no obvious guidance on how to determine such a σ_0 .

Figure 6.6: Madsen effectivity index: Log_{10} scale of $C0$, $\sigma_t = 1$, $c = 0.9$ and $\Lambda = 1$.

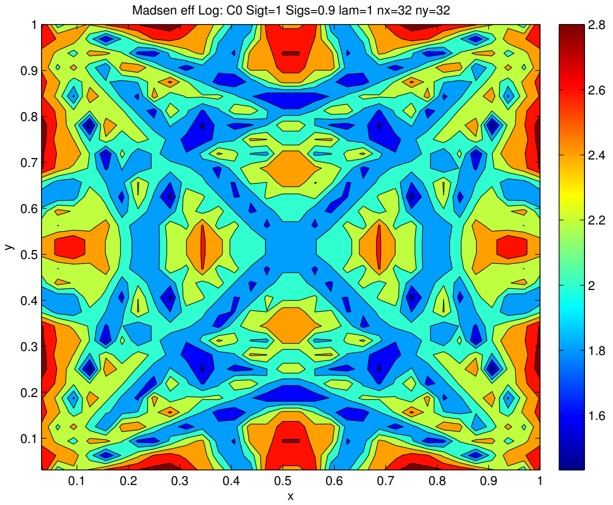

6.2.2 Conclusion

Overall, the Madsen error estimator behaves as a conservative upper bound on the error and not an actual estimator. It does a reasonable job in capturing the error distribution features, especially highlighting the increased error along the singular characteristics. This method does have the benefit of being computationally cheap as it relies only on the h-mesh angular flux solution whose error estimate is sought and not a more refined mesh solution nor a secondary solution.

Figure 6.7: Madsen effectivity index: log scale for nx,ny=32 $\sigma_t = 1.0$, $C0$ and $c = 0.1$. Left: $\Lambda = 0$, Right: $\Lambda = 1$, Bottom: $\Lambda = 2$.

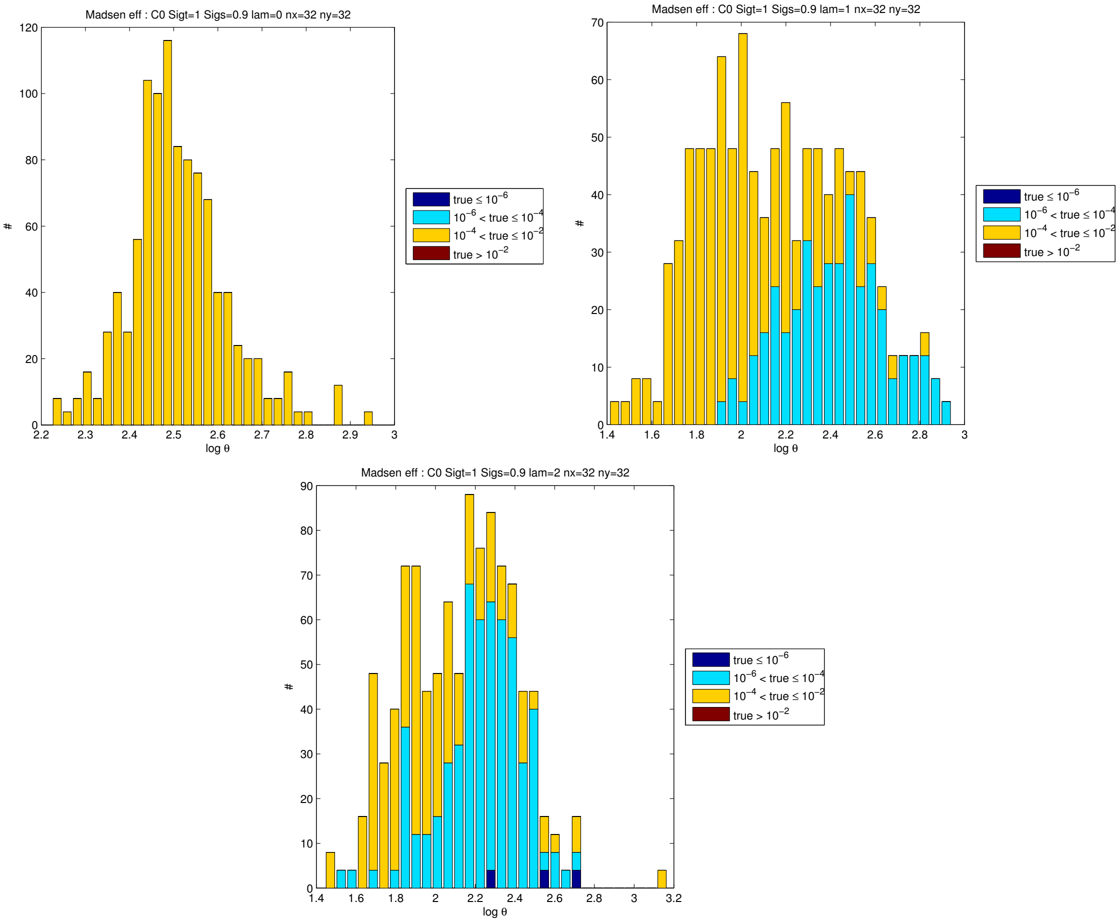

Figure 6.8: Madsen and True error min and max values: Log_{10} scale of $C1$, $\sigma_t = 1$, $c = 0.9$

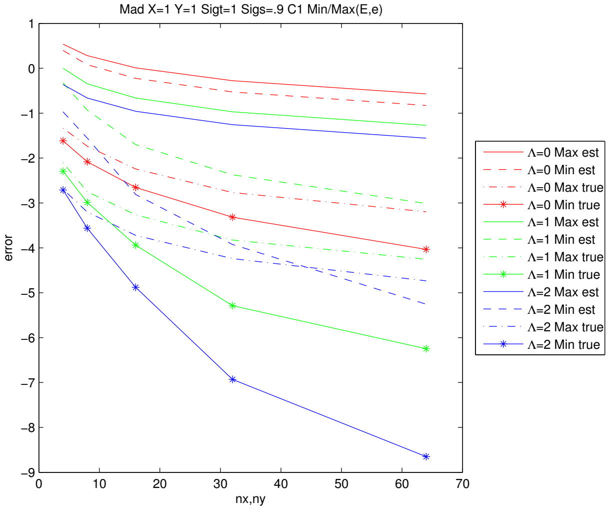

Figure 6.9: Madsen normalized effectivity index: log scale for nx,ny=32 $\sigma_t = 1.0$, $C0$ and $c = 0.1$. Left: $\Lambda = 0$, Right: $\Lambda = 1$, Bottom: $\Lambda = 2$.

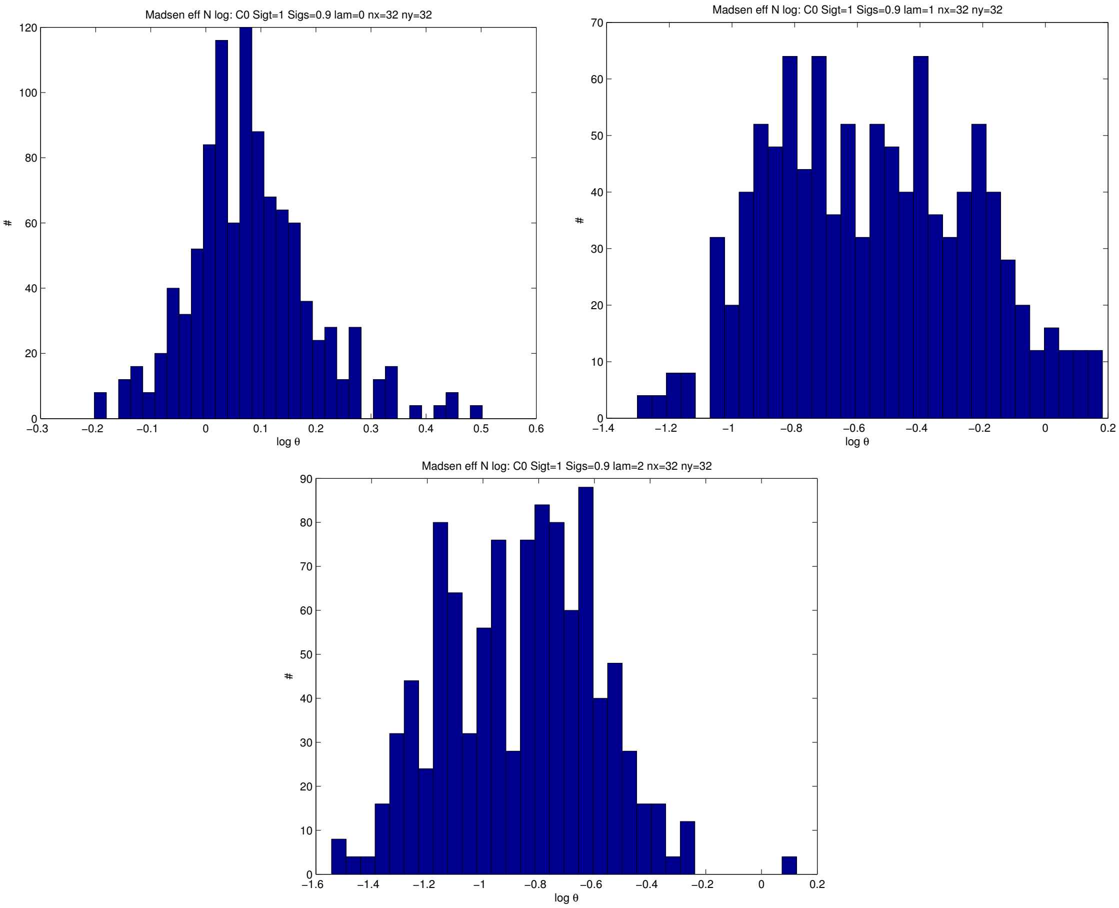

CHAPTER 7

Discontinuity Estimators

The final class of estimators examined in this work is based on the estimator proposed in [12] and is based on a DGFEM solution of the transport equation. Recalling that the solution is allowed to be discontinuous on cell boundaries, this estimator simply measures the discontinuity along the inflow boundaries. Given a spatial cell K, with a boundary ∂K, and considering the first angular quadrant, $\mu, \eta > 0$ (a similar definition applies to other quadrants), the estimator can be written as:

$$E = |\eta| \int_{\partial K_x} |\psi_K - \psi_{K,below}| dx + |\mu| \int_{\partial K_y} |\psi_K - \psi_{K,left}| dy \tag{7.1}$$

This estimator is based on an assumption of continuity of true flux across cell boundaries. This continuity is generally true along characteristics but can fail when crossing singular characteristics. In these calculations the differences in continuity are taken only along characteristics and not across them. However, these discontinuities can cut through elements and must be modeled by continuous basis function over the element. Much like the residual based estimators there is no exact correlation between residual and the error and there is no exact relation between flux continuity and the error in the flux. For both cases there is the expectation that smaller differences are signs of lesser errors.

7.1 Angular Flux Estimator

The angular flux form of this class of estimator is inspired by Eq. 7.1. In order to bring it into line with the majority of estimators in this work this estimator is formulated in an L_2 sense. The estimated error is given by Eq. 7.2 and the true error by Eq. 7.3. Where $\bar{K}$ is a cell sharing a boundary with K and dS is either dx or dy, depending on whether the edge is horizontal or vertical, respectively. When a cell shares an inflow edge with the problem boundary the known boundary conditions of the flux are used. If it is an outflow boundary, that portion is set to zero. The contributions for each direction are then summed to yield a single value per element.

$$E^{J\psi} = \sqrt{\Sigma_{n=1}^{N} w_n \int_{\partial K} dS(\psi_{n,K} - \psi_{n,\bar{K}})^2} \tag{7.2}$$

$$e^{J\psi} = \sqrt{\Sigma_{n=1}^{N} w_n \int_{\partial K} dS(\psi_{n,K}^{MMS} - \psi_{n,\bar{K}}^{MMS})^2} \tag{7.3}$$

The initial comparison of the true and estimated errors as seen in Figure 7.1 is generally good. The two share similar magnitudes with the estimator having a larger minimum than the true error which is generally a sign of the preferred conservative overestimation. The shape of the error distributions are similar enough. Both share the distinct singular characteristics and the difference in magnitude between the top/bottom and right/left boundary is observed in both and can be attributed to the nonzero boundary conditions on the left and right.

Now comparing the true and estimated errors via the effectivity index in Figure 7.2 shows that there are significant areas of disagreement. Namely, the significant overestimation of the error among cells neighboring singular characteristic lines. By referring to the estimated and true error in Figure 7.1 one observes that the estimated error along the singular characteristics

Figure 7.1: Jump Discontinuity ψ errors: Log_{10} scale of $C0$, $\sigma_t = 1$, $c = 0.1$ and $\Lambda = 1$. Left: estimator Right: true error.

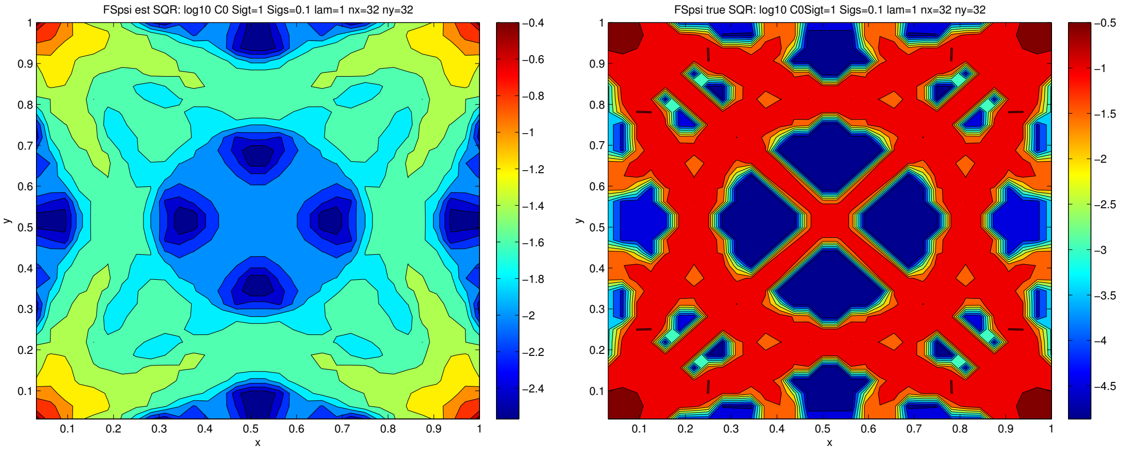

FSpsi est SQR: log10 C0 Sigt=1 Sigs=0.1 lam=1 nx=32 ny=32

FSpsi true SQR: log10 C0Sigt=1 Sigs=0.1 lam=1 nx=32 ny=32

is broader and does not drop off as rapidly with increasing distance from the SC as does the true error. This may be due to the contamination of the scattering sources of cells neighboring the singular characteristics by propogation of the inacuracies incured in the SC cell's own scattering source and contributing to larger errors in the DGFEM solution.

7.1.1 Estimator Validation

The results of the effectivity index with increasing Λ are disappointing in Figure 7.3, as the range of the index spread increases with Λ. In all cases there is a two peaked behavior and this estimator possesses a unique void about the ideal value of the effectivity index. It is apparent that the superior case is $\Lambda = 0$ due to its tighter range of effectivities. As the continuity between any element is improbable, unless the solution is flat, because each element is described by a single constant in both the MMS and DGFEM solutions, ensuring a significant difference is measured. This can be seen by the large values of the true error being larger than 10^{-2} (maroon). By increasing the basis space the ability to have continuities across cells increases and the inter cell differences should decrease. This is observed by the true error rapidly decreasing as Λ increases and by $\Lambda = 2$ (recall that this is a surface of order x^2y^2) the bulk of the true error

Figure 7.2: Angular Jump Discontinuity Effectivity Index: Log_{10} scale of $C0$, $\sigma_t = 1$, $c = 0.1$ and $\Lambda = 1$

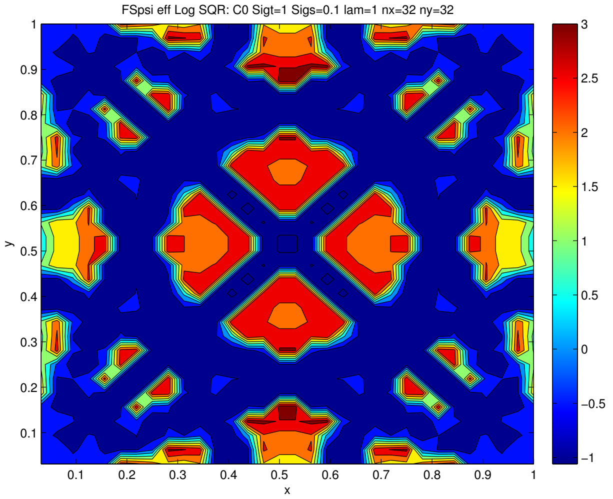

is less than 10^{-6} (blue). The estimated error simply cannot keep up with the rapidly decreasing true error.

The effect of removing the SC lines in Figure 7.4 is most prominent in the $\Lambda = 0$ case where the majority of removed elements are below the ideal value of $\theta = 1$. These are the elements where the estimated error is smaller than the true error and referring again to the spatial effectivity index in Figure 7.2 are those that lie along the singular characteristic. The effect on the higher values of Λ appears to be less significant. In all cases there is a general removal across all values of θ. Recalling the idea of singular characteristics contaminating neighboring elements in the estimated error, one may expect that if these neighboring/contaminated elements were removed along with the singular characteristic ones there ought to be an even greater improvement by removal of large effectivities.

The effect of normalizing the effectivity index in Figure 7.5, is insignificant for all Λ, with only a slight shift to the right in the distribution. This results does show that the true and estimated error are similar in magnitude as was noted in the maximum values in Figure 7.1 upon which the normalization is based but that the distributions do not coincide. Another potential for the exploration of this estimators is to instead normalize the error distributions to

Figure 7.3: Angular Jump Discontinuity effectivity index: log scale for nx,ny=32 $\sigma_t = 1.0$, $C0$ and $c = 0.1$. Left: $\Lambda = 0$, Right: $\Lambda = 1$, Bottom: $\Lambda = 2$.

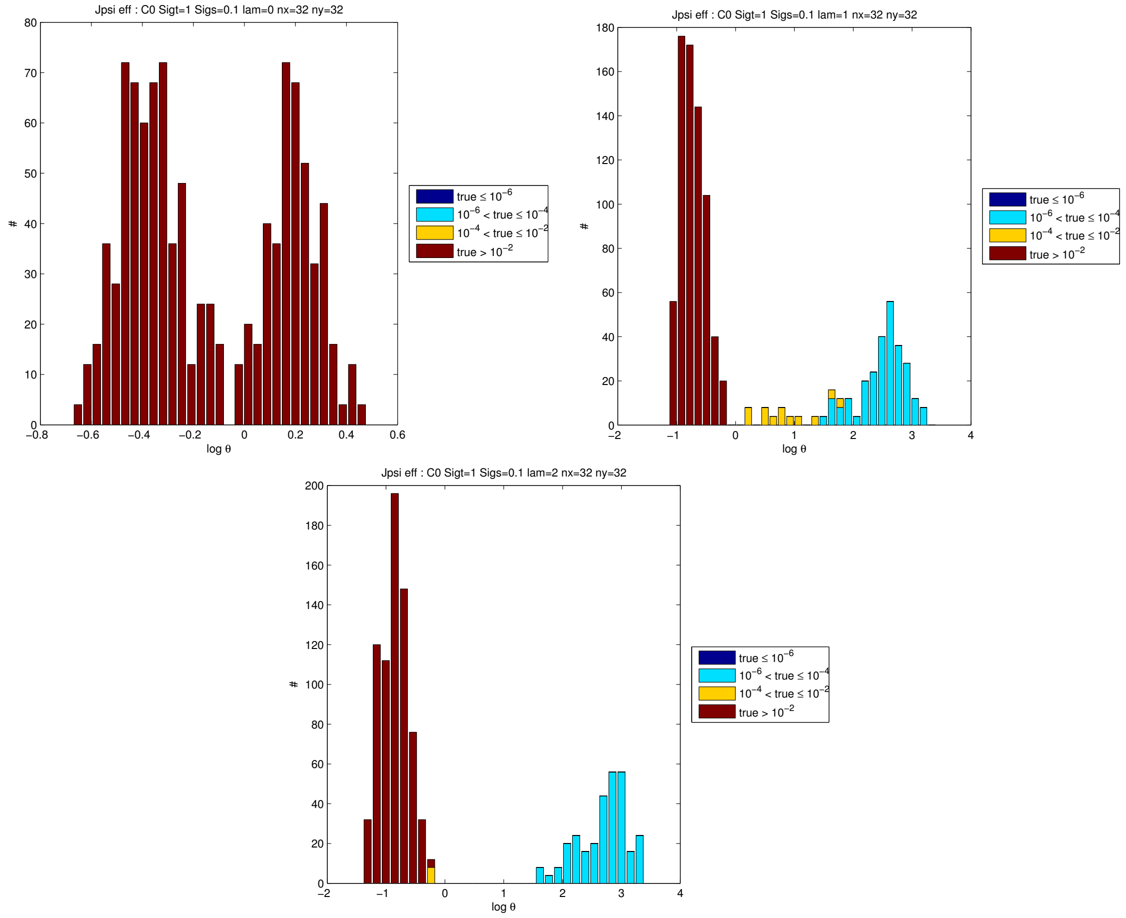

their integrated "volume" instead of their maximum values.

This is one estimator upon which the results are strongly coupled to the degree of true solution continuity across the singular characteristic. When moving from $C0$ to $C1$ regular configurations and comparing low and high scattering ration cases in Figure 7.6 it is clear that the $C1$ case is a significant improvement over $C0$ in Figure 7.3 when comparing the largest values of the effectivity index. In addition the difference between the two scattering cases is small because the model problem's manufactured solution is not explicitly dependent on the scattering cross section and is instead dependent on the auxilary source, Q, which is the same in both scattering cases (recall Eq. 3.13). Therefore, this estimator's effectiveness is clearly coupled

Figure 7.4: Angular Jump Discontinuity effectivity index with removed SC cells: log scale for nx,ny=32 $\sigma_t = 1.0$, $C0$ and $c = 0.1$. Left: $\Lambda = 0$, Right: $\Lambda = 1$, Bottom: $\Lambda = 2$.

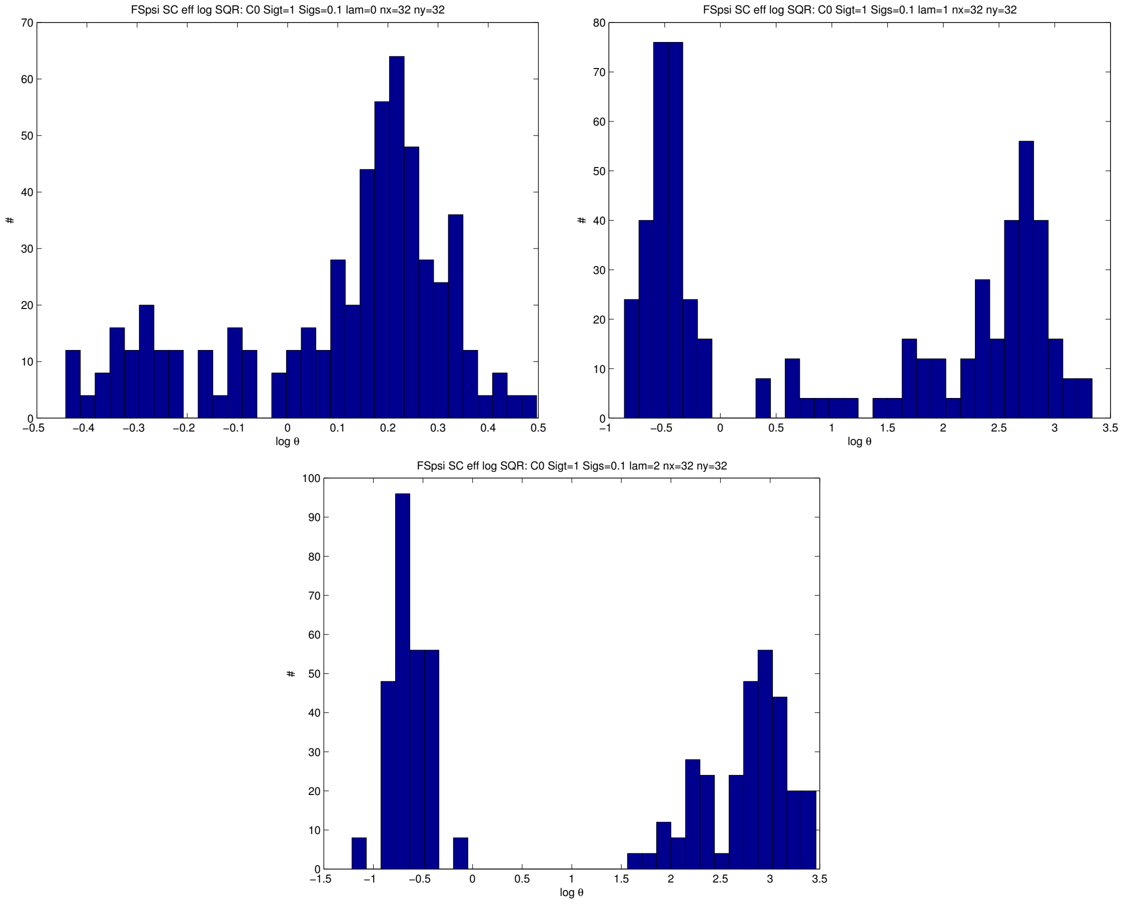

to continuity of the true solution which makes sense due to its formulation and the formulation of the test problems.

7.1.2 Conclusion

The angular flux discontinuity estimator yielded acceptable results for the $\Lambda = 0$ case and it proved superior to the greater Λ expansion orders as the discontinuity cannot decrease as rapidly ensuring a meaningful difference to measure. There is also a strong dependence on the continuity of solution, with performance improving from $C0$ to $C1$. One would expect further improvements for greater orders of continuity, such as $C2$ but these are cases not observable in

Figure 7.5: Angular Jump Discontinuity normalized effectivity index: log scale for nx,ny=32 $\sigma_t = 1.0$, $C0$ and $c = 0.1$. Left: $\Lambda = 0$, Right: $\Lambda = 1$, Bottom: $\Lambda = 2$.

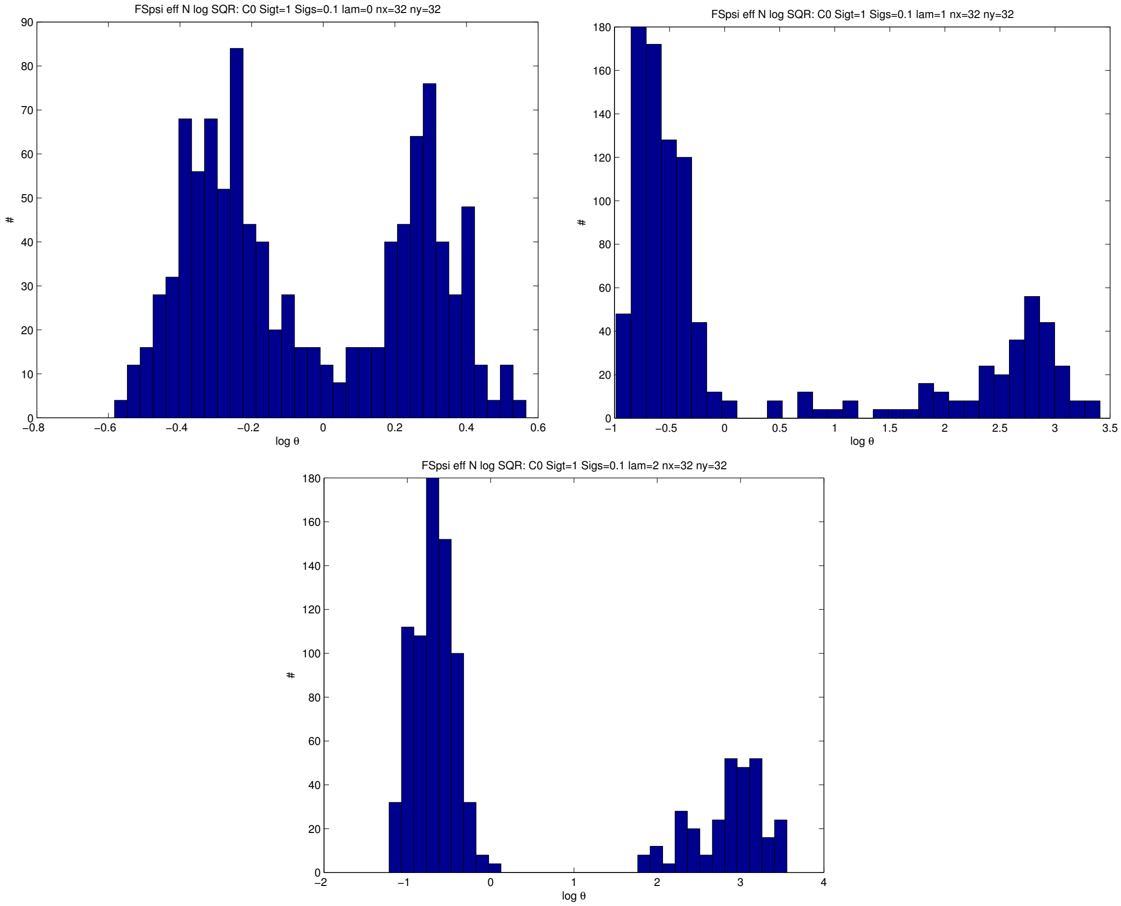

realistic configurations.

7.2 Scalar Flux Estimator

As the angular flux is not stored it is interesting to consider discontinuity effects as measured from the scalar flux. It is defined in a similar manner to the angular flux form with the estimator given by Eq. 7.4 and the true error by Eq. 7.5. Again all boundaries must be considered but there are no boundary conditions for the scalar flux in transport formulation. To account for this edges that compose the problem boundary have differences that are artificially set to zero.

Figure 7.6: Jump Discontinuity ψ errors: Log_{10} scale of $\sigma_t = 1$, $C1$ and $\Lambda = 1$. Left: $c = 0.1$ Right: $c = 0.9$.

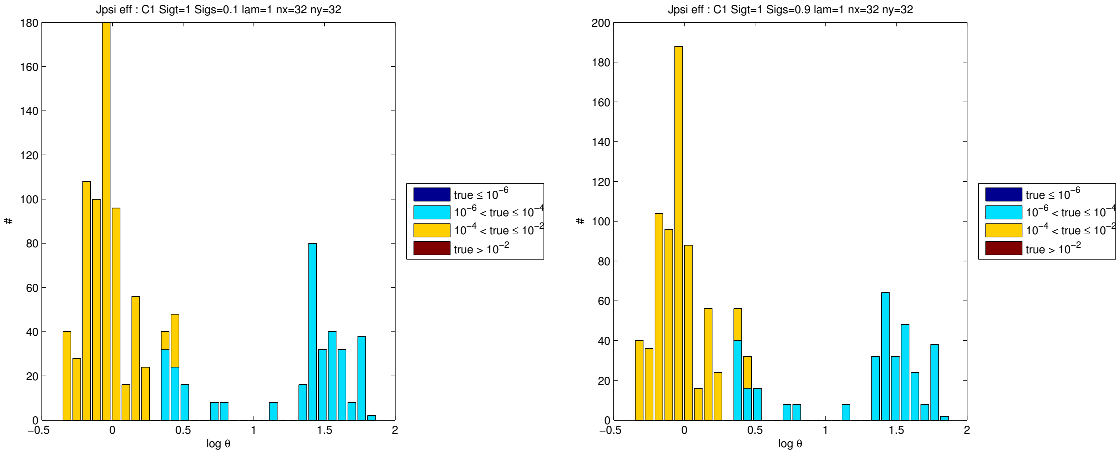

$$E^{J\phi} = \sqrt{\int_{\partial K} dS(\phi_K - \phi_{\bar{K}})^2} \tag{7.4}$$

$$e^{J\phi} = \sqrt{\int_{\partial K} dS(\phi_K^{MMS} - \phi_{\bar{K}}^{MMS})^2} \tag{7.5}$$

The results discovered are naturally similar to the angular flux formulation and similar conclusions may be drawn. This can be seen when comparing the scalar flux form of the discontinuity error shown in Figure 7.7 to the angular flux version shown in Figure 7.1. Instead of repeating the above arguments verbatim it is sufficient to consider them observing the following figures.

7.2.1 Estimator Validation

The results for the scalar flux form are very similar to the angular flux results. In Figure 7.9, the effectivity index, the same two peak behavior is observed. By normalizing the distribution in Figure 7.10 the distribution is shifted slightly to the right, a slight improvement, and there are actually discernible peaks about the ideal of zero (in the log sense), unlike the angular flux

Figure 7.7: Jump Discontinuity ϕ errors: Log_{10} scale of $C0$, $\sigma_t = 1$, $c = 0.1$ and $\Lambda = 1$. Left: estimator Right: true error.

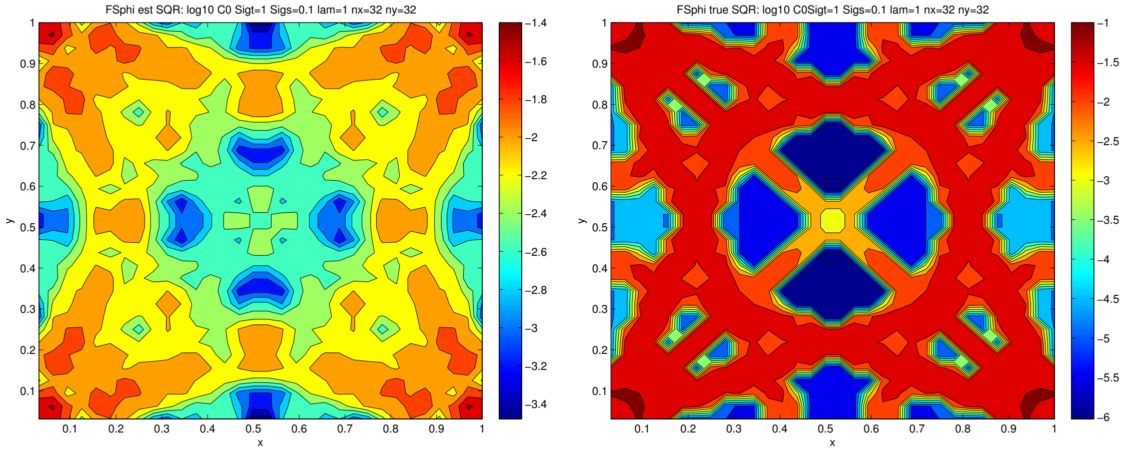

version of this estimator.

There is some benefit observed by removing cells intersected by the SC lines in Figure 7.11, in all cases of Λ and in particular $\Lambda = 0$, the majority of the values of the effectivity index removed are of $\theta < 1$. Comparing the true and estimated error in Figure 7.7, there is better agreement between the location of the maximum error, along the SC, than in the angular case.

7.2.2 Conclusion

The scalar flux discontinuity estimator performs similarly to the angular flux version. It possesses a distribution that better resembles the true distribution as seen by the normalized effectivity index. As one would expect the same behavior occurs with increasing Λ as in the angular flux form. Given that the two forms have such similar results it is clear that the scalar flux version may be preferable in that is simply faster to compute by approximately a factor of N, the number of discrete directions. Also, most transport codes print out the scalar flux at the conclusion of execution, but not the angular flux. Hence the scalr flux estimator can be evaluated without altering an existing code, while the angular flux discontinuity estimator is likely to require some modification or postprocessing of the code's output.

Figure 7.8: Scalar Jump Discontinuity Effectivity Index: Log_{10} scale of $C0$, $\sigma_t = 1$, $c = 0.1$ and $\Lambda = 1$

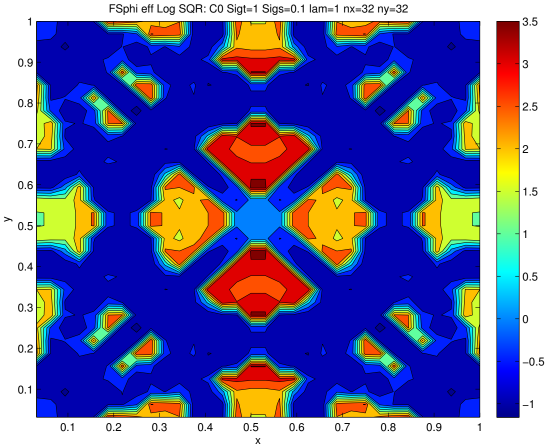
FSphi eff Log SQR: C0 Sigt=1 Sigs=0.1 lam=1 nx=32 ny=32

Figure 7.9: Scalar Jump Discontinuity effectivity index: log scale for nx,ny=32 $\sigma_t = 1.0$, $C0$ and $c = 0.1$. Left: $\Lambda = 0$, Right: $\Lambda = 1$, Bottom: $\Lambda = 2$.

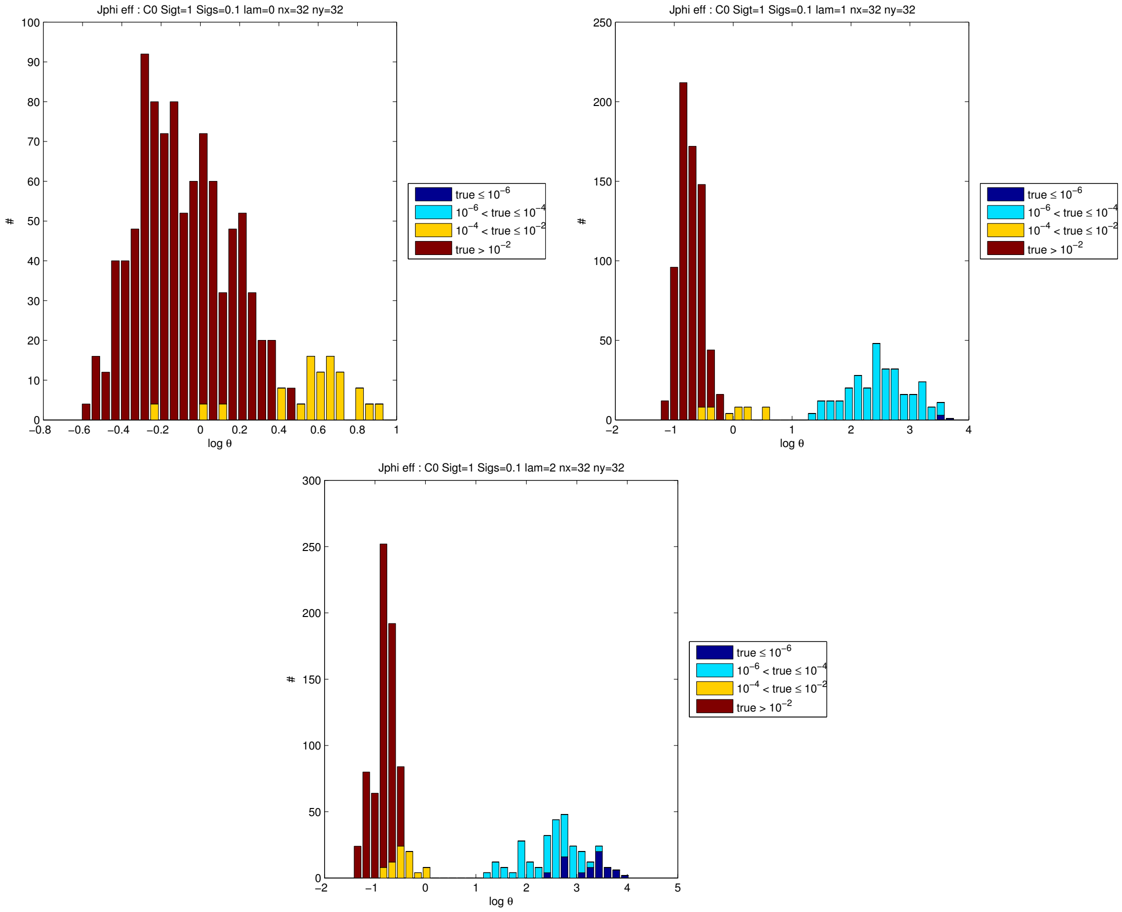
Jphi eff : C0 Sigt=1 Sigs=0.1 lam=0 nx=32 ny=32

Jphi eff : C0 Sigt=1 Sigs=0.1 lam=1 nx=32 ny=32

Jphi eff : C0 Sigt=1 Sigs=0.1 lam=2 nx=32 ny=32

Figure 7.10: Scalar Jump Discontinuity normalized effectivity index: log scale for nx,ny=32 $\sigma_t = 1.0$, $C0$ and $c = 0.1$. Left: $\Lambda = 0$, Right: $\Lambda = 1$, Bottom: $\Lambda = 2$.

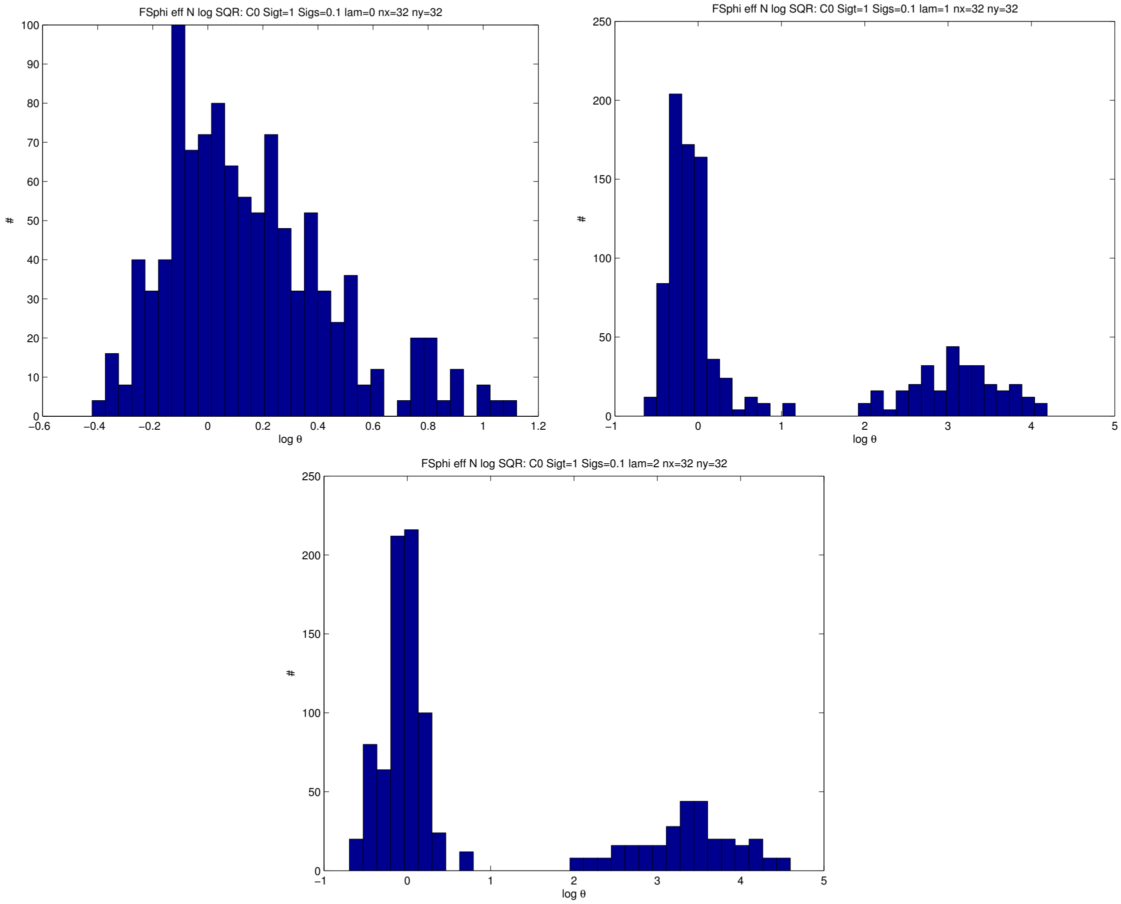

Figure 7.11: Scalar Jump Discontinuity effectivity index with removed SC cells: log scale for nx,ny=32 $\sigma_t = 1.0$, $C0$ and $c = 0.1$. Left: $\Lambda = 0$, Right: $\Lambda = 1$, Bottom: $\Lambda = 2$.

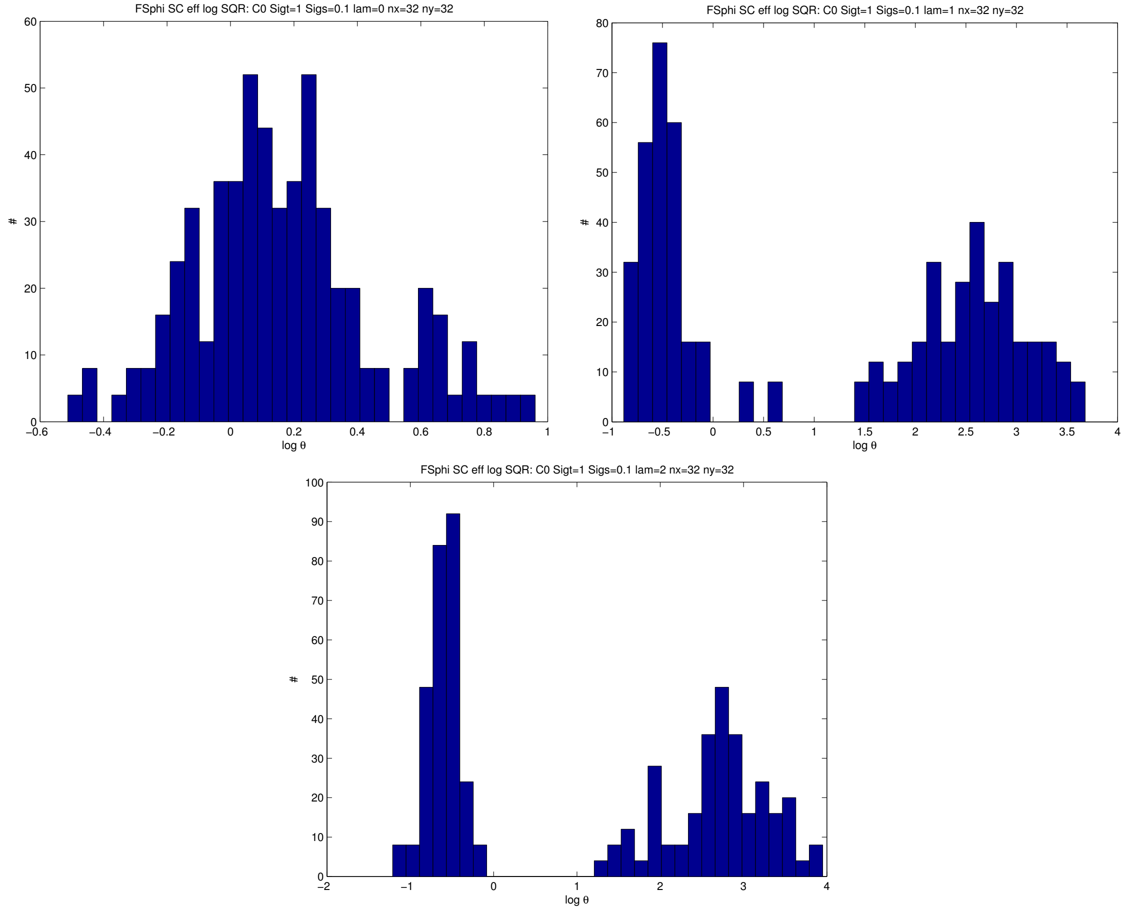

CHAPTER 8

Estimator Comparison and Conclusion

8.1 Introduction

The previous chapters served to introduce the set of error estimators and detailed some general features of their behavior by examining a small sample of test cases. As it is impractical to consider each of the 240 test cases (mesh, continuity, basis, scattering, etc) for each estimator. The remainder of the discussion is relegated to observing and contrasting global properties of the estimators under consideration such as total error and average effectivities of all the estimators over a larger set of test cases.

8.2 Global L_2 Error and Average Effectivity Indexes

A natural first test of the estimators is whether they behave as the true error in the global L_2 error norm. By starting the discussion in a global sense, some general qualities of the estimators may be explored. For all cases the global error is given by Eq. 8.1, for both the true and estimated error where $e_{i,j}$ is the error in element (i, j).

$$e_{global} = \sqrt{\Sigma_{i=1}^{nx}\Sigma_{j=1}^{ny}e_{i,j}^2} \quad (8.1)$$

The average of the effectivity index, Eq. 4.2 and stated again as $\bar{\theta} = \frac{1}{nx \times ny}\Sigma_{i=1}^{nx}\Sigma_{j=1}^{ny}\theta_{i,j}$, is a useful metric for the error estimators. However, caution must be exercised, as a single large value (outliers) of the effectivity index may overwhelm the contribution of many ideal values of unity. Even with this warning, the fact is that it provides a convenient global indicator of an estimator's behavior. Additionally, notice in the following figures that quantities with cells traversed by the SC lines removed from the tallying begin at $nx, ny = 16$ because meshes coarser than this contain a SC line in every cell.

8.2.1 Cell Centered Two Mesh Estimator

The two mesh cell centered error behaves in an interesting manner as seen as Figure 8.1. Overall the true and estimated errors have similar forms and are of similar magnitude. It is also apparent that the errors seem to plateau, particularly in the $C1$ case. This lack of the constant decreasing of the errors with mesh refinement, as seen in other estimators, is due to the lack of dx, dy terms by construction. The error in each cell, on average, must be decreasing as the number of cells increases in order to remain nearly constant. This is the case for this estimator, even in the L_2 norm, because of Eq. 8.1 which does not incorporate an additional dA term which is present in all other estimators under consideration.

The cell centered two mesh estimator average effectivity index depicted in Figure 8.2 (a note on the legend for averaged values of θ: θ is the usual effectivity index, SC θ is the effectivity index SC containing cells removed from binning and N θ is the normalized effectivity index), shows general growth, with mesh refinement, of the average θ and is particularly pronounced in the $\Lambda = 2$ case. This is due to the true error becoming exceptionally small because as the mesh is refined and Λ increases the true error becomes exceptionally small.

Figure 8.1: Two Mesh error: for $\sigma_t = 1.0$ and $c = 0.9$. Left: $C0$ Right: $C1$.

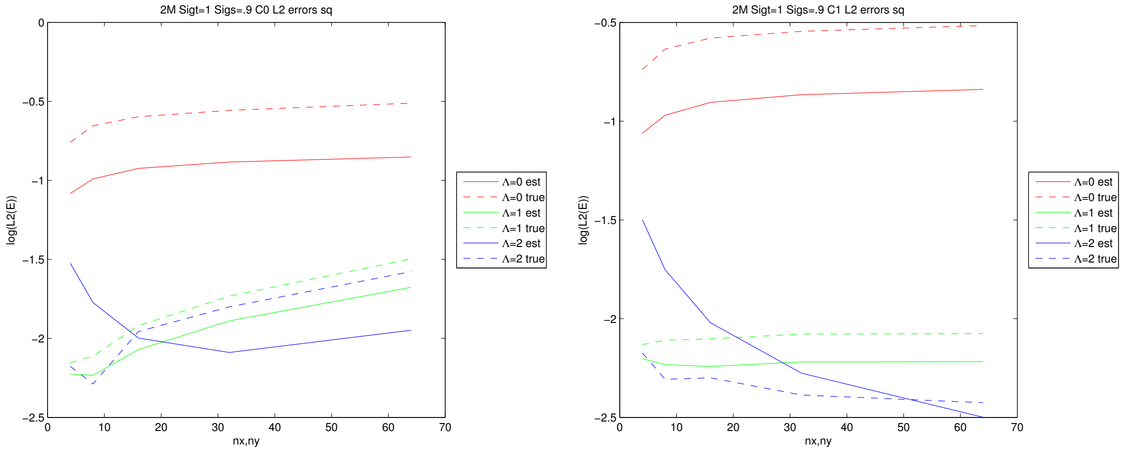

8.2.2 Ragusa and Wang Estimator

Consider Figure 8.3, which is characteristic of the other test cases of the Ragusa and Wang estimator. In general the estimator and the true error follow the same trend as the mesh is refined. However, a major drawback is that the estimated error is less than the true error. This serves to show the Ragusa and Wang estimator does not bound the error from above even in the L_2 norm and in both cases underestimates it. In terms of Λ, the error decreases as Λ increases, which is as one would expect. An interesting difference between the $C0$ and $C1$ cases occurs with regard to the continuity across the singular characteristic. In all of the cases explored the error is smaller in $C1$ (except for the coarsest mesh), this is again expected as a continuous basis space is used.

Beginning with the Ragusa and Wang estimator with its average effectivity index in Figure 8.4. The most striking feature is the uniqueness of the $\Lambda = 0$ case compared to the higher expansion orders. In all cases, it mostly overestimates the error. Even though overestimation is preferable to underestimating the error, its behavior is clearly more volatile than the others. This is particularly noticeable in the $C1$, $c = .1$ case, in which the SC removed line is constantly increasing. The $\Lambda > 0$ cases are far less wild but they consistently underestimate the error. Also notice that in the $C1$ and $\Lambda > 0$ cases the normalized effectivity index is about $\theta = 1$, on a linear

Figure 8.2: Two Mesh Average Effectivity Index: Top Left $C0$ $c = .1$ Top Right $C0$ $c = .9$ Bottom Left $C1$ $c = .1$ Bottom Right $C1$ $c = .9$. Legend: θ is the usually effectivity index, SC θ is the effectivity index SC containing cells removed from binning and N θ is the normalized effectivity index

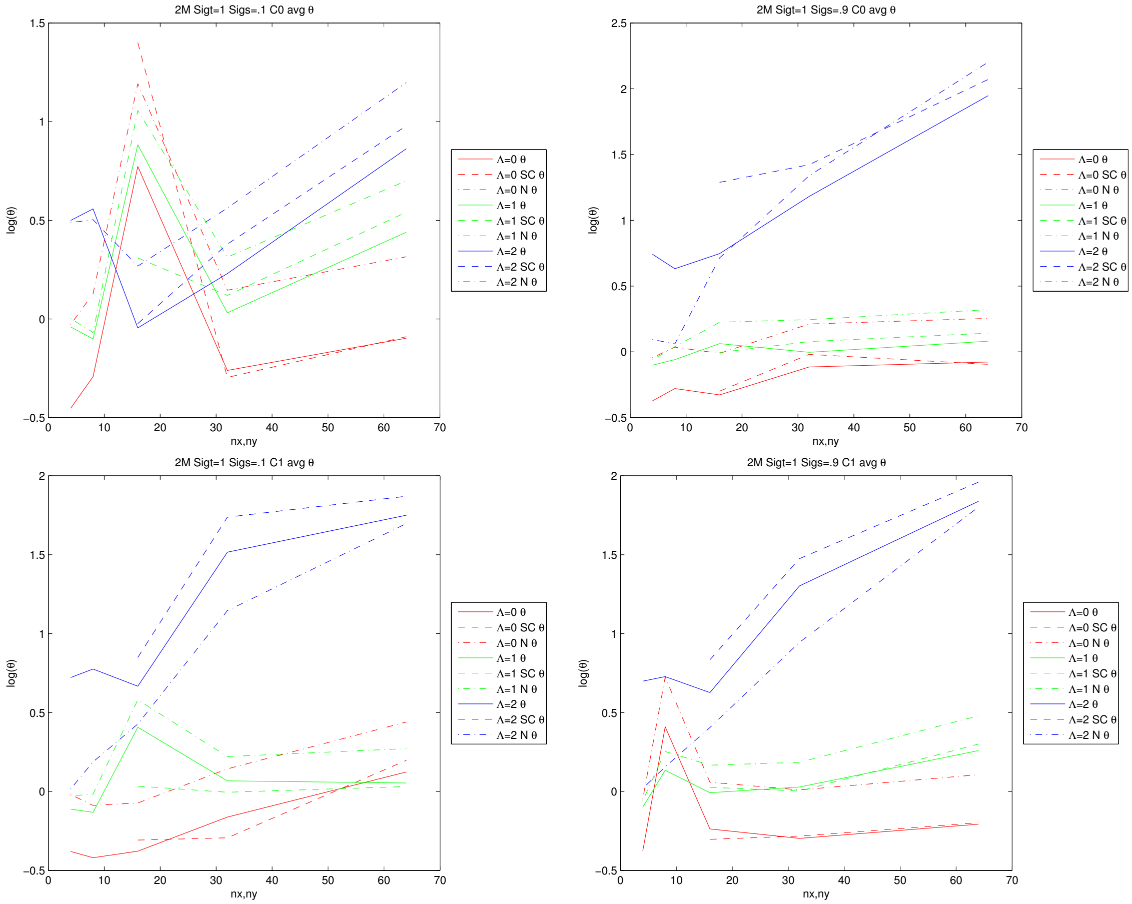

scale, this is evidence that while this estimator may underestimate the error it approximates the true error distribution well. This feature is likely why the authors in [20] and [21], utilized it to drive an adaptive mesh refinement algorithm.

8.2.3 Residual Source Estimator

The Residual Source estimator does a reasonable job of estimating the true global L_2 error norm as observed in Figure 8.5. The $\Lambda = 0$ exhibits the worst performance because of the zero valued

Figure 8.3: Ragusa and Wang $L2$ error: for $\sigma_t = 1.0$ and $c = 0.9$. Left: $C0$ Right: $C1$.

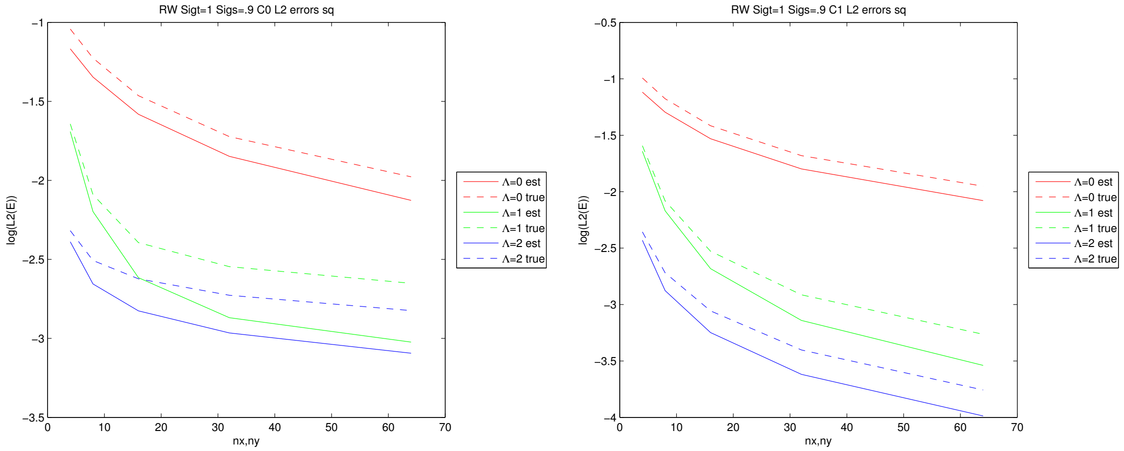

partial derivative terms in the residual. This effectively leaves the operator as a constant $L = \sigma_t$, which explains the constant estimator error. For the $\Lambda > 0$ cases the results are much improved. The estimator bounds the true error from above for $\Lambda = 0$ and $\Lambda = 1$, but it underestimates the true error for $\Lambda = 2$ and generally, except for $\Lambda = 0$ the true and estimated errors trend together.

As with many estimators in this work the average effectivity index, Figure 8.6, tends to increase as the mesh is refined and is due to the true error becoming exceptionally small. The same effect occurs with the normalized and removed singular characteristics effectivities because the ideal values of θ lie on and about these lines. As one refines the mesh a small region of growing effectivities clearly overwhelm these beneficial regions.

8.2.4 Madsen Estimator

In this scenario the Madsen estimator performs horribly as seen in Figure 8.7. The estimator significantly over estimates the true error but for cases of $\Lambda > 0$ the estimated and true error follow similar trends for the $C1$ case. While it is constructed as a conservative upper bound on the error this is too large, often by a factor of 10^2, to be useful.

The Madsen estimator as usual overestimates the true error. However, the normalized

Figure 8.4: Ragusa and Wang Average Effectivity Index: Top Left $C0$ $c = .1$ Top Right $C0$ $c = .9$ Bottom Left $C1$ $c = .1$ Bottom Right $C1$ $c = .9$

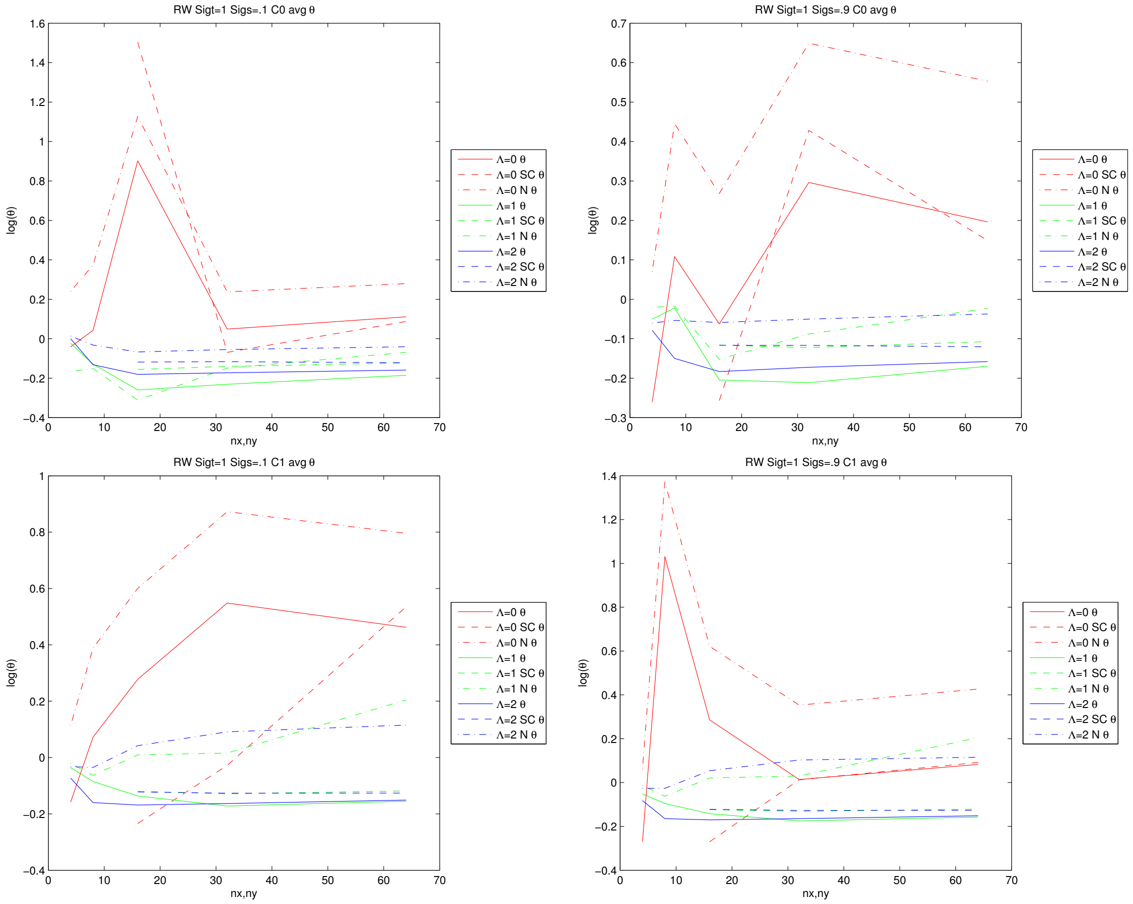

average effectivity index in Figure 8.8, there is a sign of agreement, indicating that the true and estimated error distributions generally agree.

8.2.5 Discontinuity Estimators

Finally consider the angular, Figure 8.9, and scalar, Figure 8.10, flux forms of the jump discontinuity error estimators. Once again, the true and estimated errors are of the same order of magnitude and follow similar distributions. As often occurs throughout this work, the $C0$ cases are not as well behaved as $C1$. This can be seen in the both ϕ and ψ discontinuity estimators, with the errors plateauing and overlaping with the errors of other orders of Λ. As observed

Figure 8.5: Residual Source $L2$ error: for $\sigma_t = 1.0$ and $c = 0.9$. Left: $C0$ Right: $C1$.

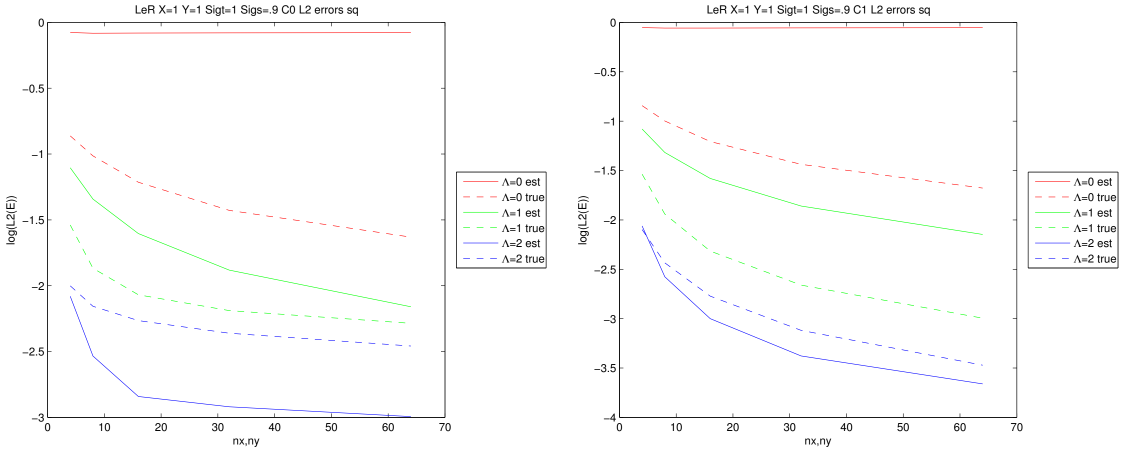

in the individual case plots (e.g. Figure 7.9) of effectivity indexes, the $\Lambda = 0$ case is the best behaved, even though there is underestimation, the errors are markedly closer than the higher order Λ.

The behavior of the flux discontinuity estimator average effectivity index of the angular flux, Figure 8.11, and scalar flux, Figure 8.12 indicates that, once again, the error estimator significantly over estimates the error and is chiefly due to the true error becoming exceptionally small as noted in the chapter discussion, where the error is predominately below 10^{-6}. This is due to the MMS solution being able to capture the continuity that exists away from SCs. In the DGFEM solution there is no continuity requirement. This conclusion is supported by the behavior of the $\Lambda = 0$ case in which the MMS loses its advantage of capturing the continuity and like the DGFEM case it can only embody the cell average value.

8.3 Computational Time

The final global quantity considered is the computational time of the estimator, in Figure 8.13. Here there is no distinction between continuity or cross sections, as the estimator is unable to distinguish between them, and is only dependent on the mesh and Λ, which quantify the amount

Figure 8.6: Residual Source Average Effectivity Index: Top Left $C0$ $c = .1$ Top Right $C0$ $c = .9$ Bottom Left $C1$ $c = .1$ Bottom Right $C1$ $c = .9$

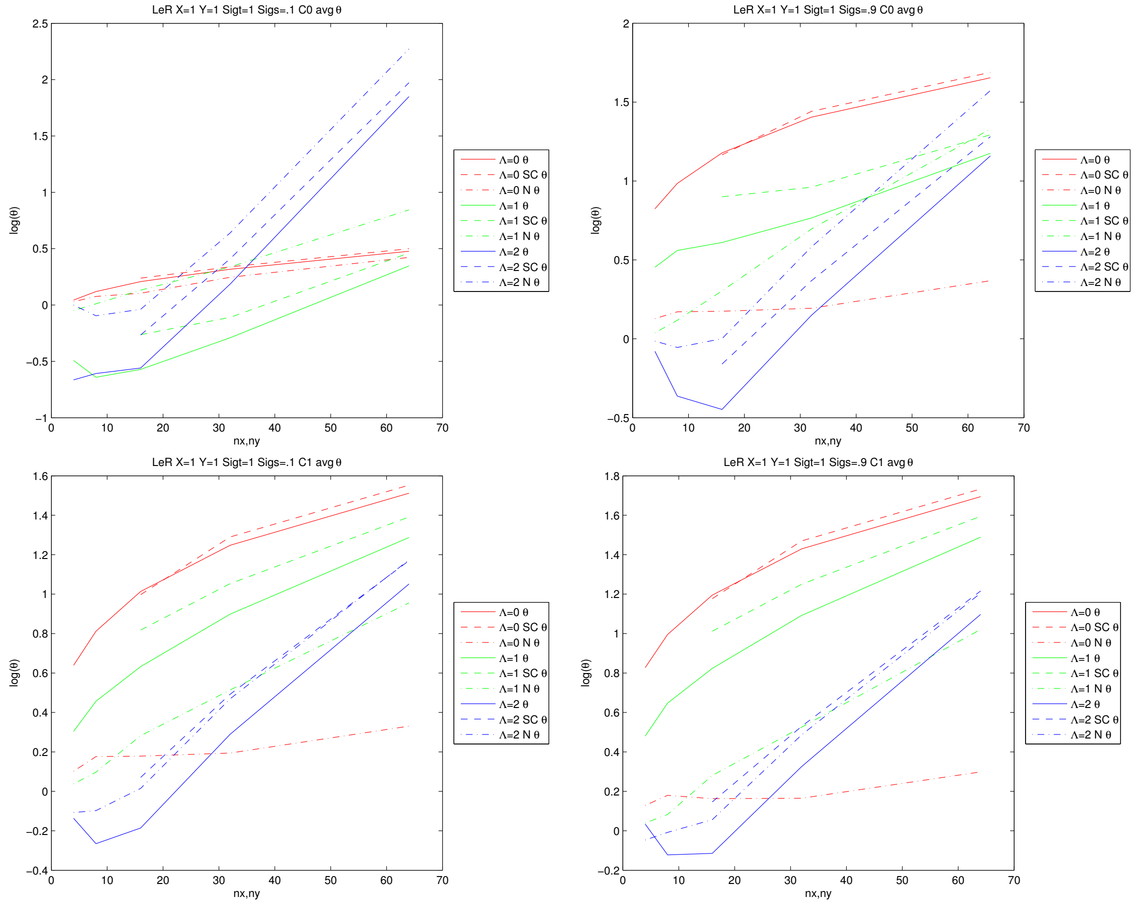

of data that must be processed. An important distinction must be made for all the estimator times. The results do not contain the DGFEM solution times. This is particularly important to note in the two mesh estimators as they require an additional transport calculation on a refined mesh and Residual Source method (Le=R). Additionally, all times are determined from MatLab run codes and MatLab is slower than Fortran. Also, no great attempt at optimizing the calculation was made. Many estimators rely on Legendre polynomial integrations and many zero terms are simply summed instead of avoiding their calculation but this is done consistently for various estimators.

For all of the estimators the computational time to evaluate the estimators increases, as

Figure 8.7: Madsen and $L2$ error: for $\sigma_t = 1.0$ and $c = 0.9$. Left: $C0$ Right: $C1$.

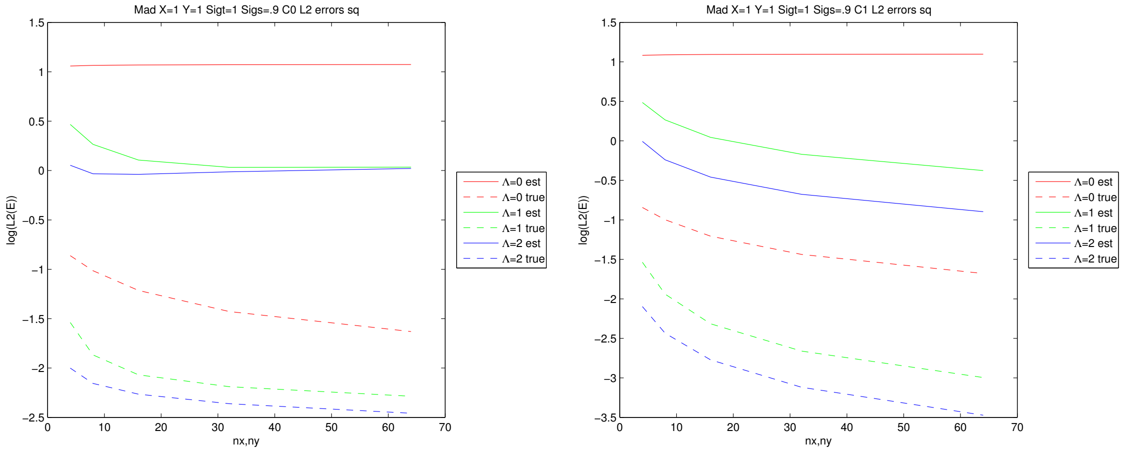

expected, for increased Λ and as the mesh is refined. It is simple to order the estimators in order of increasing times as: Two Mesh, Ragusa and Wang, scalar Jump Discontinuity, Residual Source, Madsen, and angular Jump discontinuity. The question that must be answered is how much computational time is a given quality of the result worth? For example the two mesh estimators are inefficient as they require multiple solutions but this situation is natural for adaptive mesh refinement processes. A cost benifit analysis which accounts for the final estimator application is beyond the scope of this work.

8.4 Conclusion and Future Work

This work set out to explore a collection of *a posteriori* spatial error estimators the One-Speed Discrete Ordinates Neutron Transport Equation cast as a Discontinuous Galerkin Finite Element Method. By using a the Method of Manufactured Solutions the true error in the numerical solution can be found and used as a known comparison for the estimators considered. The problems considered posses a known continuity across singular characteristics which adds another unique level of distinction among the plethora (mesh size, cross sections, order of basis space) of possible test cases. By using standard error estimator verification methods, in particular

Figure 8.8: Madsen Average Effectivity Index: Top Left $C0$ $c = .1$ Top Right $C0$ $c = .9$ Bottom Left $C1$ $c = .1$ Bottom Right $C1$ $c = .9$

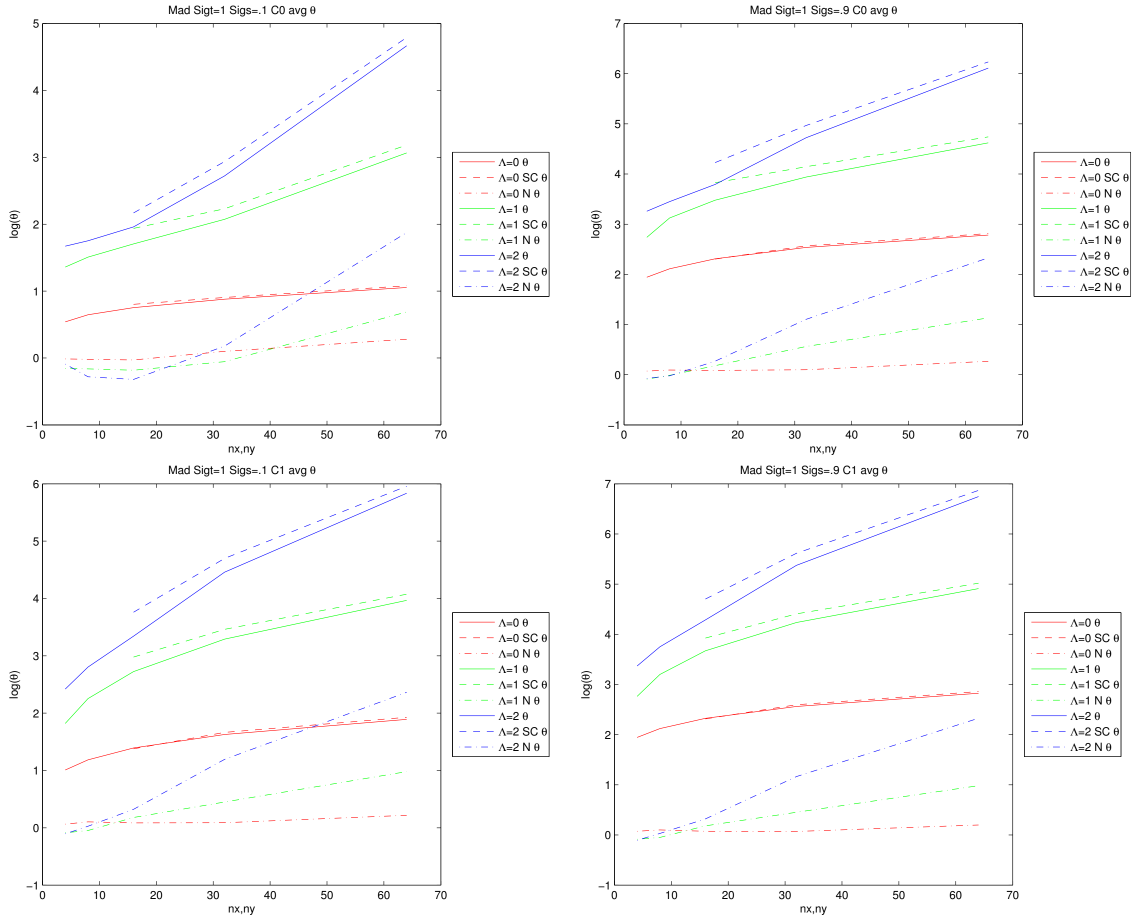

the effectivity index and global L_2 error, both the local and global properties of the considered estimators could be measured and contrasted.

The estimators presented in this work are all generally useful in quantifying the error and its spatial distribution. This is fact is overwhelmed by the presentation of highly refined in which the true error becomes so negligible in magnitude that the estimators cannot approximate it. This effect is naturally accelerated by increasing the expansion order, Λ. However, there is one estimator that seems to escape the trend of increasing average effectivity index, the Ragusa and Wang estimator. Overall this has proven to be the most robust estimator. Even if it frequently

Figure 8.9: Jump Disc. ψ error: for $\sigma_t = 1.0$ and $c = 0.9$. Left: $C0$ Right: $C1$.

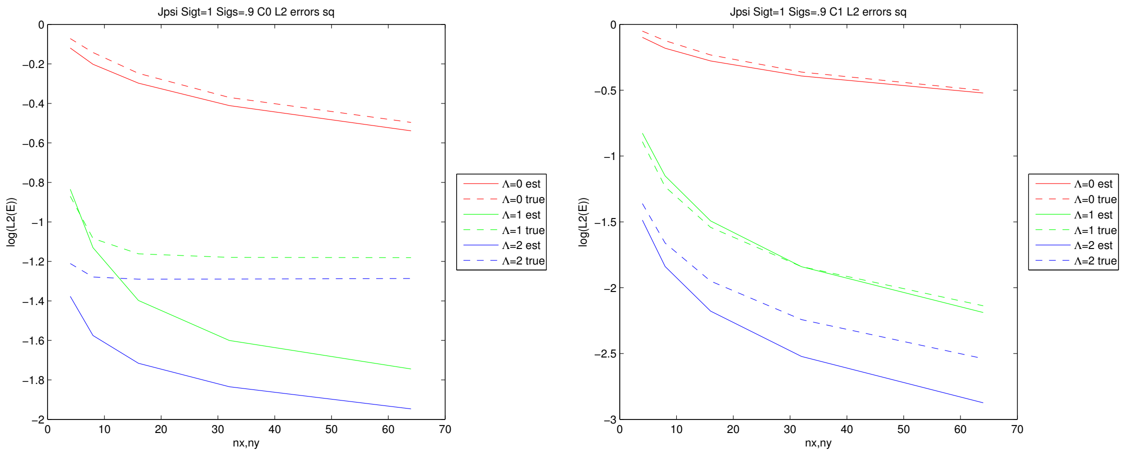

Figure 8.10: Jump Disc. ϕ error: for $\sigma_t = 1.0$ and $c = 0.9$. Left: $C0$ Right: $C1$.

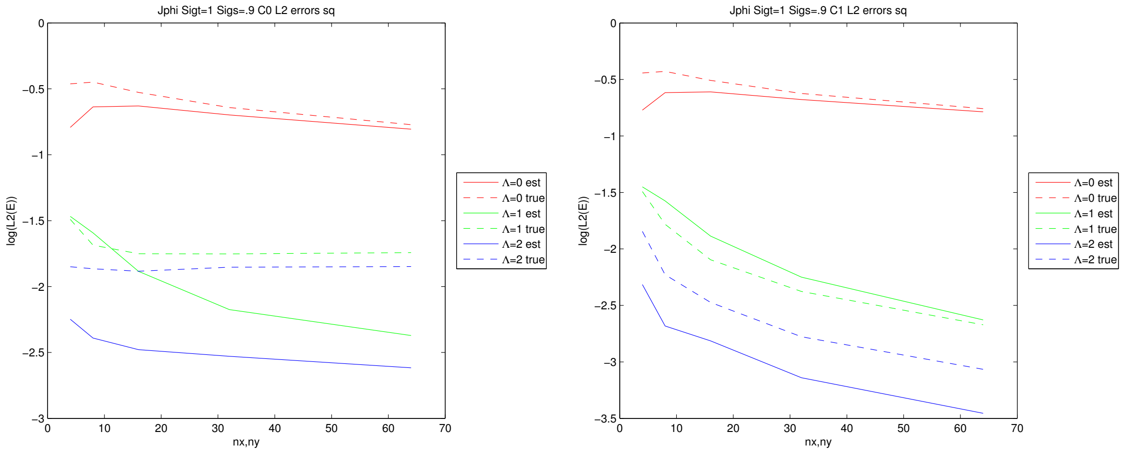

underestimates the true error it does so consistently. This behavior is why it is useful as an AMR metric as used by the authors in [20] and [21]. Additionally its computational cost, once both mesh solutions have been determined, is one of the quickest to evaluate estimators among those considered in this work.

Regarding the limitations of this work, in particular the over resolved true error, future work would consider a new collection of model problems. In particular more realistic test problems, such as multiple materials and even multiplying media. However, these more complex problems do not have a known MMS solution and may have to rely on very refined meshes solutions,

Figure 8.11: Angular Flux Discontinuity Average Effectivity Index: Top Left $C0$ $c = .1$ Top Right $C0$ $c = .9$ Bottom Left $C1$ $c = .1$ Bottom Right $C1$ $c = .9$

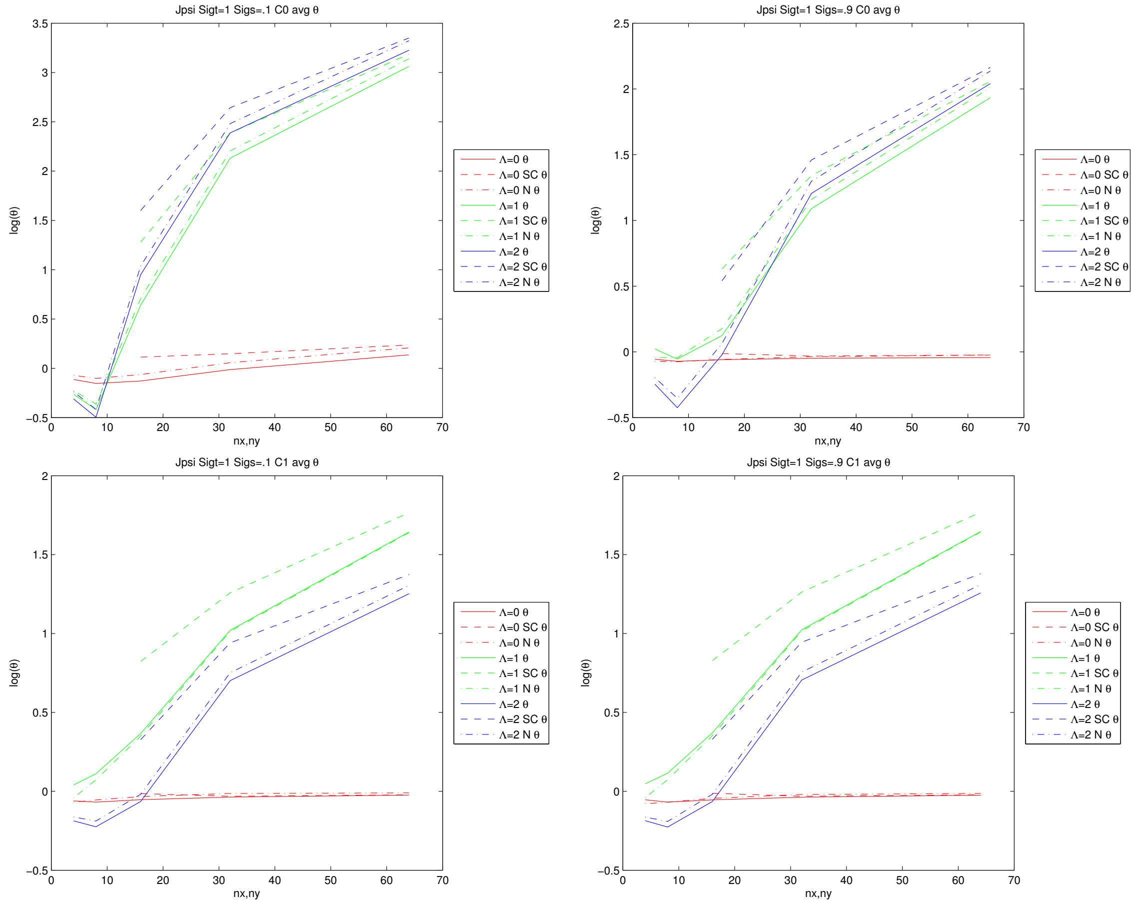

which gives a true error more questionable than the reliablility of MMS derived errors. It may also be useful to observe the error estimator versus the non projected analytic true solution such that the irregulaties are fully represented and are not limited by the size of the basis space.

The Residual Source estimator would be an ideal estimator to explore further. In particular enforcing the residual to always be non-negative, $R = |S - L\psi|$, which would yield an error of the form $e = |\bar{\psi} - \psi|$ in stead of $e = \bar{\psi} - \psi$. The chief difficulty is how to balance the positive value of the residual with the appropriate gradient. It would be interesting to see if additional improvements could be observed if an anisotropic residual source could be considered. Finally, as the singular characteristic lines are *a priori* known it would be insightful to construct a grid of

Figure 8.12: Scalar Flux Discontinuity Average Effectivity Index: Top Left $C0$ $c = .1$ Top Right $C0$ $c = .9$ Bottom Left $C1$ $c = .1$ Bottom Right $C1$ $c = .9$

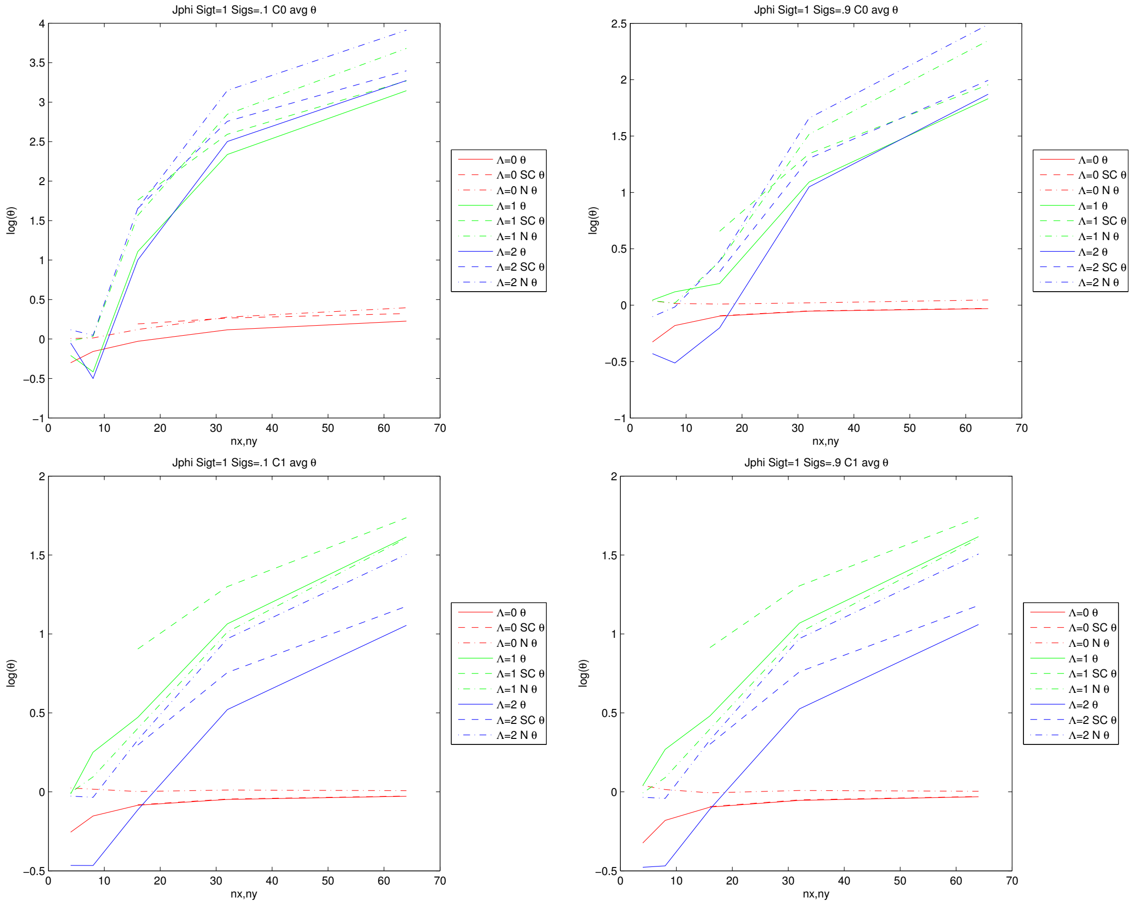

triangular or quadrilateral elements such that these lines are present on element edges and these inter cell discontinuities could be represented more precisely by the DGFEM formulation of the neutron transport equation as was done in [11] and to apply the error estimators considered to this new mesh structure.

Figure 8.13: Computation time of each estimator in seconds, not including DGFEM solver time.

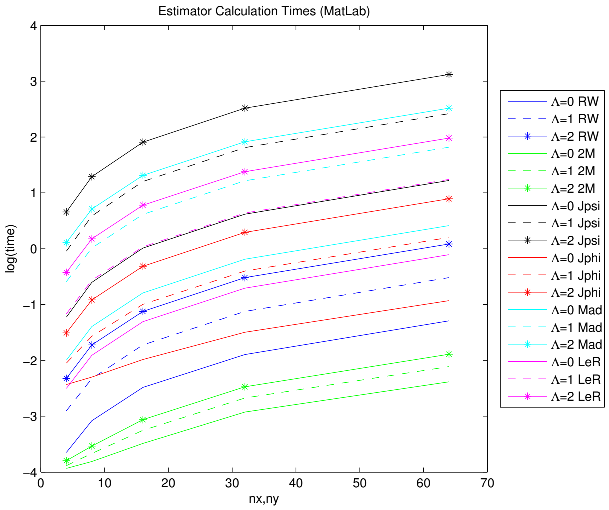

REFERENCES

[1] S. Adjerid and T.C Massey. A posteriori discontinuous finite element error estimation for two-dimensional hyperbolic problems. *Computer Methods in Applied mathematics and Engineering*, 191:5877–5897, 2002.

[2] Marks Ainsworth and J. Tinsley Oden. *A Posteriori Error Estimation in Finite Element Analysis.* Wiley, New York, 2000.

[3] I. Babuska and W.C. Rheinboldt. Error estimates for adaptive finite element computations. *SIAM J. Numer. Anal.*, 15:736–754, 1978.

[4] I. Babuska and W.C. Rheinboldt. A posteriori error analysis for the finite element method. *Internat. J. Numer. Methods Engrg*, 12:1597–1615, 1979.

[5] I. Babuska and W.C. Rheinboldt. A posteriori error analysis of finite element solutions for one dimensional problems. *SIAM J. Numer. Anal.*, 18:565–589, 1981.

[6] R.E. Bank and A. Weiser. Some a posteriori error estimators for elliptic partial differential equations. *Math. Comp.*, 44:283–301, 1985.

[7] G.C. Buscaglia, O.M. Zamonsky, and Y.Y. Azmy. A posteriori error estimation for a nodal method in neutron transport calculations. *20th Iberian Latin-American Congress on Computational Methods in Engineering*, 1999.

[8] L. Demkowicz, Ph. Devloo, and J.T. Oden. On an h-type mesh-refinement strategy based on minimization of interpolation errors. *Comput. Methods Appl. Mech. Engrg*, 53:67–89, 1985.

[9] A.R. Diaz, N. Kikuchi, and J.E. Taylor. A method of grid optimization for finite element methods. *Comput. Meths. Appl. Mech. Engrg*, 41:29–45, 1983.

[10] J.I. Duo, Y.Y. Azmy, and L.T. Zikantanov. A posteriori error estimator and amr for discrete ordinates nodal transport method. *Annals Nuclear Energy*, 36:268–273, 2009.

[11] Jose Ignacio Duo. *Error Estimates for Nodal and Short Characteristics Spatial Approximations of Two-Dimensional Discrete Ordinates Method.* PhD thesis, The Pennsylvania State University, 2008.

[12] D. Fournier, R. Le Tellier, R. Herbin, and C. Suteau. Analysis of an hp-refinement method for solving the neutron transport equation using two error estimators. *International Conference on Mathematics and Computational Methods Applied to Nuclear Science and Engineering*, 2011.

[13] D. Fournier, R. Le Tellier, and C. Suteau. Analysis of an a posteriori error estimator for the transport equation with sn and discontinuous galerkin discretizations. *Annals of Nuclear Energy*, 38:221–231, 2011.

[14] Thomas Grtsch and Klaus-Jrgen Bathe. A posteriori error estimation techniques in practical finite element analysis. *J. Computational and Applied Mathematics*, 83:235–265, 2005.

[15] Jan S. Hesthaven and Tim Warburton. *Nodal Discontinuous Galerkin Methods: Algorithms, Analysis, and Applications.* Springer Publishing Company, Incorporated, 1st edition, 2007.

[16] L. Krivodonova and J.E. Flaherty. Error estimation for discontinuous galerkin solutions of two-dimensional hyperbolic problems. *Adv. Comp. Math.*, 19:57–71, 2003.

[17] P. Ladeveze and D. Leguillon. Error estimate procedure in the finite element method and applications. *SIAM J. Numer. Anal.*, 20:485–509, 1983.

[18] E.E. Lewis and W.F. Miller. *Computational Methods of Neutron Transport.* John Wiley and Sons, New York, 1984.

[19] N.K. Madsen. A posteriori error bounds for the numerical solutions of the neutron transport equation. *Mathematics of Computation*, 27:773–780, 1973.

[20] Jean C. Ragusa and Yaqi Wang. A two-mesh adaptive mesh refinement technique for sn neutral-particle transport using a higher-order dgfem. *Journal of Computational and Applied Mathematics*, 223:3178–3188, 2010.

[21] Jean C. Ragusa and Yaqi Wang. Standard and goal-oriented adaptive mesh refinement applied to radiation transport on 2d unstructured triangular meshes. *Journal of Computational and Applied Mathematics*, 230:763–788, 2011.

[22] Sebastian Schunert and Yousry Y. Azmy. A two-dimensional method of manufactured solutions benchmark suite based on variations of larsen's benchmark with escalating order of smoothness of the exact solution. *International Conference of Mathematics and Computation Methods Applied to Nuclear Science and Engineering*, 2011.

[23] Sebastian Schunert, Yousry Y. Azmy, Damien Fournier, and Romain Le Tellier. Comparison of the accuracy of various spatial discretization schemes of the discrete ordinates equations in 2d cartesian geometry. *International Conference of Mathematics and Computation Methods Applied to Nuclear Science and Engineering*, 2011.

[24] R. Verfurth. A posteriori error estimators for the stokes equations. *Numer. Math.*, 55:309–325, 1989.

[25] O.M. Zamonsky, G.C. Buscaglia, and Y.Y. Azmy. Improving the accuracy of high-order nodal transport methods. *International Conference on Mathematics and Computation, Reactor Physics and Environmental Analysis in Nuclear Applications*, 2:1598, 1999.

[26] O.M. Zamonsky, G.C. Buscaglia, and Y.Y. Azmy. A posteriori error estimation for one dimensional arbitrarily high order transport-nodal method. *Annals Nuclear Energy*, 27:355–369, 2000.

[27] O.C. Zienkiewicz and J.Z. Zhu. A simple error estimator and adaptive procedure for practical engineering analysis. *Internat. J. Numer. Methods in Engrg.*, 24:337–357, 1987.

[28] O.C. Zienkiewicz and J.Z. Zhu. The superconvergent patch recovery and a posteriori error estimates. part 1: The recovery technique. *Internat. J. Numer. Methods in Engrg.*, 33:1331–1364, 1992.

[29] O.C. Zienkiewicz and J.Z. Zhu. The superconvergent patch recovery and a posteriori error estimates. part 2: Error estimates and adaptivity. *Internat. J. Numer. Methods in Engrg.*, 33:1365–1382, 1992.